

THE DYNAMICS OF BOTTOM BOUNDARY
CURRENTS IN THE OCEAN

by

PETER COLVIN SMITH

S.B., Brown University

(1966)

M.S., Brown University

(1967)

SUBMITTED IN PARTIAL FULFILLMENT OF THE
REQUIREMENTS FOR THE DEGREE OF
DOCTOR OF PHILOSOPHY

at the

MASSACHUSETTS INSTITUTE OF TECHNOLOGY

and the

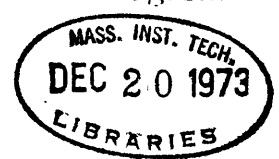
WOODS HOLE OCEANOGRAPHIC INSTITUTION

September, 1973, i.e., Feb. 1974

Signature of Author.....
Joint Program in Oceanography, Massa-
chusetts Institute of Technology -
Woods Hole Oceanographic Institution,
and Department of Earth and Planetary
Sciences, and Department of Meteorology,
Massachusetts Institute of Technology,
September, 1973

Certified by.....
Thesis Supervisor

Accepted by.....
Chairman, Joint Oceanography Committee
in the Earth Sciences, Massachusetts
Institute of Technology - Woods Hole
Oceanographic Institution
Lindgren.



THE DYNAMICS OF BOTTOM BOUNDARY CURRENTS
IN THE OCEAN

by

Peter C. Smith

Submitted to the Joint Oceanographic Committee in the
Earth Sciences, Massachusetts Institute of Techno-
logy and Woods Hole Oceanographic Institution,
on September 14, 1973, in partial fulfillment
of the requirements for the degree of
Doctor of Philosophy

ABSTRACT

This thesis presents an investigation of the dynamics of bottom boundary currents in the ocean. The major emphasis is to develop simple mathematical models in which various dynamical features of these complex geophysical flows may be isolated and explored. Two separate models are formulated and the theoretical results are compared to observational data and/or laboratory experiments. A steady flow over a constant sloping bottom is treated in each model.

A streamtube model which describes the variation in average cross-sectional properties of the flow is derived to examine the interaction between turbulent entrainment and bottom friction in a rotating stratified fluid. Empirical laws are used to parameterize these processes and the associated entrainment and friction coefficients (E_0, K) are evaluated from data for two bottom currents: the Norwegian Overflow and the Mediterranean Outflow. The ability to fit adequately all observations with the solutions for a single parameter pair demonstrates the dynamical consistency of the streamtube model. The solutions indicate that bottom stresses dominate the frictional drag on the dense fluid layer in the vicinity of the source whereas relatively weak entrainment slowly modulates the flow properties in the downstream region. The combined influence of entrainment and ambient stratification help limit the descent of the Mediterranean Outflow to a depth of approximately 1200 m. while strong friction acting over a long downstream scale allows the flow of Norwegian Sea water to reach the ocean floor.

A turbulent Ekman layer model with a constant eddy viscosity is also formulated. The properties of the flow are defined in terms of the layer thickness variable $d(x,y)$, whose governing equation is judged intractable for the general case. However, limiting forms of this equation may be

solved when the layer thickness is much less than (weak rotation) or greater than (strong rotation) the Ekman layer length scale $(\nu/\Omega)^{1/2}$.

In the weak rotation limit, a similarity solution is derived which describes the flow field in an intermediate downstream range. Critical measurements in a laboratory experiment are used to establish distinctive properties of rotational perturbations to the viscous flow, such as the antisymmetric corrections to the layer thickness profile and the surface velocity distribution, which depend on downstream distance like $y^{2/7}$. The constraint of weak rotational effects precludes a meaningful comparison with oceanic bottom currents.

The analysis of the strong rotation limit leads to the prediction of an Ekman flux mechanism by which dense fluid is drained from the lower boundary of the thick core of the current and the geostrophic flow is extinguished. The form of a similarity solution for the downstream flow is derived subject to the specification of a single constant by the upstream boundary condition. The results of some exploratory experiments are sufficient to confirm some qualitative aspects of this solution, but transience of the laboratory flow limits a detailed comparison to theory. Some features of the Ekman flux mechanism are noted in the observational data for the Norwegian Overflow.

Thesis Supervisor: Robert C. Beardsley
Title: Associate Professor of Oceanography
Massachusetts Institute of Technology

ACKNOWLEDGMENTS

The author would like to express his gratitude to Professor Robert C. Beardsley for his guidance and encouragement over the course of this investigation. He is also deeply indebted to Professor H. Stommel who suggested the topic and continually offered valuable criticism of the theoretical ideas as they were being developed. Thanks are also due to Dr. W. McKee for discussions during the early phases of the analysis and to Professor Peter Rhines for his help in the final stages. Also, aid in the setup of the experiments by Mr. William Nispel is acknowledged. Finally, to my wife Julia, who culminated four years of encouragement and support by typing and editing the manuscript, I am more than grateful.

CONTENTS

	<u>Page</u>
Abstract	2
Acknowledgments	4
Figures	7
Tables	11
I. Introduction	12
II. The Streamtube Model	18
II.1 Formulation	21
II.2 Approximate Solutions in Limiting Cases	29
II.2.1 Small Entrainment and Friction $\delta, \bar{\chi} \ll 1$; Homogeneous Environment $\dagger = 0$.	30
II.2.2 Downstream Limit for Zero Entrainment, $\delta = 0$ and Homogeneous Environment $\dagger = 0$.	31
II.2.3 Downstream Limit for Zero Friction, $\bar{\chi} = 0$, and Homogeneous Environment $\dagger = 0$.	33
II.2.4 Small Friction, $\chi \ll 1$, Weak Stratification, $\dagger \ll 1$, Zero Entrainment $\delta = 0$.	35
II.3 Comparison with Norwegian Overflow Data	37
II.4 Comparison with Mediterranean Outflow Data	55
II.5 Concluding Remarks	69
III. Formulation of Ekman-Layer Model	75
IV. Weak Rotation in the Ekman-Layer Model	96
IV.1 A Similarity Solution Including Weak Rotational Effects	98

CONTENTS (CONT'D)

	<u>Page</u>
IV.2 Weak Rotation Experiment	111
IV.2.1 Description of Experimental Methods	111
IV.2.2 Experimental Results	116
IV.3 Discussion	138
V. Strong Rotation in the Ekman-Layer Model	143
V.1 Approximate Theories for the Strong-Rotation Limit of the Ekman-Layer Model	145
V.1.1 Multiple-scale Analysis of the Central Region	147
V.1.2 Method of Characteristics for Flow at the Upper Edge	162
V.2 Laboratory Experiments for the Strong Rotation Limit	166
V.2.1 Design of the Experiment and Apparatus	166
V.2.2 Procedures for the Source Flow Experiments	170
V.2.3 Experimental Results	176
V.3 Conclusion	184
Appendix A. Streamtube Model Equations	187
Appendix B. Derivation of Approximate Solutions to the Streamtube Model Equations for Certain Limiting Cases	196
Appendix C. Method of Characteristics for Flow near the Upper Edge in the Strong Rotation Limit	206
References	210
Biographical Note	214

FIGURES

<u>Figure</u>		<u>Page</u>
2-1	Schematic diagram of streamtube model geometry	22
2-2	Locations of hydrographic sections for Norwegian Overflow data	38
2-3	Cross-sections of Norwegian Overflow	39
2-4	Profiles of potential density, oxygen, and silicates for typical stations in the Norwegian Overflow.	41
2-5	Comparison of average density contrast in Norwegian Overflow data with streamtube model results for several parameter pairs (E_o, K)	47
2-6	Comparison of observed path of stream axis for Norwegian Overflow with streamtube axis for several parameter pairs (E_o, K)	49
2-7	Comparison of cross-sectional area variation for Norwegian Overflow data with streamtube model results for several parameter pairs (E_o, K)	50
2-8	Theoretical mean velocity distribution for several parameter pairs (E_o, K)	51
2-9	Locations of hydrographic sections for Mediterranean Outflow data	58
2-10	Cross-sections of Mediterranean Outflow	59
2-11	Comparison of average density contrast in Mediterranean Outflow data with streamtube model results for several parameter pairs (E_o, K)	63
2-12	Comparison of observed path of stream axis for Mediterranean Outflow with streamtube model results for several parameter pairs (E_o, K)	64

FIGURES (CONT'D)

<u>Figure</u>		<u>Page</u>
2-13	Comparison of velocity data for Mediterranean Outflow with stream-tube model results for several parameter pairs (E_0, K)	65
2-14	Comparison of cross-sectional area variation for Mediterranean Outflow data with streamtube model results for several parameter pairs (E_0, K)	66
3-1	Schematic diagram of the geometry for the Ekman layer model. (a) side view; (b) front view.	80
4-1(a)	Overall view of experimental apparatus	112
(b)	Circulation system	112
(c)	Horizontal traversing mechanism	115
(d)	Close up of thermistor needle probe	115
4-2(a)	Comparison of surface streamline results for non-rotating experiments with theory in Experiment 5-26	117
(b)	Comparison of surface streamline results for non-rotating experiments with theory in Experiment 5-16	118
4-3(a)	Excess downstream displacement vs. mean value of η on surface streamline for Experiment 5-26, $\hat{f} = 0.74 \text{ sec}^{-1}$	121
(b)	Excess downstream displacement vs. mean value of η on surface streamline for Experiment 5-26, $\hat{f} = 1.30 \text{ sec}^{-1}$	122
4-4(a)	Excess downstream displacement vs. mean value of η on surface streamline for Experiment 5-16, $\hat{f} = 0.19 \text{ sec}^{-1}$	124
(b)	Excess downstream displacement vs. mean value of η on surface streamline for Experiment 5-16, $\hat{f} = 0.73 \text{ sec}^{-1}$	125

FIGURES (CONT'D)

<u>Figure</u>		<u>Page</u>
4-4(c)	Excess downstream displacement vs. mean value of η on surface streamline for Experiment 5-16, $\bar{f} = 1.30 \text{ sec}^{-1}$	126
4-5(a)	Comparison of measured thickness profile with theory for Experiment 6-14, $\bar{f} = 0.0 \text{ sec}^{-1}$	128
(b)	Comparison of measured thickness profile with theory for Experiment 6-12, $\bar{f} = 0.0 \text{ sec}^{-1}$	129
(c)	Comparison of measured thickness profile with theory for Experiment 6-13, $\bar{f} = 0.0 \text{ sec}^{-1}$	130
4-6	Antisymmetric perturbations to layer thickness profile for Experiment 6-14	134
4-7	Antisymmetric perturbations to layer thickness profile for Experiments 6-12 and 6-13	135
4-8	Symmetric perturbations to layer thickness profile for Experiments 6-12, 6-13, and 6-14	137
5-1	Flow regimes for strong rotation limit	146
5-2(a)	Free parameters in thick-layer similarity solution	158
(b)	Sample profiles of similarity function for $\eta^- = -1.0, -1.3, -1.75$	160
5-3(a)	View of apparatus for strong rotation experiments	167
(b)	Circulation system showing reservoir, constant head-device, and peristaltic pump	167
5-4(a)	Probe stem carrying conductivity probes and injection tubes for dyed fluid	173
(b)	Motor-driven syringe	173

FIGURES (CONT'D)

<u>Figure</u>		<u>Page</u>
5-5	Circuit diagram for conductivity probe	174
5-6(a)	Source flow for Experiment 7-30.2	177
(b)	Source flow for Experiment 7-30.3	177
5-7	Period of interfacial waves normalized by rotation period for Experiments 7-21.2 and 7-21.3	179
5-8	Comparison of average thickness data to depth contours for similarity solution with symmetric cross-stream profile for Experiments 7-20.1, 7-21.2, and 7-21.3	181

TABLES

<u>Table</u>		<u>Page</u>
I	Physical Constants, Initial Conditions and Scales for the Norwegian Overflow Comparison	44
II	Physical Constants, Initial Conditions and Scales for Mediterranean Outflow Experiment	61
III	Average Dimensionless Friction and Entrainment Coefficients	72
IV	Flow Parameters for Surface-Streamline Experiments	119
V	Flow Parameters for Layer-Thickness Experiments	131
VI	Parameters for the Source Flow Experiments	175

CHAPTER I

Introduction

There is ample motivation for studying the dynamics of bottom boundary currents in the deep ocean. According to Worthington (1969), four of the five sources of North Atlantic deep and bottom water are dense bottom currents entering the North Atlantic from adjoining seas and oceans. Specifically, the waters carried by the overflows from the Norwegian Sea through the Denmark Strait and across the Iceland-Scotland Ridge, the Mediterranean outflow, and the flow of Antarctic Bottom Water across the equator are known to be the major constituents of North Atlantic Deep Water. The basis for this statement is some critical water mass analyses of the hydrographic structure in the North Atlantic Ocean, notably those by Lee and Ellett (1965), (1967) and Worthington and Metcalf (1961). Not only is the composition of the deep water controlled by these currents, but it has also been suggested that the resulting deep circulation pattern and its variability are responsible for the climatological characteristics of northern Europe and for fluctuations in the productivity of the rich fishing grounds of the northwestern North Atlantic [Cooper (1955)]. Furthermore, there is a keen geological interest in bottom current dynamics. Certain evidence suggests that contour-following bottom currents are the principal agents which control the shape of the continental rise and other sedimentary features, such as the Blake-Bahama Outer Ridge

and the Eirik Ridge south of Cape Farewell, Greenland [see Johnson and Schneider (1969)]. Considering their location and orientation it is clear that these sea floor ridges are formed by depositional processes which in turn are controlled by the overflow of dense bottom water from the Norwegian Sea into the North Atlantic.

In contrast to the abundance of water mass analyses and budget calculations involving the deep boundary flows, few attempts have been made to explain their dynamics. There are several notable exceptions, however. Stommel and Arons (1972) have employed a simple potential-vorticity-conserving model to examine the effects of bottom slope, latitude, and transport on deep western boundary currents such as northward flow of Antarctic Bottom Water in the South Atlantic. Of particular interest in these results is the demonstration that the presence of a sloping bottom can produce substantial broadening of inertial boundary currents. On the other hand, Whitehead, Leetmaa and Knox (1973) have used hydraulic concepts in conjunction with potential-vorticity conservation to study the dynamics of strait and sill flows. Their analysis provides relations between transport, upstream conditions, and rotation rate which are then tested successfully against laboratory experiments and observational data. However, their model is tailored specifically to the conditions in the strait and its applicability is therefore limited to the vicinity of the shallowest and narrowest sill. Moreover, both this and the Stommel-Arons model are steady and inviscid. Finally, Bowden (1960) has made an investigation of the dynamics of flow on a submarine ridge which is aimed at interpreting data from the Denmark Strait and Iceland-Scotland overflows. His steady,

two-layer model on a constant sloping bottom incorporates both rotational effects and bottom friction. The conclusion he draws is that bottom friction is solely responsible for the component of flow across bottom contours and should not be neglected. Based on hydrographic data, he computes deflections of the current vector ranging up to 30° downslope.

The purpose of the present study is to examine in detail the dynamics of deep ocean boundary currents. The major emphasis will be to develop simple mathematical models, which isolate certain physical processes at work in these flows and illustrate the interactions among them. The internal consistency of the model will then be demonstrated by testing the theoretical results with laboratory experiments or by comparison to observational data.

The Norwegian Sea overflow through the Denmark Strait and the Mediterranean outflow are adopted as prototypes for this investigation. With the aid of hydrographic data, it is possible to identify or infer certain general characteristics common to these and other deep boundary currents. First of all, the flow emanates from a confined source region and is banked up against the continental slope by the Earth's rotation. Over the course of the stream, the dense water descends along the slope from the sill depth to a constant level or the ocean floor. The cross-stream profile of the current is characteristically broad and thin (order 100 km. x 100 m.) and the bottom slope is generally small (10^{-2}).

Furthermore, the flow regime in the outflows may be assumed to be fully turbulent. The Reynolds numbers based on typical velocity and length scales with molecular viscosity are quite large ($10^7 - 10^8$),

whereas the hydrodynamic stability is weak due to relatively small density contrasts with the surrounding medium. Evidence for entrainment and mixing of the outflow current with adjacent waters is afforded by water mass analysis of the changing properties at the core of the stream. Moreover, the generally rough topography coupled with high Reynolds numbers suggests that strong turbulence is generated at the base of the flow. The rugged bottom may also exert a strong influence on the path of the outflow current. In the Mediterranean outflow, for instance, the jet which emanates from the Strait of Gibraltar is fragmented into several veins which plunge down submarine canyons as the mean axis of the stream spreads over the northern slope of the Gulf of Cadiz [see Madelain (1969)].

Finally, numerous investigations [Cooper (1955), Mann (1969), Worthington (1969)] have revealed a distinct temporal variability in the overflow currents. However, the details of these fluctuations and their controlling mechanisms are poorly understood, largely because of the difficulty of obtaining adequate synoptic coverage with hydrographic surveys.

Faced with the complexity of these geophysical flows, the theoretical analysis will be formulated to treat only certain aspects of the fluid dynamical problem. Making use of observed parameters and scales in the outflow data, two separate models which describe steady, two-layer flows over plane topography are presented in the following chapters. In the investigation of simple dynamical balances, attention will be focused on the effects of entrainment, bottom friction, and rotation.

In Chapter II, a streamtube model which describes integral properties of the outflow currents will be formulated and used to determine important scales of motion as well as to demonstrate the gross interaction among entrainment, bottom friction, the Coriolis acceleration, and stratification of the ambient density field. Empirical laws will be used in this study to parameterize the entrainment and frictional effects, and the associated proportionality constants are evaluated by comparing solutions of the model equations to hydrographic and current meter data from the Norwegian and Mediterranean outflows. These results provide a consistent overall picture of the outflow dynamics.

In Chapter III, a more detailed Ekman layer model is derived in which entrainment is ignored and the balance between rotation and friction is examined in a homogeneous environment. The properties of the flow in this model may be related to the distribution of layer thickness in the downstream region. However, the general equation governing the thickness variable is judged to be intractable. Nevertheless, the two important limiting forms of this equation for strong friction and strong rotation may be analyzed and are treated individually in Chapters IV and V.

A similarity solution for the viscous limit in which weak rotational effects are included as perturbations is derived in Chapter IV. The resulting theoretical expressions for the flow variables, which are valid over a limited downstream range, are then tested successfully by a series of critical laboratory experiments. In Chapter V, on the other hand, the mathematical analysis of the strong rotation limit leads to a

similarity solution for the thick geostrophic core of the stream.

This result is supplemented by a viscous solution valid near the upper edge of the flow. Some exploratory experiments for source flow in a rapidly rotating system will also be described in this chapter.

CHAPTER II

The Streamtube Model

Historically, integral techniques have proved to be very powerful methods in a variety of fluid dynamical applications (e.g. boundary layer theory, hydraulics). In the present context, a streamtube model will be employed to demonstrate some dynamical features of bottom boundary currents. Specifically the effects of entrainment, bottom friction, Coriolis acceleration and ambient density stratification will be investigated in an attempt to evaluate their relative importance in determining the path of the stream as well as variations in its average flow properties, i.e., mean velocity, density contrast, and cross-sectional area.

The processes of entrainment and bottom friction result from turbulence present in the outflow current which mixes in fluid from the surrounding medium across the upper interface of the flow and transmits momentum to the bottom by the action of turbulent Reynolds stresses, thereby causing a drag on the fluid above. To understand fully the physics of these processes, it is essential to distinguish clearly the nature of this turbulence and the mechanism(s) by which it is generated and maintained. However, for modelling purposes, two different empirical laws will be adopted to account for the effects of entrainment and friction. Each contains an unknown constant which must be determined independently from laboratory experiments or by comparison with observations.

The first of these relations sets the total volumetric entrainment per unit length of the stream equal to a constant fraction of the mean velocity of the flow with a proportionality constant E_0 . A similar assumption has been used by Ellison and Turner (1959) in their experiments with

turbulent stratified flow down inclines. Their results indicate that the appropriate value of E_0 for a given physical situation depends rather critically on the "overall Richardson number", Ri_0 , a stability parameter based on the initial density contrast, characteristic depth, and velocity. On the other hand, the frictional resistance is related to the square of the mean velocity through an unknown factor, K . Quadratic drag laws have been used successfully in a number of oceanographic applications [Defant (1961)], so estimates of the magnitude of the drag coefficient are available.

In other applications, the coefficients corresponding to E_0 and K are dimensionless. However, in the present context, both E_0 and K are found to have the dimension of length due to an integration performed in the cross-stream direction. Since the analysis only provides information about the area of the cross-stream profile, not its linear dimensions, it is not possible to use average dimensionless coefficients by dividing E_0 and K by the local cross-stream scale. Furthermore, an estimate of the stability parameter is unavailable because the characteristic depth of the layer is unknown. In an attempt to overcome these deficiencies, an alternative streamtube model was considered in which the area was expressed as a variable cross-stream dimension times the average layer depth. By analogy to the two-dimensional nonrotating results of Ellison and Turner (1959), the layer depth was specified to increase linearly in the downstream direction. However, it was felt that the introduction of assumptions about the entrainment process derived from a situation in which the dynamical balances were different not only limited the flexibility of the model but also

could not be justified from a physical standpoint. Moreover, because of the ambiguity involved in assigning particular dimensions to the profiles of actual outflow currents over rough topography, this alternate model was rejected.

The usefulness of the present model lies in its ability to fit observational data with unique values of the empirical constants, E_0 and K . Hydrographic sections furnish estimates of the density contrast, cross-sectional area, and path of the stream, while current meter and/or Swallow float data provide estimates of the mean velocity. If all these data can be fit with reasonable accuracy by the solutions for a single parameter pair (E_0 , K), then the dynamical consistency of the model is demonstrated. Once this is achieved, it is then possible, using observed cross-stream dimensions, to estimate average dimensionless friction and entrainment coefficients and compare them to those deduced in other oceanographic situations and in laboratory experiments.

II.1 Formulation

A schematic diagram showing the geometrical aspects of the streamtube model is presented in Figure 2-1. The bottom plane is inclined at a small angle α to the horizontal, and the rotation $\underline{\Omega}$ and gravity \underline{g} vectors are aligned vertically. Two coordinate systems will be employed in the model. The first is a Cartesian system whose orientation is fixed by the bottom topography. Its origin is located at the source, the x-axis lies along a bottom contour, the y-axis points downslope, and z is measured normal to the bottom.

The second system is a set of streamwise coordinates (ξ, η) in which every point (x, y) in the neighborhood of the current is associated with a normal distance η from the stream axis ($\eta = 0$) and a corresponding point on the ξ axis where ξ is the distance from the source. The value of ξ defines uniquely both the position of the axis of the streamtube in the bottom-fixed coordinates, $(X(\xi), Y(\xi))$, and a local pitch angle, β , between the streamtube and x axes. Therefore, the equations for the path of the stream are

$$\frac{dX}{d\xi} = \cos \beta, \quad (2.1)$$

and

$$\frac{dY}{d\xi} = \sin \beta. \quad (2.2)$$

The governing equations for the streamtube model are derived in Appendix A. The formulation proceeds from the differential equations of motion (rather than from integral theorems) in order to emphasize the detailed assumptions made in the analysis. The major constraints placed on the mean flow variables

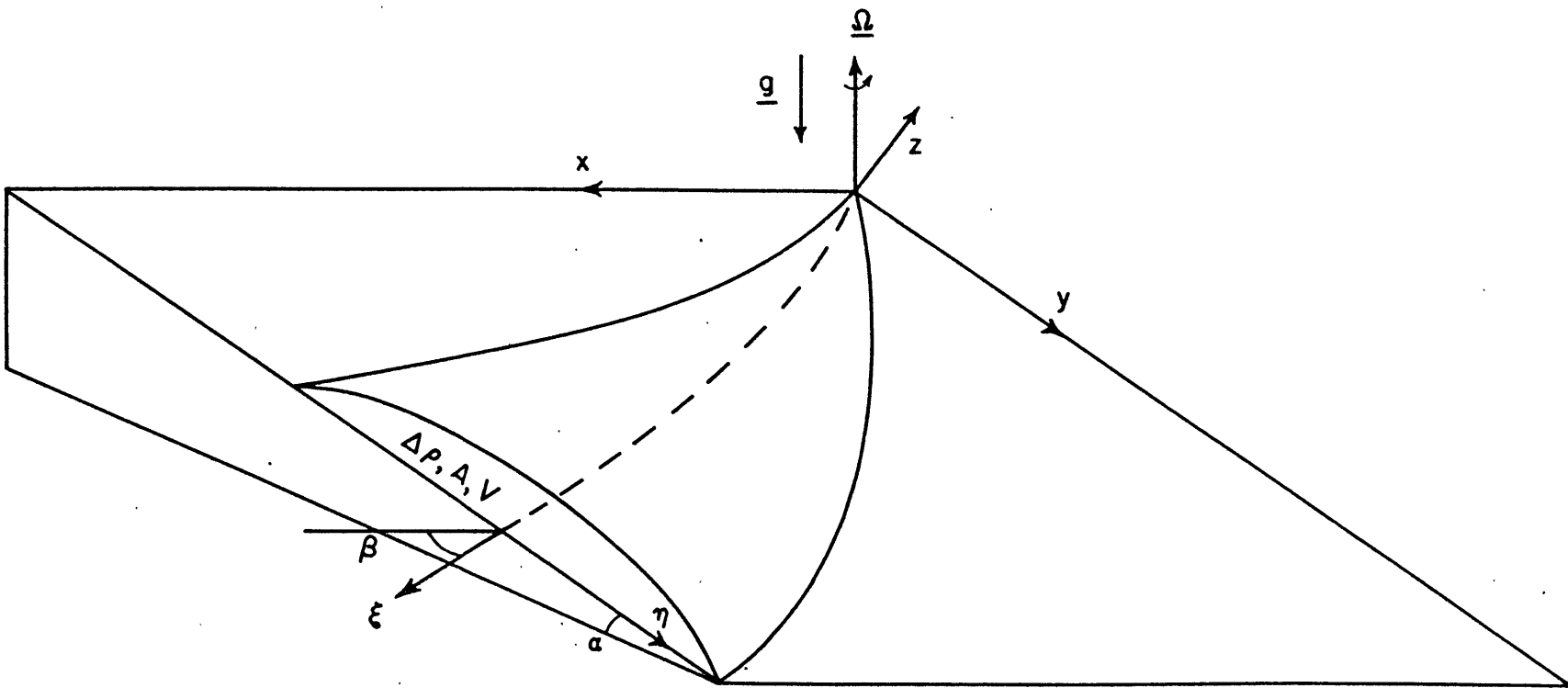


Figure 2-1. Schematic diagram of streamtube model geometry.

are that the flow is steady, the strong axial velocity and excess density fields are concentrated in a broad, thin layer adjacent to the bottom, and that these quantities are nearly uniform over a cross section of the stream. In addition, the current is narrow in the sense that the cross-stream scale is much smaller than the local radius of curvature of the stream axis. Furthermore, the turbulent velocity and density profiles are assumed to exhibit similarity forms, so that the turbulent stresses and rate of entrainment may be related solely to the mean velocity and density contrasts [see Morton (1959)]. The postulated forms for the turbulent entrainment and friction laws are

a) entrainment,

$$E_0 V = \int_{\xi^-}^{\xi^+} w_e d\eta, \quad (2.3)$$

and b) friction,

$$\rho K V^2 = \int_{\xi^-}^{\xi^+} (\tau_B + \tau_I) d\eta, \quad (2.4)$$

where $w_e(\xi, \eta)$ is the entrainment velocity at the interface, $\tau_B(\xi, \eta)$ and $\tau_I(\xi, \eta)$ are the turbulent stress components (defined in a sense opposing the mean motion) at the bottom and interface respectively, and $\eta = \xi^-(\xi), \xi^+(\xi)$ are the edges of the flow.

Subject to these conditions, the dynamical equations for the streamtube model have the form

$$\frac{d}{d\xi} (AV) = E_0 \bar{V}, \quad (2.5)$$

$$\frac{d}{d\xi} (\rho AV) = \rho_e E_0 \bar{V}, \quad (2.6)$$

$$\rho \bar{V} \left(\hat{f} + V \frac{d\beta}{d\xi} \right) = S \hat{g} \Delta \rho \cos \beta, \quad (2.7)$$

and

$$\frac{d}{d\xi} (\rho A V^2) = s \hat{g} \Delta \rho A \sin \beta - \rho K V^2, \quad (2.8)$$

where $V(\xi)$ and $\Delta \rho(\xi)$ are the mean velocity and density contrasts and $A(\xi)$ is the cross-sectional area. In addition to the entrainment constant E_0 and friction coefficient K , the parameters appearing in the equations are the slope $s = \tan \alpha$, and the normal components of the Coriolis parameter $\hat{f} = 2|\underline{\Omega}| \cos \alpha$ and gravity $\hat{g} = |g| \cos \alpha$. The excess density is defined as the difference between density in the current and the local ambient density, i.e.,

$$\Delta \rho = \rho - \rho_e, \quad (2.9)$$

where

$$\rho_e(\xi) = \rho_0 [1 + s \hat{T} Y(\xi)], \quad (2.10)$$

and $\hat{T} = T \cos \alpha$ is the stratification rate normal to the plane in the quiescent region. According to the model, the divergence of the downstream volumetric flow rate is measured by the entrainment, $E_0 V$, the cross-stream balance is geostrophic with a correction for the curvature of the path, $\frac{d\beta}{d\xi}$, and the divergence of the downstream momentum flux is driven by the downslope component of gravity and retarded by friction.

Considering (2.1) and (2.2) along with (2.5) - (2.10) as the full set of model equations, the mathematical formulation is completed by imposing a suitable set of initial conditions at the source:

$$V = V_0,$$

$$\begin{aligned}
\Delta\rho &= \Delta\rho_0, \\
A &= A_0, \\
\beta &= \beta_0, \\
X &= Y = 0,
\end{aligned}
\tag{2.11}$$

at $\xi = 0$.

As a further simplification, the Boussinesq approximation is now invoked in the momentum equation which implies $\rho = \rho_e = \rho_0$ except when combined with gravity. After making some convenient definitions,

$$r(\xi) = (\Delta\rho)^{-1} = \text{inverse of density contrast}, \tag{2.12}$$

$$H(\xi) = \Delta\rho A V = \text{flux of excess density}, \tag{2.13}$$

further manipulation yields the following form for the dynamical equation

$$\frac{dH}{d\xi} = -\rho_0 s \hat{T} r H \sin\beta, \tag{2.14}$$

$$\frac{dr}{d\xi} = \frac{E_0 V}{H} + \rho_0 s \hat{T} r^2 \sin\beta, \tag{2.15}$$

$$r V^2 \frac{d\beta}{d\xi} = \frac{s \hat{q}}{\rho_0} \cos\beta - \hat{f} r V, \tag{2.16}$$

and

$$r V \frac{dV}{d\xi} = \frac{s \hat{q}}{\rho_0} \sin\beta - \frac{(E_0 + K)}{H} V^3. \tag{2.17}$$

where the initial conditions corresponding to equations (2.14) and 2.15) are

$$\begin{aligned}
r &= r_0 = (\Delta\rho_0)^{-1}, \\
H &= H_0 = \Delta\rho_0 A_0 V_0
\end{aligned}
\tag{2.18}$$

at $\xi = 0$.

Note that the density contrast, $\Delta\rho = r^{-1}$, is modified both by entrainment and by the effect of descending along the slope into a denser medium. Also

note from equation (2.17) that the entrainment, while not affecting the momentum flux, has a decelerating effect on the velocity due to the injection of mass into the stream.

Next the variables are normalized in the following way:

$$\begin{aligned} r &= r_0 r' , \\ V &= U V' , \\ (\xi, X, Y) &= L (\xi', X', Y') , \\ H &= \frac{L^2 U}{r_0} H' , \end{aligned} \tag{2.19}$$

where the geostrophic velocity scale U and the topographic length scale L are defined by

$$\begin{aligned} U &= s \hat{q} / \rho_0 r_0 \hat{f} , \\ L &= U / f = s \hat{q} / \rho_0 r_0 \hat{f}^2 . \end{aligned}$$

The full set of dimensionless model equations then takes the form

$$\frac{dH'}{d\xi'} = -\gamma r' H' \sin \beta , \tag{2.20}$$

$$\frac{dr'}{d\xi'} = \delta \frac{V'}{H'} + \gamma r'^2 \sin \beta , \tag{2.21}$$

$$r' V'^2 \frac{d\beta}{d\xi'} = \cos \beta - r' V' , \tag{2.22}$$

and
$$r' V' \frac{dV'}{d\xi'} = \sin \beta - (\delta + \chi) \frac{V'^3}{H'} , \tag{2.23}$$

with
$$\frac{dX'}{d\xi'} = \cos \beta , \tag{2.24}$$

and
$$\frac{dY'}{d\xi'} = \sin \beta . \tag{2.25}$$

The corresponding initial conditions are

$$\begin{aligned}
 H' &= H_0' , \\
 r' &= 1 , \\
 V' &= V_0' , \\
 \beta &= \beta_0 , \\
 X' &= Y' = 0 .
 \end{aligned}
 \quad \text{at } \xi' = 0 .
 \tag{2.26}$$

The dimensionless constants appearing in the equations are the entrainment parameter,

$$\delta = E_0 / L_1 ,
 \tag{2.27}$$

which measures the amount of entrainment over a topographic wavelength, the friction parameter,

$$\chi = K / L_1 ,
 \tag{2.28}$$

which measures the frictional dissipation over that distance, and the stratification parameter,

$$\gamma = \rho_0 s T r_0 L_1 = s^2 \frac{\hat{g} \hat{T}}{\hat{f}^2} = \frac{N^2 \sin^2 \alpha}{f^2 \cos^2 \alpha} ,
 \tag{2.29}$$

which measures the square ratio of the natural frequency for motion along the slope of a particle of density ρ_0 in a stratified system to that in a rotating system.

Numerical solutions for the streamtube model were obtained by integrating equations (2.20) to (2.25) in the downstream direction starting with the initial values, (2.26). The calculations were performed on an IBM system 360 computer using a modified Adams "predictor-corrector" scheme.

II.2 Approximate Solutions in Limiting Cases

Before proceeding to the comparison with observational data, it is instructive to examine the behavior of solutions to equations (2.20) - (2.25), subject to (2.26), in several limiting cases. For certain ranges of the parameters (δ, κ, γ) and in certain regions of the flow, approximate solutions to this system may be found by asymptotic methods. These solutions fall into two categories:

- (i) linearized solutions, which are valid in the vicinity of the source for small values of the parameters and restricted initial conditions, and
- (ii) asymptotic solutions in the downstream region ($\xi' \rightarrow \infty$) where irregularities in the flow are damped by friction or entrainment and the flow variables attain constant values.

In all cases, the results of these approximate analyses are confirmed by quantitative comparison to numerical solutions of the full equations in the appropriate regime.

The most important qualitative features of the streamtube model may be extracted from the case of uniform external density ($\gamma = 0$). This limit is characterized by a constant flux of excess density such that $H' = H_0'$. Therefore, to streamline the notation, it is convenient to define modified entrainment and friction parameters as,

$$\bar{\delta} = \delta / H_0' ; \quad (2.30)$$

and

$$\bar{\kappa} = \kappa / H_0' . \quad (2.31)$$

Four different limiting cases were analyzed and the resulting approximate solutions are summarized and discussed below. The complete derivation of these expressions is found in Appendix B.

II.2.1 Small Entrainment and Friction $\bar{\delta}, \bar{\chi} \ll 1$; Homogeneous Environment $\gamma = 0$.

For small values of $\bar{\delta}$ and $\bar{\chi}$ with $\gamma = 0$, a bilinear perturbation expansion of the dimensionless flow variables yields a linearized solution to streamtube model equations valid in the source region, provided the initial conditions are suitably constrained, i.e.,

$$\beta_0 \leq \mathcal{O}(\bar{\delta}, \bar{\chi}) \quad , \quad V_0' - 1 = \Delta V_0' \leq \mathcal{O}(\bar{\delta}, \bar{\chi}) . \quad (2.33)$$

The resulting expressions for the dimensionless variables to first order in both $\bar{\delta}$ and $\bar{\chi}$ are

$$r' = 1/\Delta \rho' = 1 + \bar{\delta} \xi' \quad , \quad (2.34)$$

$$V' = 1 - \bar{\delta} \xi' - (\beta_0 - \bar{\chi}) \sin \xi' + \Delta V_0' \cos \xi' \quad , \quad (2.35)$$

$$\beta = (\beta_0 - \bar{\chi}) \cos \xi' + \Delta V_0' \sin \xi' + \bar{\chi} \quad , \quad (2.36)$$

$$A' = A_0' \left[1 + 2\bar{\delta} \xi' + (\beta_0 - \bar{\chi}) \sin \xi' + \Delta V_0' (1 - \cos \xi') \right] . \quad (2.37)$$

Note that the presence of the secular terms at first order in $\bar{\delta}$ limits the validity of the perturbation scheme to a region $\xi' < \bar{\delta}^{-1}$.

These results indicate that, near the source, a pattern of steady, topographic meanders of wavelength $2\pi L_1$ arises from mismatches between the imposed initial conditions and the "preferred state":

$\beta = \bar{\chi}$; $V' = 1$. Furthermore the appearance of the secular terms at first order implies that initially both the velocity and density contrast diminish linearly with downstream distance, whereas the area increases with ξ' at twice the rate. The velocity and cross-sectional area both oscillate about these initial trends, while the pitch angle β oscillates about its preferred value of $\bar{\chi}$, the friction parameter.

Beyond the region of validity of perturbation theory ($\xi' > \bar{\delta}^{-1}$), the numerical solutions indicate that the oscillations induced by the initial conditions are damped and β approaches a constant value. Furthermore, for large values of the entrainment of friction parameter ($\bar{\delta}$ or $\bar{\chi} > 1$) the solutions appear critically damped and no meanders appear.

II.2.2 Downstream Limit for Zero Entrainment, $\bar{\delta} = 0$, and Homogeneous Environment, $\bar{\gamma} = 0$.

In this asymptotic limit ($\xi' \rightarrow \infty$), the meanders present near the source are damped by friction and the axis approaches a constant pitch angle at which the viscous drag exactly balances the downslope component of gravity. For this case, all flow variables approach constant values governed by the following relations

$$r' = 1 \quad , \quad (2.38)$$

$$A' = H_0' / V' \quad , \quad (2.39)$$

$$\tan \beta = \bar{\chi} V'^2 \quad , \quad (2.40)$$

$$\bar{\chi}^2 V'^6 + V'^2 - 1 = 0 \quad . \quad (2.41)$$

The cubic equation for V'^2 has only one real root, so choosing its positive square root,

$$V' = 2^{-1/6} \bar{\chi}^{-1/3} \left\{ \left(1 + \sqrt{1 + 4/27 \bar{\chi}} \right)^{1/3} + \left(1 - \sqrt{1 + 4/27 \bar{\chi}} \right)^{1/3} \right\} \quad , \quad (2.42)$$

serves to specify all the variables uniquely.

In the absence of entrainment and external stratification, the density contrast remains fixed at its initial value. The limiting velocity exhibits a rather complicated dependence on the friction parameter, $\bar{\chi}$. However, for the case of strong friction ($\bar{\chi} \gg 1$) V' is given approximately by,

$$V' = \bar{\chi}^{-1/3} \quad ,$$

so

$$\beta = \tan^{-1} (\bar{\chi}^{1/3}) \quad ,$$

(2.43)

$$A = H_0' \bar{\chi}^{1/3} \quad ,$$

for $\bar{\chi} \gg 1$.

Similarly for the case of weak friction ($\bar{\chi} \ll 1$),

$$V' = 1 - \frac{\bar{\chi}^2}{2} + \dots$$

so

$$\beta \doteq \tan^{-1}(\bar{\chi}) \doteq \bar{\chi}, \quad (2.44)$$

$$A' \doteq H'_0 \left(1 + \frac{\bar{\chi}^2}{2}\right), \quad \text{for } \bar{\chi} \ll 1.$$

In the former case, the velocity is small and the pitch angle approaches a value of $\pi/2$, that is, the stream axis points directly downslope.

In the latter case, the velocity is near its geostrophic value ($V' = 1$) and the pitch angle is very shallow, so the flow tends to follow bottom contours. Notice, the direct dependence of β on $\bar{\chi}$ in both cases.

II.2.3 Downstream Limit for Zero Friction, $\bar{\chi} = 0$, and Homogeneous Environment, $\gamma = 0$.

For the frictionless limit ($\bar{\epsilon}' \rightarrow \infty$), oscillations in the source region decay due to entrainment. As demonstrated in Appendix B, the only constant value of the pitch angle which is consistent with the limiting forms of the equations is $\beta = 0$. Therefore, in this limit, the stream axis ultimately parallels bottom contours.

The behavior of the other variables for this case is evident from their asymptotic forms:

$$r' \sim (2\bar{\delta}\bar{\epsilon}' + c)^{1/2}, \quad (2.45)$$

$$V' \sim (2\bar{\delta}\xi' + c)^{-1/2}, \quad \text{as } \xi' \rightarrow \infty. \quad (2.46)$$

and

$$A' \sim H_0' (2\bar{\delta}\xi' + c), \quad (2.47)$$

The density contrast and velocity decay at a rate proportional to the square root of downstream distance, whereas the cross-sectional area grows linearly with ξ .

It is possible to extend the results for this limit to include a weak frictional effect if the pitch angle β is assumed to be small but non-zero. The expressions for r' and V' given in (2.45) and (2.46), which are based on the entrainment law and geostrophy, imply a non-divergent downstream momentum flux. If friction is included for small β , then the remaining balance in the downstream momentum equation yields

$$\beta = \bar{\chi} V'^3 \sim \bar{\chi} (2\bar{\delta}\xi' + c)^{-3/2}, \quad (2.48)$$

where the value of c is no longer constant but a function of $\bar{\chi}$, i.e., $c = c(\bar{\chi})$. Note that this result is fully compatible with the condition that β vanish downstream. Assuming such a state may be achieved, an estimate of the downstream point beyond which this balance holds is given by

$$\xi_T' = \xi_T / L_1 = \frac{(\bar{\chi} / \beta_T)^{2/3}}{2\bar{\delta}}, \quad (c=0) \quad (2.49)$$

where β_T is the small pitch angle observed at the transition point, $\xi = \xi_T$.

II.2.4 Small Friction, $\chi \ll 1$, Weak Stratification, $\gamma \ll 1$,
Zero Entrainment, $\delta = 0$.

Significant effects of external stratification can occur only in conjunction with frictional effects since all terms in the model equations multiplied by γ also contain $\sin \beta$ which vanishes as $\xi' \rightarrow \infty$ in the absence of friction. However, with friction, the current descends the slope into a denser environment, and both the density contrast and the flux of excess density are thereby reduced.

Using an expansion procedure entirely analogous to that used to derive the results for the homogeneous case, with the same constraints on the initial conditions, the perturbation analysis for the case of $\chi, \gamma \ll 1$ yields the following expressions for the dimensionless variables:

$$H' = H_0' \left[1 - \gamma \left\{ (\beta_0 - \bar{\chi}) \sin \xi' + \Delta V_0' \cos \xi' + \bar{\chi} \xi' \right\} \right] + \mathcal{O}(\gamma^3), \quad (2.50)$$

$$r' = 1 + \gamma \left[(\beta_0 - \bar{\chi}) \sin \xi' + \Delta V_0' \cos \xi' + \bar{\chi} \xi' \right] + \mathcal{O}(\gamma^3), \quad (2.51)$$

$$V' = 1 + (\beta_0 - \bar{\chi}) \sin \xi' + \Delta V_0' \cos \xi' + \mathcal{O}(\gamma^2), \quad (2.52)$$

$$\beta = (\beta_0 - \bar{\chi}) \cos \xi' - \Delta V_0' \sin \xi' + \bar{\chi} + \mathcal{O}(\gamma^2), \quad (2.53)$$

$$A' = A_0' \left[1 - (\beta_0 - \bar{\chi}) \sin \xi' + \Delta V_0' (1 - \cos \xi') \right] + \mathcal{O}(\gamma^2). \quad (2.54)$$

Note that the secular terms in these results appear first at order $\gamma \bar{\chi}$, so that the range of validity of this solution extends out to $\xi' = (\gamma \bar{\chi})^{-1}$.

The pattern of steady meanders which arises in the solution for $\bar{\delta}, \bar{\chi} \ll 1$ is preserved here and appears also in the expressions for r' and H' at higher order ($\delta \bar{\chi}$). The mean rate of descent, $\bar{\chi}$, due to frictional influence, is accompanied by diminishing trends in the density contrast and excess density flux which also appear at order $\delta \bar{\chi}$. Notice that despite the expansion of variables in χ , the parameter which appears in the final result is the modified friction parameter, $\bar{\chi} = \chi/H_0'$.

The foregoing results will prove useful in interpreting the numerical solutions which are to be compared with outflow data.

II.3 Comparison with Norwegian Overflow Data

The observational data to be used for the comparison of the stream-tube model with the Norwegian Overflow come from a series of hydrographic sections taken during cruise BIO 0267 of the C.S.S. Hudson from January to April, 1967 [see Grant (1968)]. Since the purpose of this cruise was to define the course and water mass characteristics of the outflow, the system of measurement within the current itself was quite comprehensive. An acoustic pinger was attached to the bottom of the wire on all casts to allow the lowest bottle to be positioned less than 10 meters from the bottom and the bottle spacing was generally 25 meters in the lowest 200 meters of water [see Mann (1969)]. Unfortunately, there are no velocity data available to accompany the hydrographic survey despite an attempt by Worthington (1969) to measure currents in the Denmark Strait.

The locations of the stations used for this comparison are shown in Figure 2-2. The sections cover the region from the sill of the Denmark Strait (Section I) to the vicinity of Cape Farewell (Section VII) along the continental slope of Greenland. Sections I and II were run at the end of January, Sections III and VII in early February, and Sections IV, V, VI toward the end of March.

Using smoothed bottom topography, a series of cross-sections of the outflow current showing station locations is presented in Figure 2-3. The overflow water is delineated by two contours. The solid curve is the $\sigma_{\theta} = 27.9$ contour which according to Worthington (personal communication) is a reasonable boundary for the overflow water. The dashed

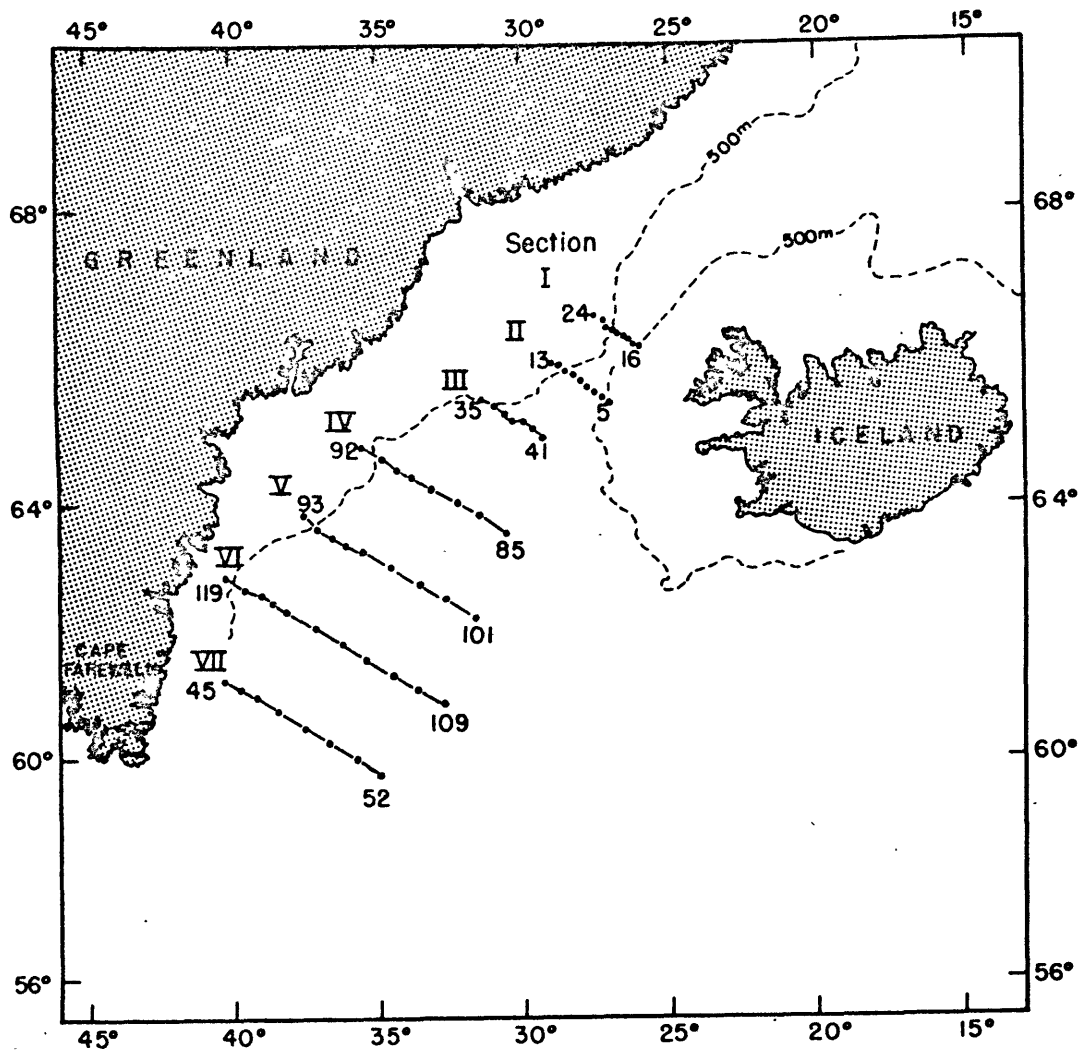


Figure 2-2. Locations of hydrographic sections for Norwegian Overflow data.

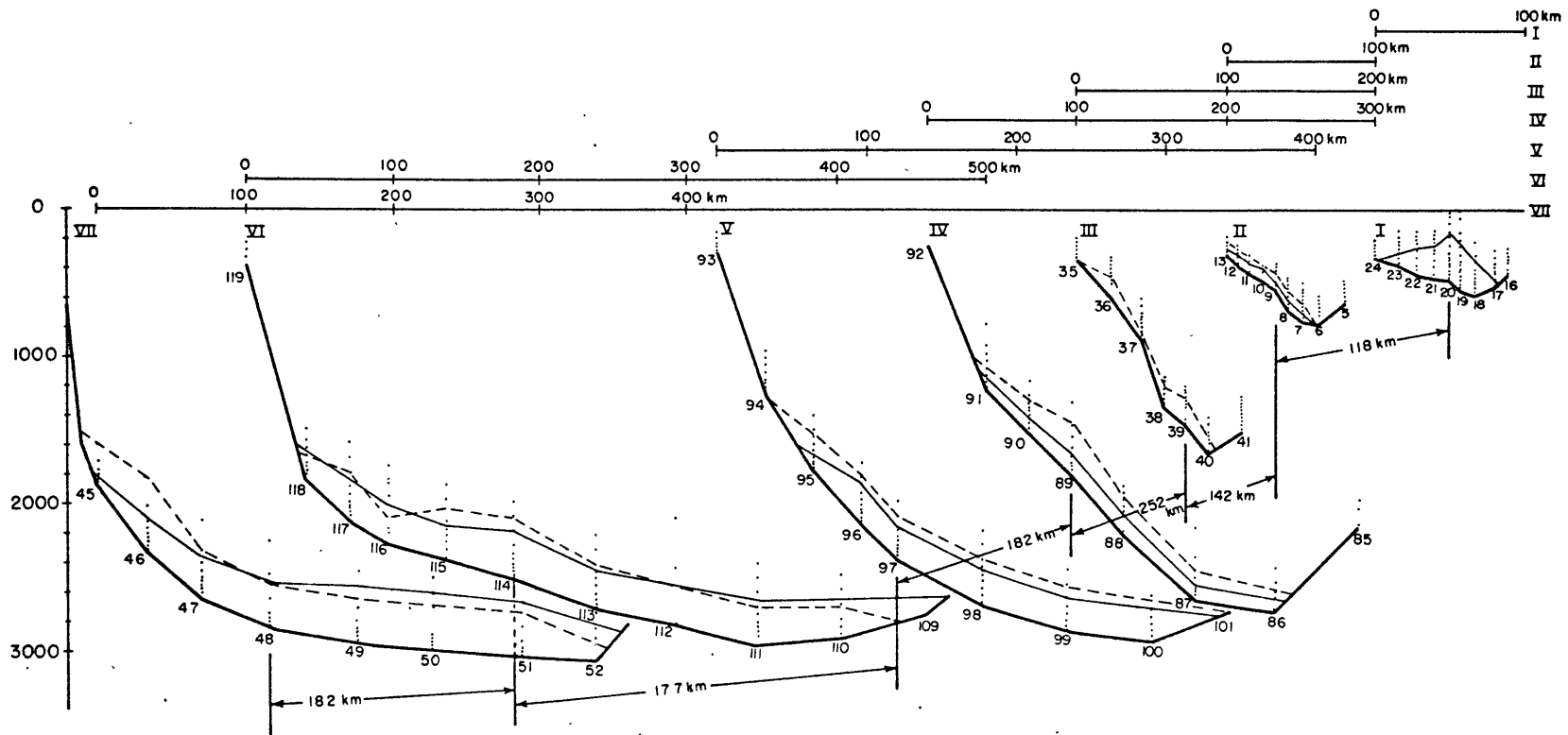


Figure 2-3. Cross-sections of Norwegian Overflow; ---- maximum extent of overflow water,
 ——— $\sigma_0 = 27.9$ contour.

curve represents the boundary of maximum vertical extent of the Norwegian Deep Water as determined by a detailed examination of the profiles of σ_{θ} , oxygen, and silicates. It is well known that the overflow waters are characterized by low concentrations of nutrients, especially reactive silicates, high oxygens, and, of course, large densities [Stefansson (1968)]. Typically, the profiles of potential density and the chemical tracers show a marked variation at some point near the bottom, below which these properties are relatively uniform (see Figure 2-4). The vertical extent of the outflow is defined by the top of this gradient, where the oxygen and silicates, in particular, take on values characteristic of the local environment. The potential temperature-salinity diagrams for these stations indicate that these contours contain pure Norwegian sea water which has been degraded by mixing with the Atlantic water, the East Greenland Current and water derived from the Iceland-Scotland overflow [Mann (1969)]. Figure 2-3 also illustrates one of the fundamental difficulties in fashioning a steady model after observational data, namely the absence of $\sigma_{\theta}=27.9$ water at Section III. According to Mann (1969), this observed variability in composition may be ascribed to the fact that waters from different depths in the Norwegian Sea flow over the sill at different times. This conclusion is supported by other observations of radical changes in the thickness of the overflow layer in the Denmark Strait over a period of hours [Harvey (1961)]. However, in terms of the stream dynamics, it is significant that a small but distinct density contrast and trace element anomalies are evident along the slope at this section, indicating that a weak flow still exists. Furthermore, except for this section, the continuity

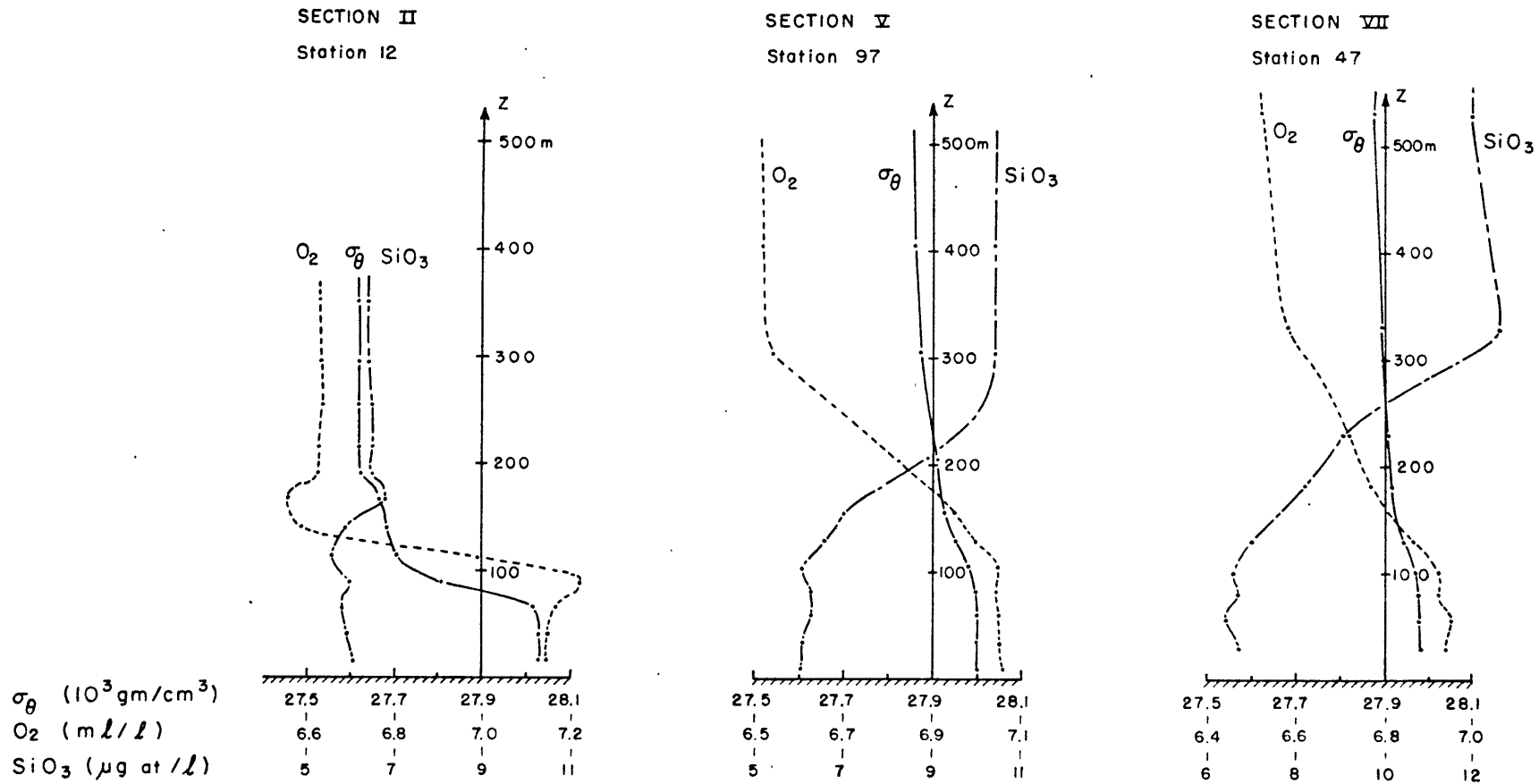


Figure 2-4. Profiles of potential density (σ_θ), oxygen, and silicates for typical stations in the Norwegian overflow.

of average flow properties does not seem to be broken. Therefore, it may be argued that the drastic departure of Section III from the overall pattern results from an isolated cutoff of Norwegian Deep Water at the sill and that further evidence of temporal variability of the source conditions or the flow itself remains at or below the noise level of the measurements. Hence, data from Section III is incompatible with data from other sections and will not be considered in the following comparison. Explicitly, it is assumed that the break in flow pattern at this point represents a local disturbance which propagates along the stream exerting a relatively minor effect on the average flow properties in other segments of the stream or on the overall dynamical characteristics such as the path of the stream.

In order to produce a meaningful comparison with theory, the physical constants appearing in the model equations as well as the average flow properties must be extracted from the hydrographic data in a way that is consistent with the premises on which the model is based. First of all, the bottom slope, $S = \tan \alpha$, was computed by fitting a straight line across each section through the observed depths of all stations at which overflow water was present. The mean slope was then obtained by averaging over all sections. Secondly, the mean Coriolis parameter was taken to be twice the value of the vertical component of the Earth's rotation near the center of the outflow current at a latitude of 64° N. Also the stratification of the ambient fluid was determined by fitting a straight line to the density field adjacent to the overflow water at several typical downstream stations. This procedure led to a quite small but stable value of the external stratification

rate, \hat{T} , and corresponding stratification parameter, γ . Finally, standard values were adopted for the gravitational acceleration, $\hat{g} = g \cos \alpha$, and characteristic density, ρ_0 . These physical properties of the system are compiled in Table I.

The measureable average flow properties are the density contrast, $\Delta \rho$, the cross-sectional area, A , and the pitch angle, β . Using the profiles of σ_θ , oxygen and silicates and the temperature-salinity diagram to distinguish the transition between overflow and adjacent waters, the density contrast at each station was determined as the maximum difference in potential density across the interface, i.e., between the density at the top of the strong gradient in properties and the maximum interior value. The station values were then averaged over each section to obtain a sectional mean density contrast. However, in most cases it was found that these average values were severely degraded by the small differences observed at stations near the edges of the flow and that the estimates were, therefore, not truly representative. To counterbalance this effect, the value of $\Delta \rho$ used for the comparison with the streamtube model is the average between the density contrast at the core station (maximum $\Delta \rho$) and the sectional mean value. This procedure tended to weight the relatively uniform values at and about the core station more heavily in the estimate. An attempt was also made to refine the values of $\Delta \rho$ at each station by integrating graphically the area between the observed density profile and the extrapolated ambient density profile and then dividing by the thickness of the overflow layer to obtain a true vertically-averaged density contrast. The results derived by this technique for stations near the axis of the flow agreed quite well with the

TABLE I. Physical Constants, Initial Conditions and Scales for the Norwegian Overflow Comparison

<u>Quantity</u>	<u>Symbol</u>	<u>Value \pm Error</u>
Bottom Slope	$s = \tan \alpha$	$(.58 \pm .26) \times 10^{-2}$
Coriolis Parameter	$\hat{f} = 2\Omega \cos \alpha$	$(1.30 \pm .04) \times 10^{-4}/\text{sec}$
Ambient Stratification Rate	$\hat{T} = T \cos \alpha$	$(.66 \pm .09) \times 10^{-9}/\text{cm}$
Dimensionless Stratification Parameter	$\gamma = s^2 \frac{gT}{f^2}$	$(1.29 \pm .18) \times 10^{-3}$
Characteristic Density	ρ_o	1.00 gm/cm^3
Gravitational Acceleration	$\hat{g} = g \cos \alpha$	$980. \text{ cm/sec}^2$
Initial Density Contrast	$\Delta\rho_o$	$.38 \times 10^{-3} \text{ gm/cm}^3$
Initial Value of Cross-sectional Area	A_o	7.84 km^2
Initial Pitch Angle	β_o	.112
Initial Velocity	V_o	16.0 cm/sec
Geostrophic Velocity Scale	$U = \frac{sg\Delta\rho_o}{\rho_o f}$	16.6 cm/sec
Topographic Length Scale	$L = U/f$	1.28 km

sectional mean values; however, these estimates were very sensitive to the layer thickness chosen and varied radically near the edges of the flow where there was little excess density. This method was, therefore, rejected because of its inability to produce stable estimates of average contrasts of the cross section. In summary, the density contrast used in the streamtube model comparison was computed by averaging the potential density difference observed at the core station (maximum value) with the sectional mean of those differences. This method is simple and relatively unambiguous and leads to stable values of the average density contrast for each section.

The area of the stream cross section was computed by graphically integrating the area between the dashed curve and the smoothed bottom contour in Figure 2-3. By this technique irregularities in the true bottom topography were neglected and the cross-stream profile encompasses all of the water whose origin could be traced to the Norwegian Sea. Furthermore, at each section the axis of the stream was assumed to pass through the core station where the maximum density contrast was observed. In most cases, this point nearly coincided with an alternate criterion, the centroid of the cross-sectional area, and differences between the two could be used as a measure of the error involved in the estimate. Once the path of the axis was determined, the average pitch angle between sections could be measured.

When the hydrographic data had been reduced to the appropriate set of average flow properties, the initial conditions were selected and the numerical solutions to equations (2.20) to (2.25) were computed. Due to the distortion of the outflow profile at Section I by the presence of the East Greenland Current, the flow properties at Section II were adopted as initial conditions. In fact, the integration may be started at any point in the stream since ξ

does not appear explicitly in the equations. Furthermore, since there were no velocity data available, the initial velocity was assumed to be in geostrophic balance, i.e.,

$$\bar{V}_0 = \frac{S \hat{q} \Delta \rho_0}{\rho_0 \hat{f}} \cos \beta_0 \quad (2.55)$$

The initial pitch angle, β_0 , was derived from the path of the stream between Sections I and II. The values of all the initial conditions plus the corresponding velocity and length scales are tabulated in Table I.

Starting with estimates of the empirical constants (E_0 , K) obtained by matching initial trends in the data with approximate solutions for the case $\bar{\delta}, \bar{\chi} \ll 1$, $\gamma = 0$, optimum values for E_0 and K were sought by trial and error. The numerical solutions are compared to the average flow properties derived from the hydrographic data in Figures 2-5 to 2-7. It is found that all the observations can be adequately fit with a unique pair of empirical constants,

$$(E_0, K) = (.065, 15) \text{ km} . \quad (2.56)$$

Furthermore, all the data points may be encompassed by varying these optimum values by less than a factor of two.

Figure 2-5 shows a comparison of the average density contrasts. As expected, $\Delta \rho$ is found to be a strong function of the entrainment rate, but depends weakly on the magnitude of the friction coefficient. The error bars on the data points represent the difference between the density contrast observed at the flow axis and the sectional mean value. Next, the path of

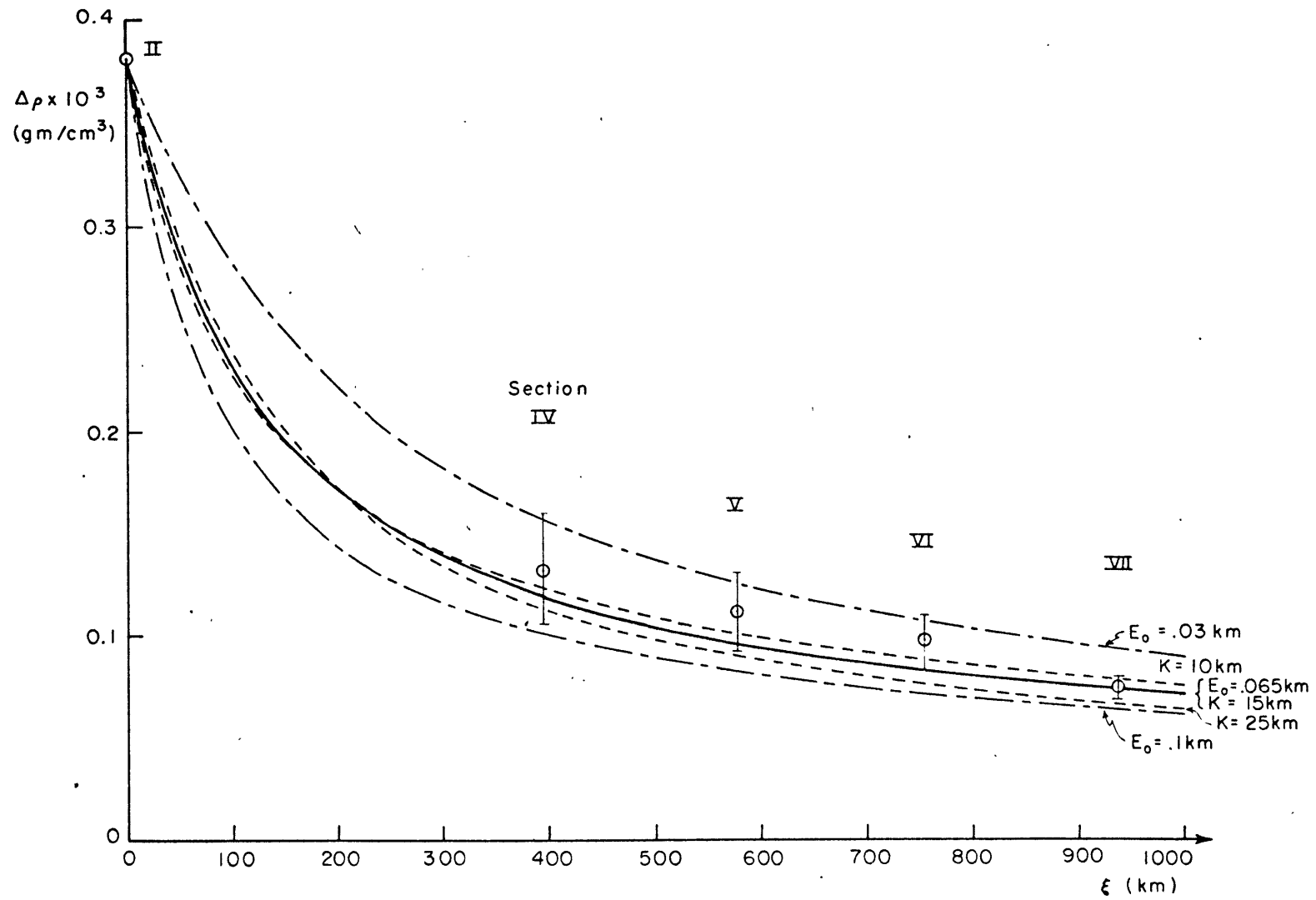


Figure 2-5. Comparison of average density contrast in Norwegian Overflow data with streamtube model results for several parameter pairs (E_0, K).

the stream is plotted in bottom-fixed coordinates in Figure 2-6. The coordinates (X, Y) of the observed stream axis were computed from geometrical relations using the depth of the core station and the mean bottom slope. This calculation implicitly involves the mean pitch angles between sections. The error bars on the data points reflect the uncertainty in the axis position as measured by the distance between the core station and area centroid at each cross section. The trajectory of the stream axis is controlled strongly by both the friction and entrainment constants. In Figure 2-7, the rate of increase of cross-sectional area is seen to depend heavily on the entrainment rate, but weakly on the strength of friction. The error bars attached to the observational points represent uncertainty in the area measurements as determined from the difference in the areas under the solid and dashed curves in Figure 2-3.

Lastly, for the sake of completeness, the theoretical mean velocity distribution along the stream is presented in Figure 2-8. The locations of Sections IV to VII are also indicated. According to this prediction, the average current drops very rapidly near the source from its initial value, $V_0 = 16.0 \text{ cm/sec}$, to a value of 10.8 cm/sec just 10 km . downstream, then diminishes gradually to a value of 3.26 cm/sec at Section VII. Combining this information with the cross-sectional area results indicates that the volumetric flow rate of the outflow current,

$$Q(x) = AV, \quad (2.57)$$

has increased from a value of $1.3 \times 10^6 \text{ m}^3/\text{sec}$ at the source to roughly $4.6 \times 10^6 \text{ m}^3/\text{sec}$ at Section VII. In his water budget for the Norwegian Sea, Worthington (1970) used estimates obtained from dynamic computations

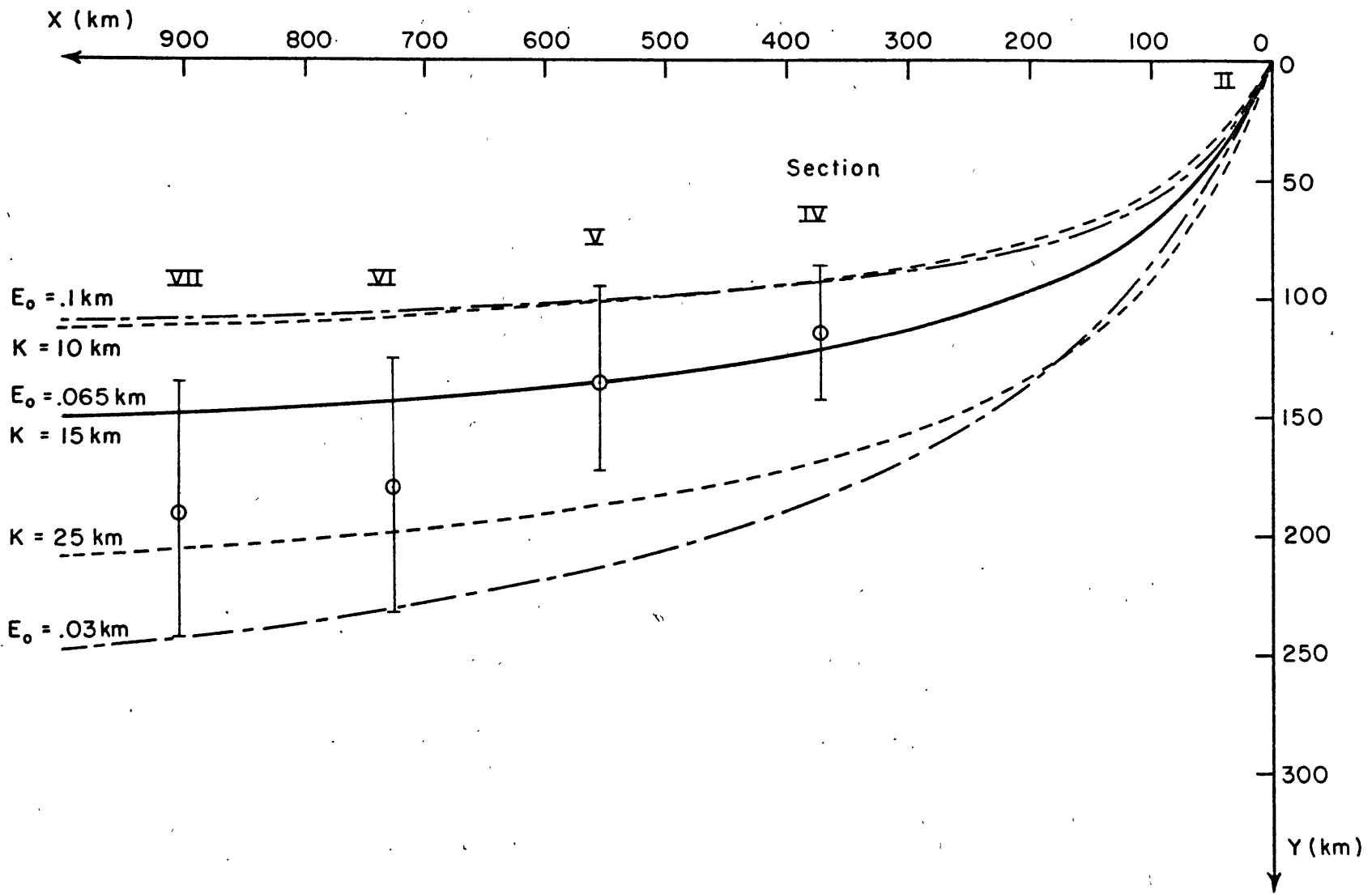


Figure 2-6. Comparison of observed path of stream axis for Norwegian Overflow with streamtube axis for several parameter pairs (E_0, K) .

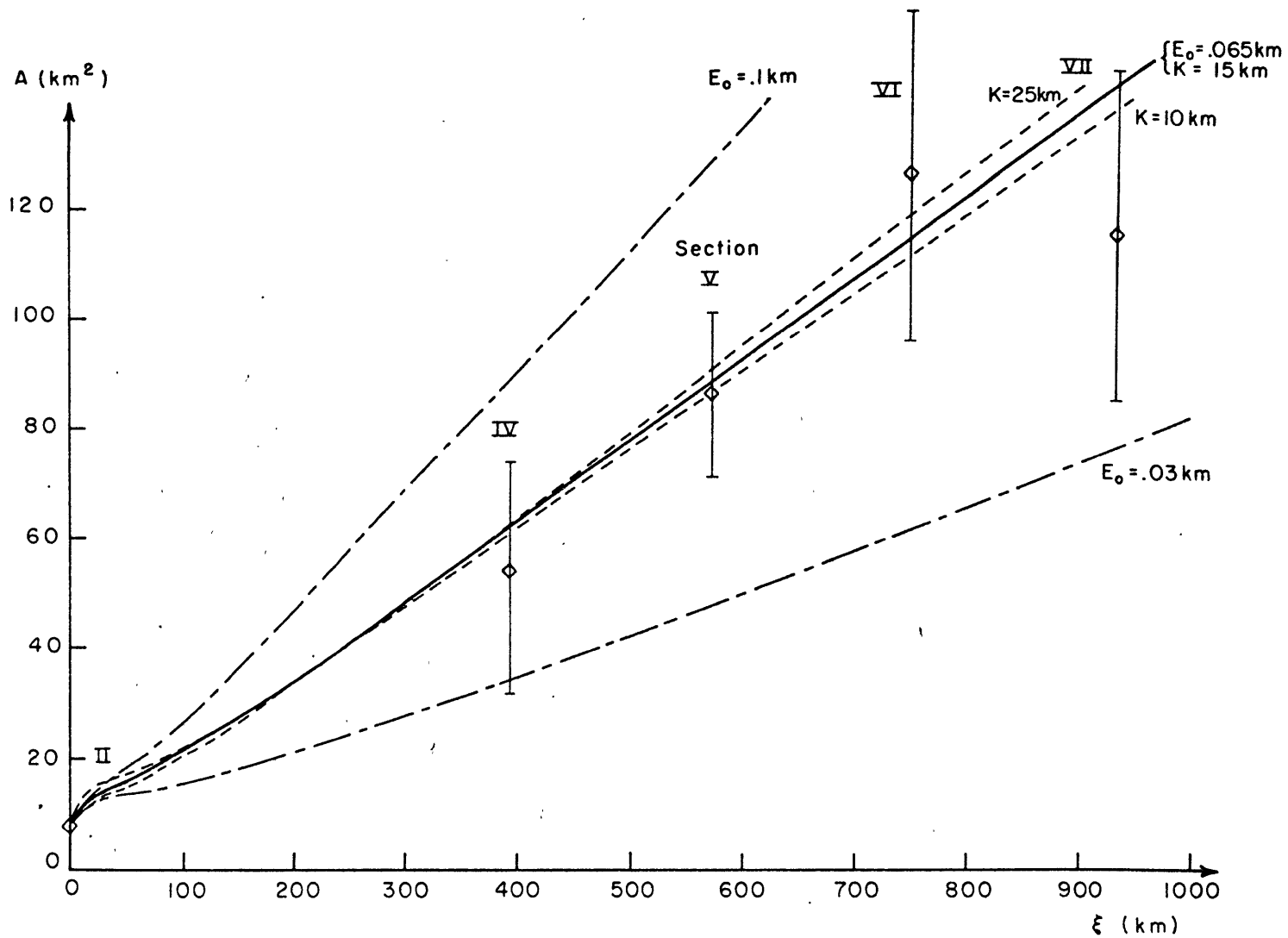


Figure 2-7. Comparison of cross-sectional area variation for Norwegian... Overflow data with streamtube model results for several parameter pairs (E_0, K).

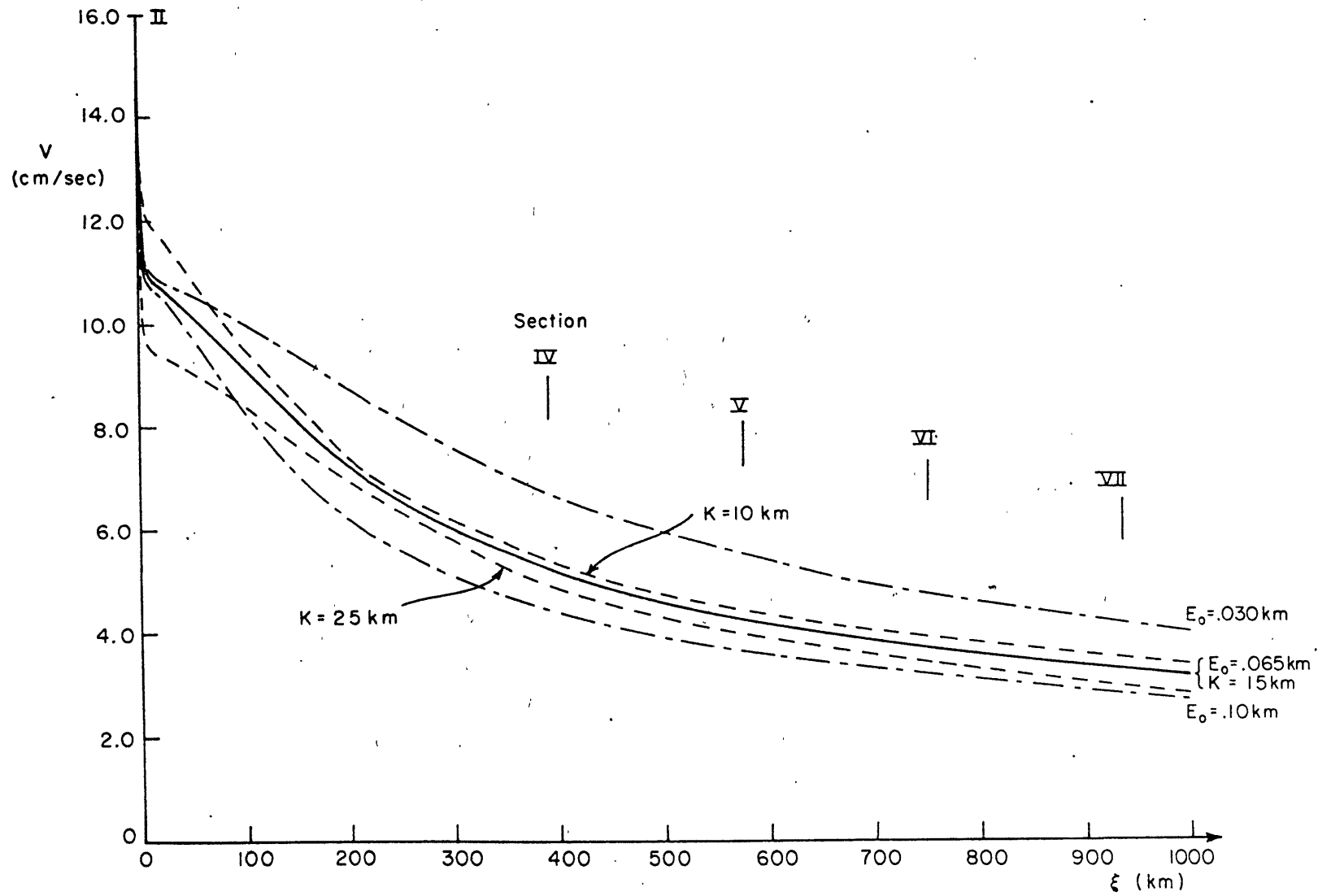


Figure 2-8. Theoretical mean velocity distribution for several parameter pairs (E_0, K) .

and neutrally buoyant float measurements to arrive at transport values of $4 \times 10^6 \text{ m}^3/\text{sec}$ for the Denmark Strait overflow and $10 \times 10^6 \text{ m}^3/\text{sec}$ for the total transport southwest of Greenland. Each of Worthington's values exceeds the corresponding value here but the ratios of the two, i.e., the factors by which the transport is enhanced due to entrainment, are roughly comparable. Moreover, in a separate computation designed to match a transport value of $4 \times 10^6 \text{ m}^3/\text{sec}$ at the source ($V_0 = \frac{Q_0}{A_0} = 51 \text{ cm/sec}$), the transport grew to a value of $9.3 \times 10^6 \text{ m}^3/\text{sec}$ at Section VII using the same optimum pair of coefficients (E_0, K). This fact is further evidence of the consistency of this model with observational data.

The numerical solutions may be interpreted with knowledge of the values of the modified entrainment and friction parameters,

$$\bar{\delta} = 0.011, \quad (2.58)$$

and

$$\bar{\chi} = 2.54, \quad (2.59)$$

which correspond to the optimum values of the empirical constants, $(E_0, K) = (.065, 15) \text{ km}$. First of all, the strong frictional influence indicated by the value of $\bar{\chi}$ accounts for the absence of oscillations in the flow properties and stream path near the source. Instead, the velocity and cross-sectional area change rapidly from their initial values to levels appropriate to the non-entraining downstream limit

$$V = 11.3 \text{ cm/sec},$$

$$A = 10.3 \text{ km}^3.$$

The initial pitch angle likewise adjusts to its limiting value,

$$\beta = .94 .$$

The density contrast, on the other hand, is invariant in the non-entraining limit. It, therefore, undergoes no drastic changes in the source region but varies smoothly over the entire length of the stream. The sharpest decrease in $\Delta\rho$ occurs within a distance of 100 or 200 km. from the source, which corresponds generally to an entrainment length scale introduced in (2.34), namely $\xi_E = L/\bar{\delta} = 106 . \text{ km}.$

The character of the downstream variations of $\Delta\rho$, V , β , and A , and their dependence on the value of E_0 , suggest the asymptotic behavior of the stream is controlled by the entrainment with a weak frictional influence. In fact, quantitative comparison of the linear variation in cross-sectional area reveals that the slope of the numerical solution (.15 km²/km) between Sections V and VI differs from that in the limiting case,

$$\frac{dA}{d\xi} = 2H_0' \bar{\delta} L_1 = .13 \text{ km}^2/\text{km} .$$

Moreover, the inverse square root dependences of $\Delta\rho$ and V do not hold exactly and the trend in β is different from that predicted by (2.48). However, a special computation for the case of $\hat{T} = 0$ reveals that these discrepancies can be fully accounted for by the presence of a weak ambient stratification. It may be concluded, therefore, that the behavior of the solutions in the downstream region is strongly controlled by the entrainment parameter, $\bar{\delta}$. The transition to this state appears to occur somewhat before $\xi_T = 500 \text{ km}.$, which is predicted by equation (2.49) for $\beta_T = 0.1.$

The pronounced influence of the strength of friction on the path of the stream axis is anticipated from the direct dependence of the pitch angle on $\bar{\chi}$ for all limiting cases in which it is non-zero. The dependence on E_0 , however, is related to the damping of the flow by entrainment and may be explained qualitatively by reference to (2.49). For fixed $\bar{\chi} \ll 1$, strong entrainment (large $\bar{\delta}$) helps damp the velocity and causes a rapid transition to the asymptotic state of flow along bottom contours. If the entrainment is weak, however, the transition is delayed, thereby allowing the axis a larger excursion downslope.

Finally, with regard to the effects of ambient stratification, the results of the computation for $\hat{T} = 0$ mentioned above showed relatively minor differences (not exceeding 25%) in the flow properties at Section VII from those corresponding to the stratified case, accompanied by a slight shift of the stream axis downslope.

II.4 Comparison with Mediterranean Outflow Data

The data selected to define the structure of the Mediterranean Outflow comes from two sources. The first is a comprehensive hydrographic survey and current measurement program conducted by Madelain (1970) aboard the Jean Charcot during April and May of 1967. Accompanying a fine series of hydrographic sections run across the outflow current are records from ten current meter moorings from which a set of five has been chosen to represent the mean velocity structure of the outflow current. The second source is some unpublished hydrography data taken by F. C. Fuglister aboard the R.R.S. Discovery II in November, 1958. In these observations, as with Mann's survey of the Norwegian Overflow, great care was taken to resolve accurately the properties of the outflow water, and bottle spacing near the bottom (within 5 to 40 meters) was usually 25 meters. The temperature and salinity profiles for the Fuglister sections have been compiled and published by Heezen and Johnson (1969). In addition, these authors present a summary of four documented sets of current observations taken in the Gulf of Cadiz. The results of these measurements are found to be entirely consistent with the velocities quoted by Madelain. Notice that the use of two sets of data taken nine years apart represents a strong test of the assumed permanence of the flow field.

Upon inspection of the Mediterranean outflow data, several important differences are immediately apparent between this current and its counterpart in the Northwest Atlantic. First of all, the outflow water is recognized most readily by its distinctive high salinity, rather than strong anomalies of temperature, oxygen, or dissolved nutrients. Although salinity values ex-

ceeding 38‰ in the Straits of Gibraltar are severely degraded due to entrainment by the time the flow reaches Cape St. Vincent, the difference between the core salinity and that of the local environment never falls below .4‰ along the Spanish continental slope.

Secondly, it is evident that bottom topography exerts a strong influence on the course and integrity of the stream. In his analysis of the Jean Charcot data, Madelain (1970) demonstrates that the stream is fragmented by the rugged topographic features, with separate veins detouring down submarine canyons then coalescing again further downstream. Indeed, at one point, the flow is divided into three branches separated by two large peaks. Yet, despite these irregularities, the average bottom slope remains fairly uniform along the entire Spanish continental margin. Moreover, in the regions where the bottom water of highest salinity is found, the salinity contours lie roughly parallel to the mean bottom slope. Dynamically, this implies that geostrophic bottom currents, though splintered by the local topography, are guided in an overall sense by the mean bottom slope, which also controls their magnitude.

Finally, a phenomenon unique to this outflow is the observed departure of the main body of the flow from the bottom as it nears Cape St. Vincent [Heezen and Johnson (1969)]. Beyond this point, the current exists largely as an interflow and the applicability of the streamtube model in this region is highly questionable. In selecting the data for comparison, therefore, an attempt was made to focus on sections taken across the flow upstream from the breakaway point where the major portion(s) of the current is clearly bearing against the continental slope. This criterion was violated at the final

section along $8^{\circ}30'W$, since only two of the stations there show maximum salinity at the bottom. This section is included in the comparison, however, along with this qualification.

The tracks of the sections selected for comparison with the streamtube theory are plotted in Figure 2-9. The lines of stations cut across the current as defined by the map of bottom salinity maxima presented by Madelain (1970) and are roughly normal to the velocity vectors observed at the current meter stations. In Figure 2-10, cross sections of the stream are displayed over a highly smoothed bottom. The outflow water is delineated by two salinity contours. The inner (dashed) curve, the 36.4‰ contour, seems to enclose the main body of the outflow, while the solid contour (36.0‰) represents the maximum vertical extent of Mediterranean water at each station. Following the procedure outlined in the previous section, cross-sectional areas are computed on the basis of maximum extent of the outflow water, while the second curve is used to estimate the uncertainty of the measurement.

Also shown in Figure 2-10 is the deployment of the five current meters used for the velocity comparison. The current meters used were Mecabolier-type and each meter, with the exception of C.1, is located deep in the outflow water near the stream axis. The average current speed at each current station was assumed to represent the mean flow velocity in the stream at that section while the variations about the average speed were used to assess its accuracy. The general compatibility of these estimates with other hydrographic data from the area is indicated by comparing the volumetric flow rate $Q = A_o V_o = 2.02 \times 10^6 \text{ m}^3/\text{sec.}$, calculated at Section I with Lacombe's estimates of the geostrophic transport in the Strait of Gibraltar, which ranged from 0.72 to $1.57 \times 10^6 \text{ m}^3/\text{sec}$ [see Madelain (1970)].

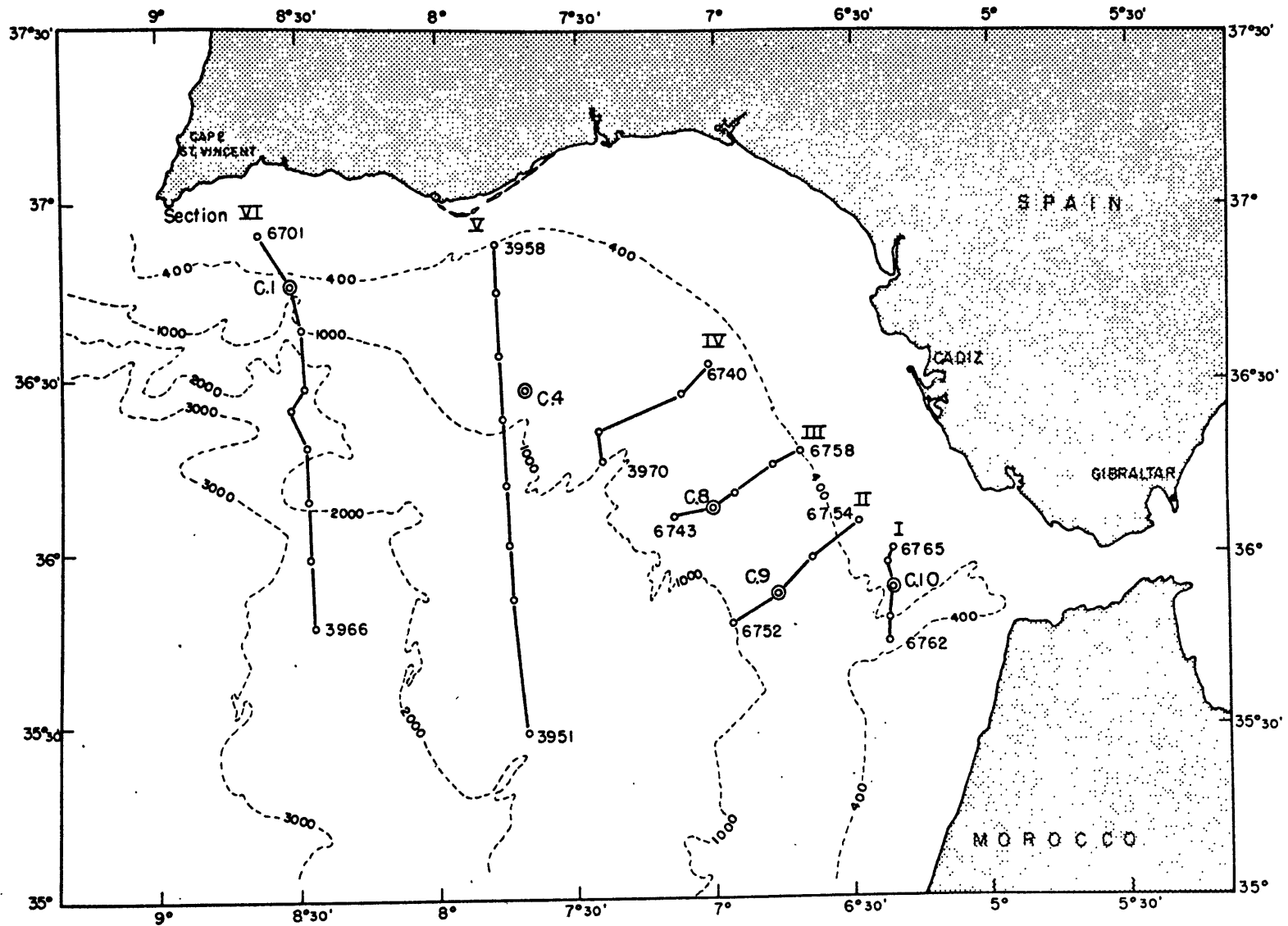
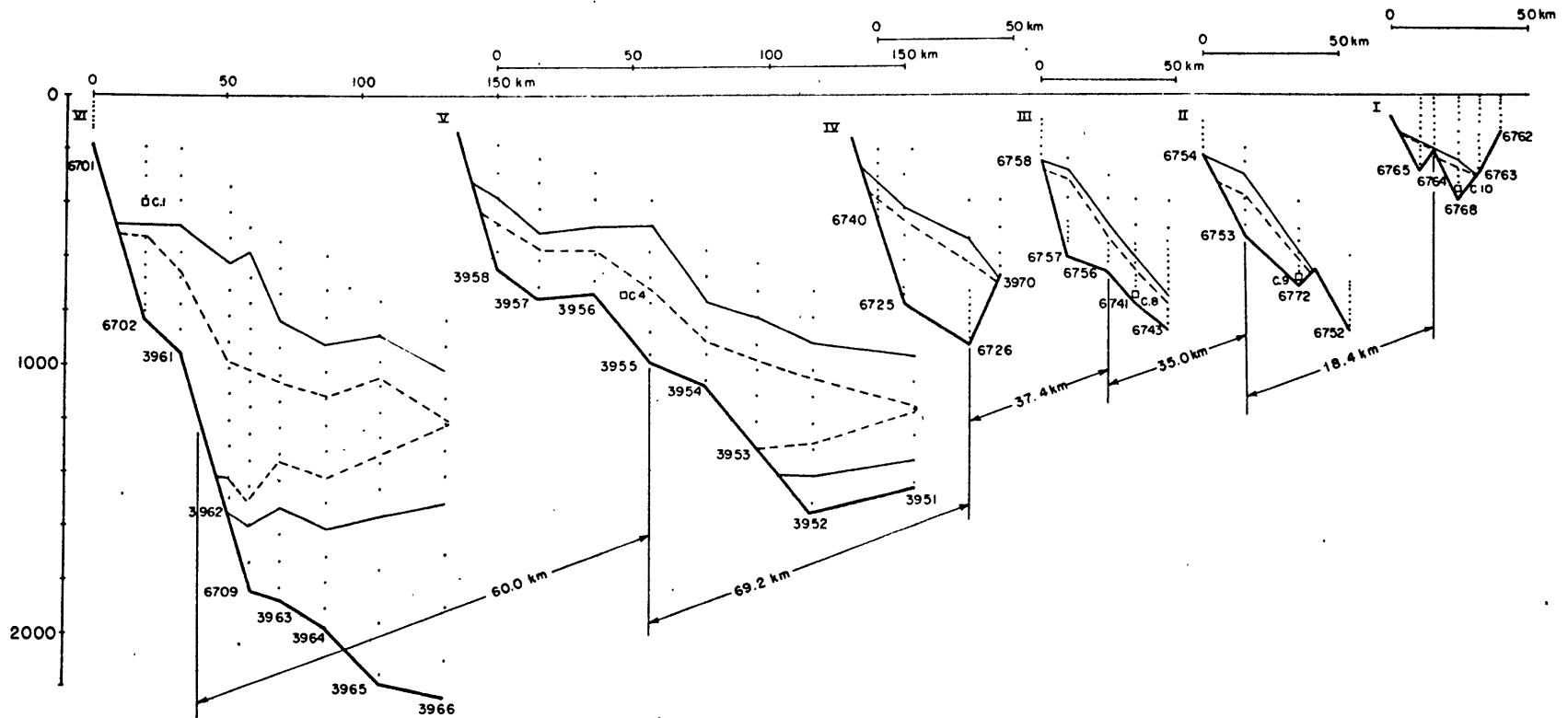


Figure 2-9. Locations of hydrographic sections for Mediterranean Outflow data.



. Figure 2-10. Cross-sections of Mediterranean Outflow; ——— 36.0 ‰ salinity contour, - - - - 36.4 ‰ salinity contour.

The physical constants required by the streamtube model were computed for this case as they were for the Norwegian Overflow and their values are given in Table II. Of particular interest is the relatively large vertical stratification rate, \hat{T} , and the correspondingly high stratification parameter, γ . Based solely on the relative values of γ , it is expected that the nonhomogeneous environment will play a more significant role here than it did for the Norwegian Outflow, provided the frictional forces are comparable.

The presence of a strongly varying external density field made the calculation of the mean density contrast more difficult than before since the differences had to be computed between the actual density profile and the extrapolated ambient density profile. However, the transition to Atlantic water was usually well marked at each station by a distinct salinity minimum or at least a rapid change in the salinity gradient. Within this boundary, the mean density profile showed the maximum deviation from the ambient density field, whether that point occurred at the bottom or somewhere above the bottom for stations in the interflow. This difference was chosen to represent the mean density contrast for that station. The sectional mean values were then derived by averaging across the outflow profile. Finally, these results were averaged with the maximum contrast at the core station to obtain the value which weights the core more heavily for use in the comparison.

The path of the stream axis was defined to be the trajectory connecting the core stations of each section except at Section VI where an insufficient number of stations caused the axis to be located between two stations near the depth of the centroid of the cross-sectional area.

TABLE II. Physical Constants, Initial Conditions, and Scales for the Mediterranean Outflow Experiment

<u>Quantity</u>	<u>Symbol</u>	<u>Value \pm Error</u>
Bottom Slope	$s = \tan \alpha$	$(1.43 \pm .40) \times 10^{-2}$
Coriolis Parameter	$\hat{f} = 2\Omega \cos \alpha$	$(.854 \pm .060) \times 10^{-4}/\text{sec}$
Ambient Stratification Rate	$\hat{T} = T \cos \alpha$	$(1.00 \pm .15) \times 10^{-8}/\text{cm}$
Dimensionless Stratification Parameter	$\gamma = s^2 \frac{gT}{f^2}$	$.275 \pm .041$
Characteristic Density	ρ_o	1.00 gm/cm^3
Gravitational Acceleration	$\hat{g} = g \cos \alpha$	$980. \text{ cm/sec}^2$
Initial Density Contrast	$\Delta\rho_o$	$1.25 \times 10^{-3} \text{ gm/cm}^3$
Initial Value of Cross-sectional Area	A_o	2.10 km^2
Initial Pitch Angle	β_o	$.7185$
Initial Velocity	V_o	96.0 cm/sec
Geostrophic Velocity Scale	$U = \frac{sg\Delta\rho_o}{\rho_o f}$	205.1 cm/sec
Topographic Length Scale	$L = U/f$	24.02 km

Choosing mean values from Section I as initial conditions (see Table II), the numerical search for the optimum values of the empirical constants yields,

$$(E_0, K) = (.05, .5) \text{ km.} \quad (2.60)$$

The detailed comparison of the average properties and path of the stream is presented in Figures 2-11 to 2-14. Overall the agreement between data and theory is reasonable. However, due to the qualifications with regard to the way the data was reduced (e.g., neglecting influence of bottom topography), the quality of the fit is not as good as that for the Norwegian Overflow.

All of the velocity and density contrast data are covered well by the range of numerical solutions, and the trends in the two seem to be quite consistent. The most outstanding disagreement occurs in the comparisons of cross-sectional area (Figure 2-14) and path of the stream axis (Figure 2-12). The apparent lack of continuity between the measured areas at Sections V and VI and those at upstream sections may be explained in part by the fragmentation of the stream. According to Madelain (1970), a small secondary vein of outflow water escapes down a submarine canyon at Section III but rejoins the main stream again by Section V. Thus, the value of A measured at Section IV would underestimate the area of the entire stream cross section. Furthermore, the profiles observed at Sections V and VI include portions of the interflow, which leads to overestimates of the cross section of the pure bottom current. This uncertainty is manifested by the significant differences between the areas bounded by the two salinity contours in Figure 2-10.

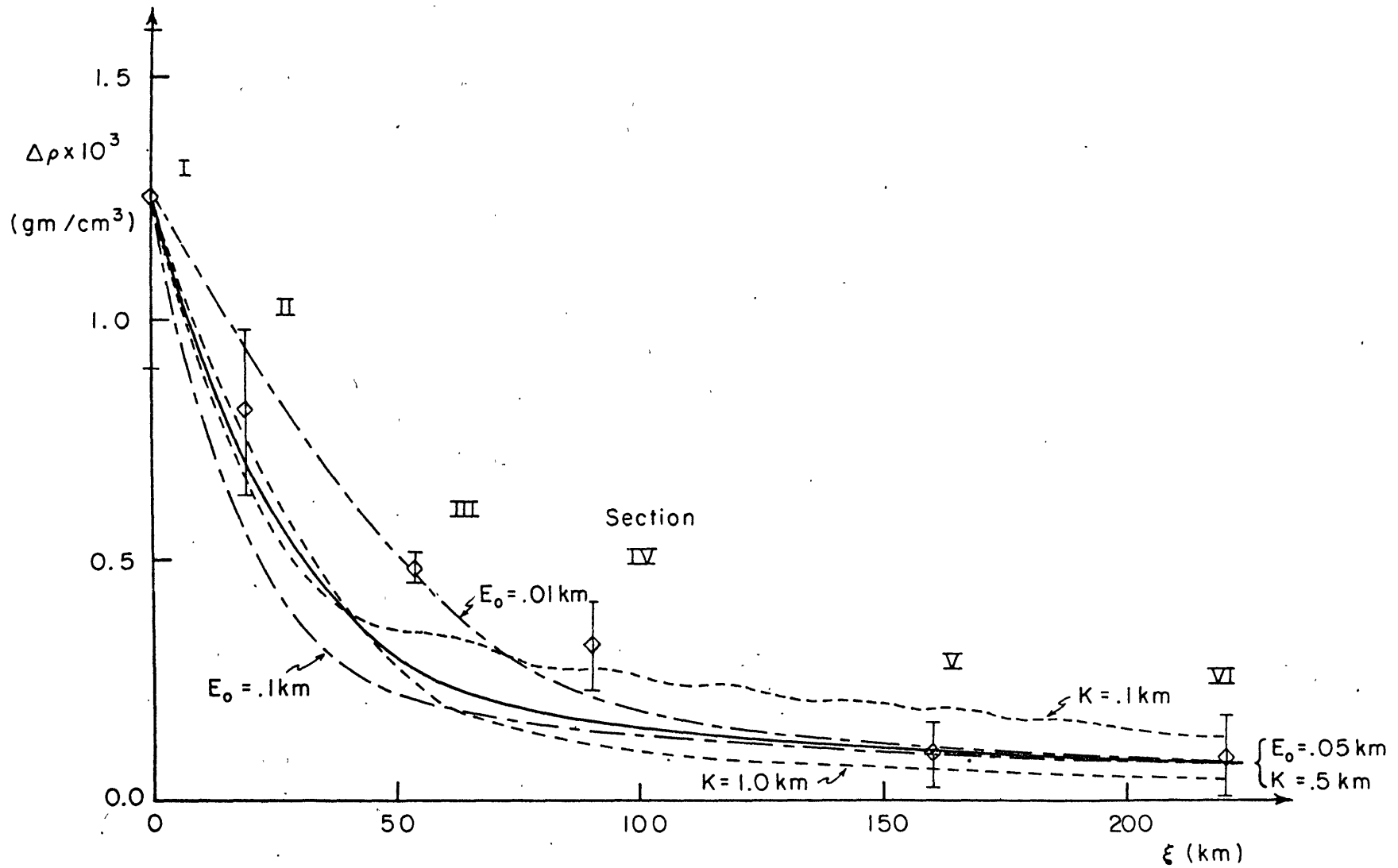


Figure 2-11. Comparison of average density contrast in Mediterranean Outflow data with streamtube model results for several parameter pairs (E_0, K) .

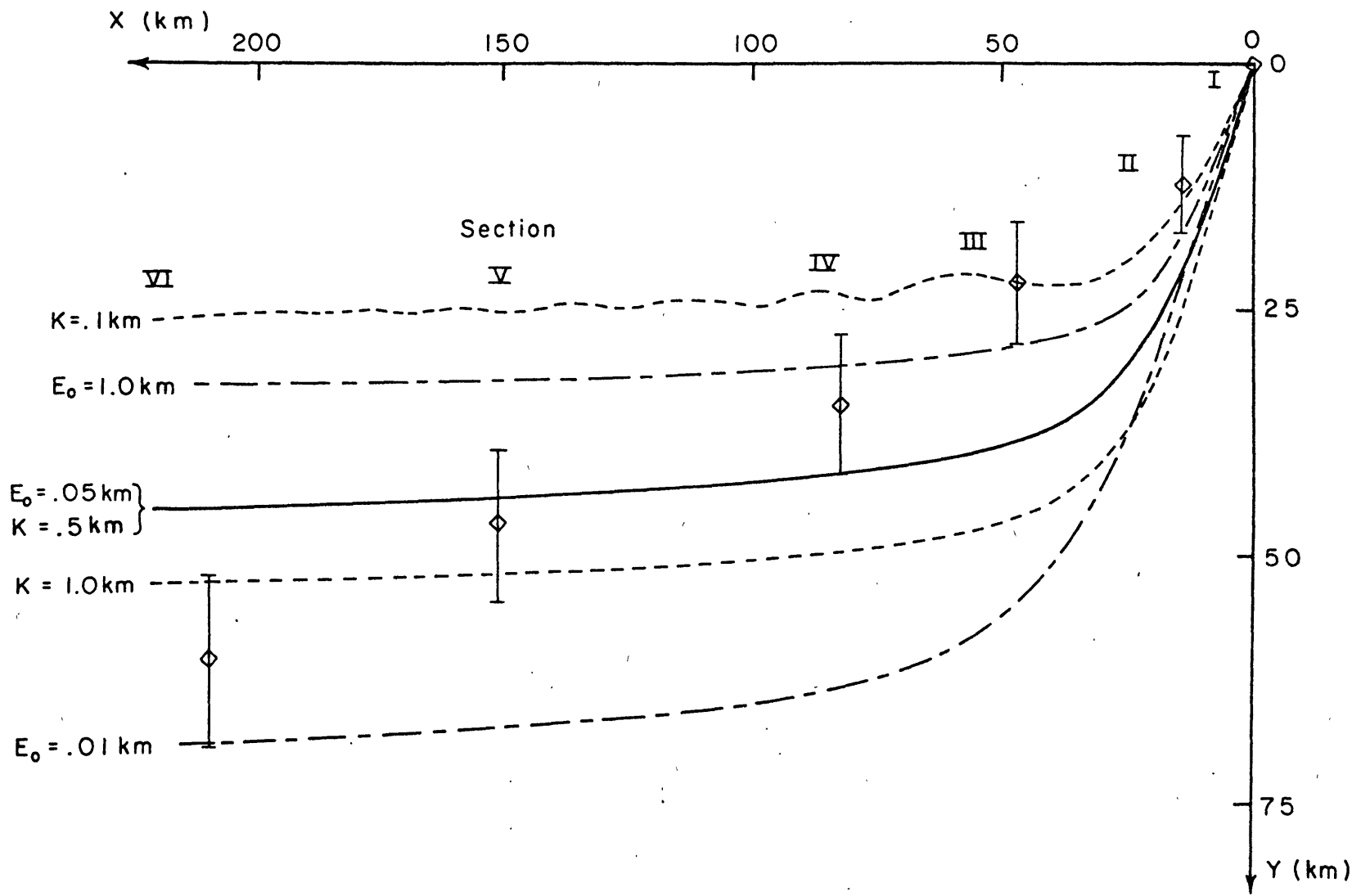


Figure 2-12. Comparison of observed path of stream axis for Mediterranean Outflow with streamtube model results for several parameter pairs (E_0, K).

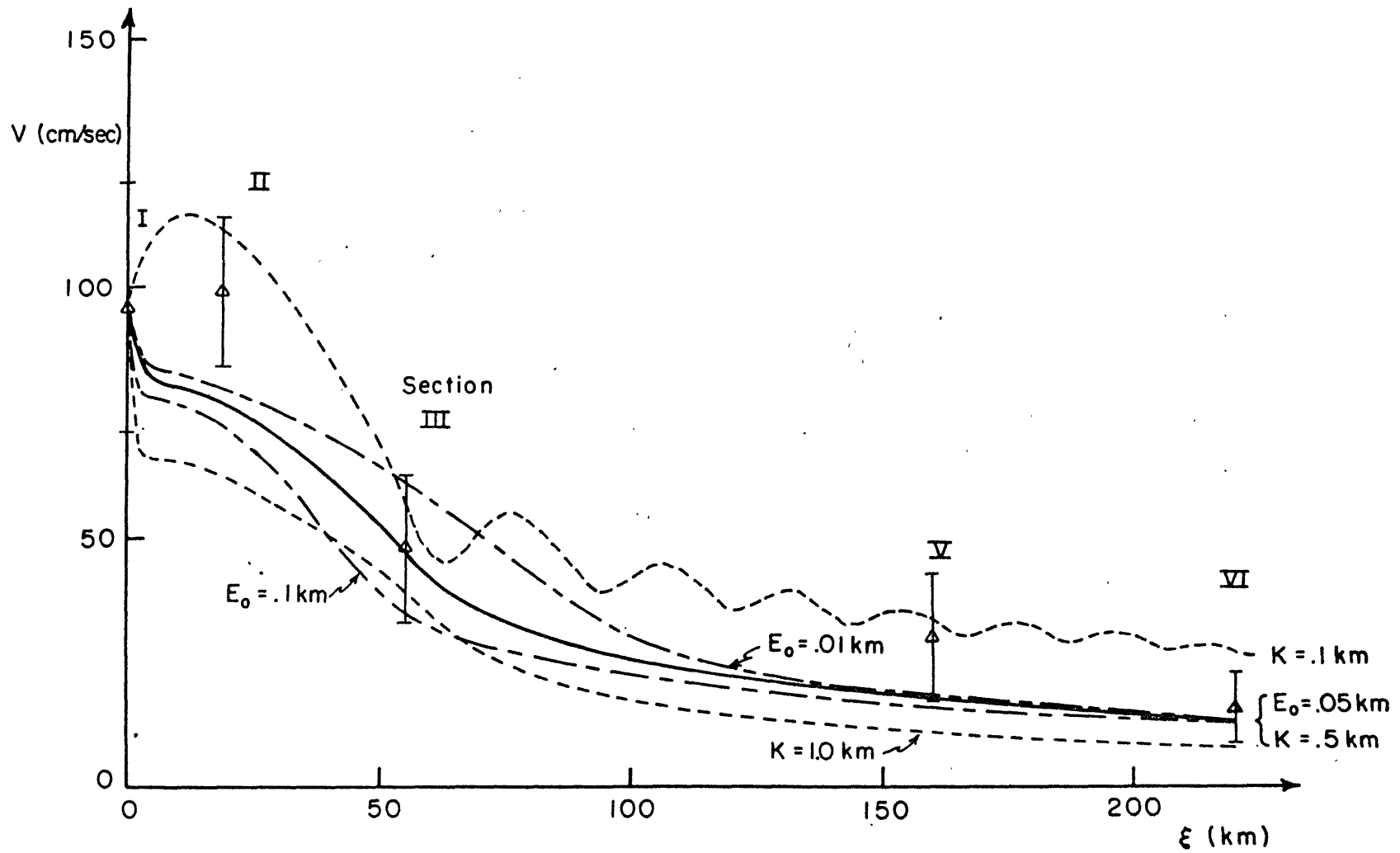


Figure 2-13. Comparison of velocity data for Mediterranean Outflow with streamtube model results for several parameter pairs (E_0, K).

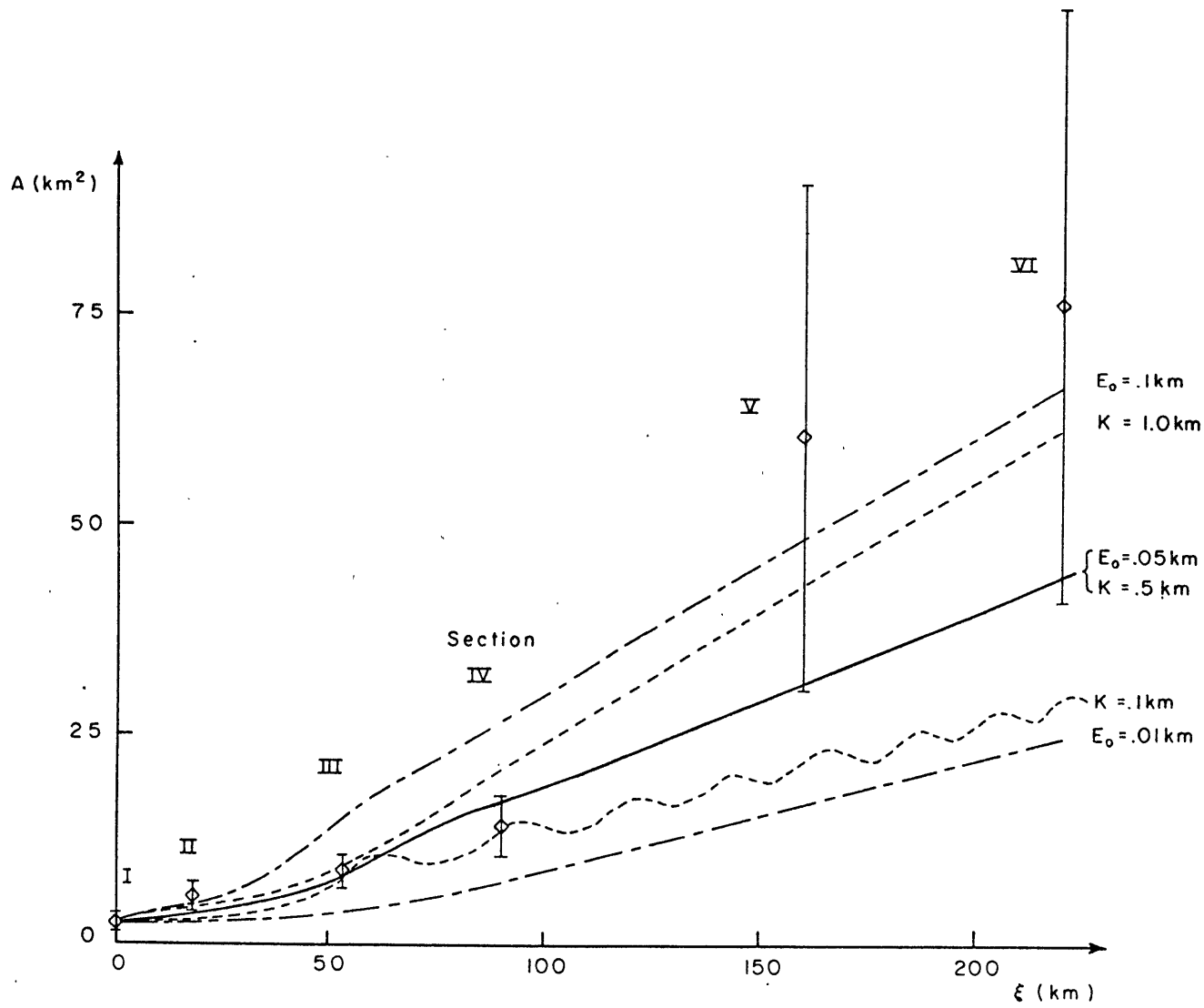


Figure 2-14. Comparison of cross-sectional area variation for Mediterranean Outflow data with streamtube model results for several parameter pairs (E_0, K) .

The lack of correspondence between the theoretical and observed path of the stream may also be attributed to the rugged bottom. In contrast to the secondary veins which plunge down canyons, there is evidence from the detailed topography at the upstream sections [Heezen and Johnson (1969)] that the descent of the main portion of the flow is blocked by high ridges, forcing the axis of the current to remain up on the slope. In light of these explanations, the agreement between the observed properties of the outflow and the streamtube theory is judged to be satisfactory and, therefore, the optimum values of (E_o, K) are said to characterize the entrainment and frictional processes in this outflow current.

A close examination of the numerical solutions used for this comparison reveals some further salient features of the streamtube model. The modified dimensionless parameters corresponding to $(E_o, K) = (.05, .5) \text{ km}$ are,

$$\bar{\delta} = 1.22, \quad (2.61)$$

and

$$\bar{\chi} = 12.2. \quad (2.62)$$

As with the Norwegian Outflow, the solution for this case is critically damped and the velocity, area and pitch angle attain their asymptotic levels for the non-entraining limit quite near to the source. However, for the minimum frictional coefficient considered ($K = 0.1 \text{ km}$), the value of $\bar{\chi}$ drops to 2.44 and a weak meander pattern appears. As evidenced by the mean velocity contour, the damping is still rather strong since the

amplitude of the oscillations diminishes rapidly with downstream distance. Moreover, the topographic wavelength ($2\pi L$) which would characterize meanders in the frictionless, non-entraining limit is 150 km. for this case. Therefore, it is clear that frictional effects considerably shorten the meander wavelength.

Also, notice that once again the flow variables exhibit features of the strong entrainment limit (modified by stratification) for downstream distances greater than 100 km. The predicted transition point from equation (2.49) for $\beta_T = 0.1$ is further downstream at $\xi_T = 242$ km., whereas for $\beta_T = 1.0$, the value is $\xi_T = 52.2$ km.

Finally, the expected importance of stratification of the ambient density field is confirmed by the results of a separate computation using the optimum values of (E_0, K) , but with $\hat{T} = 0$. In particular, the theoretical values at Section V are given by,

$$\begin{aligned} \Delta\rho &= .33 \times 10^{-3} \text{ gm/cm}^3, \\ A &= 143.0 \text{ km}^2, \\ V &= 53. \text{ cm/sec}, \\ (X, Y) &= (128, 88) \text{ km}, \end{aligned} \tag{2.63}$$

which differ drastically from stratified results plotted in Figures 2-11 to 2-14. The most dramatic difference occurs in the cross-sectional area where the value is increased by more than a factor of four. In addition, the density contrast and average velocity are raised substantially and the path of the stream is shifted downslope.

II.5 Concluding Remarks

Before proceeding, it is appropriate to make a few concluding remarks concerning the general character of the streamtube results and their implications about the nature of the two bottom currents.

First of all, it is clear that both outflows are characterized by the effects of turbulent friction and entrainment. In the vicinity of the source, strong frictional influence dominates the local dynamics: topographic meanders are critically damped, and the flow variables change rapidly from their initial values to levels appropriate to the non-entraining downstream limit. In each case, the constant properties associated with this limit are then gradually modulated by the relatively weak entrainment rate in such a way that the downstream behavior of the flow variables closely resembles that in the asymptotic limit dominated by entrainment. However, to separate the flow into two regimes is misleading since it tends to minimize the importance of the overall interaction between the two processes. For instance, numerical solutions for $\bar{\chi} = 0$ indicate that, in the absence of friction, neither outflow would reach this slowly modulating asymptotic state over the downstream range considered for the comparison. Instead the oscillations induced by the initial conditions persist over the whole domain. Moreover, the axis of the stream remains near the $Y = 0$ bottom contour in these computations. With respect to the corresponding results with friction, the density contrasts are significantly lower, and the velocity and area functions oscillate about higher and lower values respectively. In short, the entire character of the solution is changed when there is no friction. Indications of the onset of

this radically different behavior were observed in the numerical solutions for $K = 0.1$ km. in the Mediterranean Outflow comparison [Figures (2-11) to (2-14)]. Evidently, therefore, in addition to a relatively weak influence in guiding the flow and in determining the levels attained by the flow properties in the asymptotic limit, the crucial importance of the viscous forces lies in their ability to damp out irregularities in the source region and allow transition to the entraining downstream state.

Several important differences are noticed between the two outflow currents. As mentioned before, the strong stratification of the environment has a pronounced effect on the Mediterranean outflow while the weaker ambient gradient in the North Atlantic has little influence on the Norwegian overflow. Furthermore, strong frictional dissipation acting over a larger downstream scale allows the Norwegian Sea water to descend along the Greenland continental slope to the ocean floor, whereas the combination of entrainment and external stratification limits the descent of the Mediterranean current to a depth of approximately 1200 m. where the actual flow is observed to separate from the bottom and form an interflow. Finally, a larger total range in density contrast, accompanied by a much sharper decrease near the source, is observed for the Mediterranean case ($\bar{\delta} = 1.22$) than for the Norwegian case ($\bar{\delta} = .011$) despite the fact that the entrainment constants E_0 and parameters δ are roughly comparable. Therefore, as indicated by the approximate solutions, the modified entrainment parameter $\bar{\delta}$ is the appropriate measure of the strength of entrainment.

As noted at the beginning of this chapter, it is possible to compare

crudely the values of dimensionless friction and entrainment constants found in other oceanographic and laboratory applications with the corresponding values for the outflows by dividing the optimum values of E_o and K by observed cross-stream scales. The results of this computation are shown in Table III. The dimensionless friction coefficients for the two outflows ($k_N = .15$, $k_M = .01$) bracket the value of .03 which was used by Bowden (1960) and, according to Defant (1961), is an appropriate value for turbulent bottom currents of this scale. The dimensionless entrainment coefficient e_o is known to be a function of the stability of the two-layer system, which was measured in the experiments of Ellison and Turner (1959) by an overall Richardson number

$$Ri_o = \frac{\Delta \rho g h}{\rho V^2} \quad (2.64)$$

where h is the layer depth. This parameter was also estimated for the outflows using the observed layer thickness and other flow properties at the source profile. These results indicate that the rather stable conditions ($Ri_o > 1$) existing in both currents are responsible for the small values derived for the entrainment coefficients. According to experimental evidence compiled by Turner (1973), the value of e_o drops from 10^{-2} near $Ri_o = 1$ to less than 10^{-4} at $Ri_o = 10$. The magnitudes quoted for the outflow currents in Table III not only lie in this range but also show the proper trend. It must be emphasized, however, that these values are order-of-magnitude estimates only, due to uncertainties in the observed outflow data and a detailed quantitative comparison is therefore unwarranted.

Quantity	$\Delta\rho$ (gm/cm ³)	V (cm/sec)	h (m)	ℓ (km)	Ri_o	$e_o = E_o/\ell$	$k = K/\ell$
Current							
Norwegian Overflow	$.38 \times 10^{-3}$	16.0	100	100	14.5	6.5×10^{-4}	.15
Mediterranean Outflow	1.25×10^{-3}	100	200	50	2.45	1.00×10^{-3}	.01

TABLE III. Average Dimensionless Friction and Entrainment Coefficients

Finally, the disparity between the values of E_0 and K may be used to make certain inferences about the structure of turbulence in the outflow currents. First of all, it is important to note that the magnitudes of E_0 and K are both linked to the strength of the interfacial stresses, τ_I . This quantity appears explicitly in the definition of K [equation (2.4)] and, assuming horizontal homogeneity, it may be directly related to E_0 by a simple momentum balance at the interface,

$$\tau_I = \rho E_0 V^2 / l \quad (2.65)$$

where l is the cross-stream scale. Therefore, the fact that the optimum value of K exceeds that of E_0 by at least an order of magnitude in both comparisons with outflow data signifies that turbulent stresses at the bottom of the layer, τ_B , provide most of the frictional resistance to the current ($\tau_B \gg \tau_I$) while the interfacial turbulence which gives rise to entrainment is much weaker on an overall basis. Furthermore, the turbulence at the interface is believed to consist of locally generated disturbances (e.g., by hydrodynamic instability) rather than residual turbulence which is generated at the bottom and decays in intensity as it penetrates the layer. This hypothesis is supported by the character of the downstream density profiles for the Norwegian Overflow (Figure 2-4) which show broad zones of nearly linear stratification above the relatively homogeneous interior portions of the flow. A similar feature was observed by Ellison and Turner (1959) in their laboratory study of turbulent flows down inclines and was interpreted using dimensional arguments as characteristic of a "self-regulated" flow which

is influenced by turbulence generated elsewhere in the layer. In such a case, the flow field near the interface is maintained in a marginally stable state, the turbulence is therefore strongly damped and the entrainment is weak [see Turner (1973), p. 186]. In contrast, if turbulence generated at the bottom were the primary cause of entrainment at the interface, then the density gradient in the downstream profiles would be sharp, as it is near the source, and the entire layer would be well-mixed. This conclusion is reached by analogy to the results of the "stirring experiments" quoted by Turner (1973) in which mechanically generated turbulence was used to mix across a remote density interface.

Based on the suggestion that turbulent bottom stresses play a dominant role in the source region dynamics of outflow currents, a more elaborate viscous model will be presented in the next chapter. The purpose of this model is to isolate frictional effects and propose a detailed mechanism by which they lead to the observed features of these flows.

CHAPTER III

Formulation of Ekman-Layer Model

The dynamical nature of the turbulent boundary layer which exists beneath the outflow currents and transmits their momentum to the ocean floor is not well understood. Most analytical attempts to investigate boundary layer flow in a turbulent, rotating fluid fall into two broad classes. Neither approach takes account of time dependence and both assume the boundary layer is Ekman-like in the sense that the flow above the bottom is geostrophic and that the associated Coriolis forces remain dynamically significant in balancing the divergence of the turbulent stress field near the bottom. In the first class of analyses, certain structural features of the turbulent Ekman layer are deduced using similarity hypotheses and dimensional arguments. By these accounts [see Monin (1970)], the boundary layer is divided into two regions, a logarithmic layer, characterized by constant stress, overlain by a thicker Ekman layer. The similarity arguments are used to provide relations among various properties of the flow such as the stress at the boundary and the total veering angle between the geostrophic velocity and bottom stress vectors [e.g. Csanady (1967)]. The empirical constants arising in these expressions are usually determined by appealing to observational data and/or the results of numerical studies. A field experiment designed to test the predictions of these Ekman layer theories against measurements taken at the base of the Florida Current was carried out by Weatherly (1972). Among other things, he finds that although

a mean veering in the correct sense does exist between the geostrophic velocity and bottom stress vectors, it takes place entirely within the logarithmic layer. The failure to observe the characteristic Ekman layer features above the logarithmic layer is attributed to the presence of a strong diurnal tide component, which modulates the flow faster than the layer structure can form. Weatherly's results cast doubt on all attempts to apply quasi-stationary Ekman layer theory to ocean-bottom boundary layers. However, the observation of mean veering coupled with diminishing velocity near the bottom supports the contention that at least some of the aspects of a rotating boundary layer are preserved in spite of the strong temporal variability. Moreover, characteristic Ekman features have been observed in other oceanographic contexts. For instance, some (unpublished) current profile measurements taken by J. Meincke of The Institut für Meereskunde, Kiel, Germany, during a cruise of the R.V. "Anton Dohrn" in May and June, 1972, show a rapid turning of the velocity vector in the proper sense within the deepest 30 meters of the Norwegian Sea overflow water on the Iceland-Faroe Ridge. Thus conflicting evidence indicates that Weatherly's single measurement may not be typical of bottom boundary layers, especially those beneath the outflow currents where surface tides are weak.

The second category of Ekman layer analyses includes eddy viscosity models and mixing length theories. The basis for these investigations is an analogy drawn between turbulent and molecular processes. Specifically, in the eddy viscosity models, a turbulent viscosity coefficient, ν_t , is used to relate stress vector to the shear of the mean velocity profile. In contrast to the constant molecular coefficient, the eddy viscosity is known

to be a function of space and time scales. It also varies with distance from the boundary so that the structure of the turbulent layer is not exactly the same as the laminar Ekman spiral. Moreover, because of the dependence on scale, the variation of ν_t across the layer is not universal, but depends to some degree on the particular application. Using the results of their laboratory study of the turbulent Ekman layer, Caldwell, Van Atta, and Helland (1972) attempted to correlate observations of the planetary boundary layer with measurements taken in the controlled laboratory environment using two variable eddy viscosity models. They conclude that these models can predict the aspects of the turbulent boundary layer with varying degrees of success, but that the overall agreement is not entirely satisfactory.

For the present model, the turbulent Ekman layer presumed to exist at the base of the outflow currents will be parameterized by a constant eddy viscosity. In view of the lack of unanimity about the proper mathematical description of such a layer, the use of a more sophisticated model, which incorporates variable coefficients or similarity hypotheses, is hardly warranted. Moreover, in the absence of detailed velocity profile measurements in the outflow currents, there would be no basis by which the merits of an elaborate model could be evaluated. Finally, the analogy of a constant eddy viscosity with molecular friction allows direct comparison of theoretical results with laboratory experiments carried out in the laminar regime. It is hoped that this simplified analysis will furnish an approximate picture of the influence of turbulent frictional processes at the ocean floor and provide results which will serve as a basis for further investigation.

Before proceeding with the mathematical formulation some representative values of the turbulent eddy viscosity are needed. Since the streamtube model results contain no information about the shear of the mean velocity profile, it is difficult to obtain meaningful estimates of K from the frictional constants K derived from the outflow data. However, an alternate approach may be used. According to Faller (1971), the vertically averaged eddy viscosity near the ocean floor varies approximately as the square of the geostrophic velocity, V_g , such that the Reynolds number based on the scale height of the turbulent boundary layer $R_t = V_g \left(\frac{2}{\nu_{tf}} \right)^{1/2}$ remains constant at a value of 10^3 . He bases this conclusion on the results of measurements in the atmospheric boundary layer which he claims should apply to the oceanic bottom boundary layer for geostrophic velocities in excess of 10 cm/sec. Applying his formula to the source conditions of the Norwegian and Mediterranean outflows gives eddy viscosities of $\nu_{t_N} = 4.0 \text{ cm}^2/\text{sec}$ and $\nu_{t_M} = 215 \text{ cm}^2/\text{sec}$ respectively. The corresponding values of the Ekman layer scale height, $A = \left(\frac{2\nu_t}{f} \right)^{1/2}$, are $A_N = 2.46 \text{ m}$ and $A_M = 22.5 \text{ m}$. The degree of uncertainty about the magnitude of the turbulent friction coefficient is clearly evident from the large difference in these estimates.

In addition to the adoption of a constant eddy viscosity to characterize the turbulent stress field, the flow field is assumed to be stationary, the density stratification is approximated by two homogeneous layers, and the Coriolis parameter is assumed not to vary significantly over the region of interest. The upper fluid is in hydrostatic balance and based on the

weakness of turbulence at the fluid boundary inferred from the streamtube results (Chapter II), the interface is taken to be stress-free. With these restrictions, the vector equations of motion for the turbulent Ekman-layer model are:

$$\nabla \cdot \underline{u} = 0, \quad (3.1)$$

$$\underline{u} \cdot \nabla \underline{u} + \underline{f} \times \underline{u} = - \frac{1}{\rho} \nabla P + \underline{g} + \nu_t \nabla^2 \underline{u}, \quad (3.2)$$

where \underline{f} is twice the normal component of the Earth's rotation and ρ is the density of the lower layer. As in most geophysical applications, the centrifugal term in the momentum equation has been included in the gravitational acceleration, \underline{g} . However, in analyzing the rotating fluid dynamic experiments described in the following chapters, it will be important to distinguish these two terms.

The coordinate system employed in this analysis is the bottom-oriented Cartesian set used in the streamtube model and shown again in Figure 3-1. The inclination of the plane bottom is measured by α , and the x-, y- and z-axes lie along, down, and normal to the slope, respectively. The position of the free surface is defined by $z = d(x,y)$ and, for the general case, the lateral edges of the flow are at $y = y_e^-(x), y_e^+(x)$. The component forms of the governing equations in this system are given by

$$u_x + v_y + w_z = 0 \quad (3.3)$$

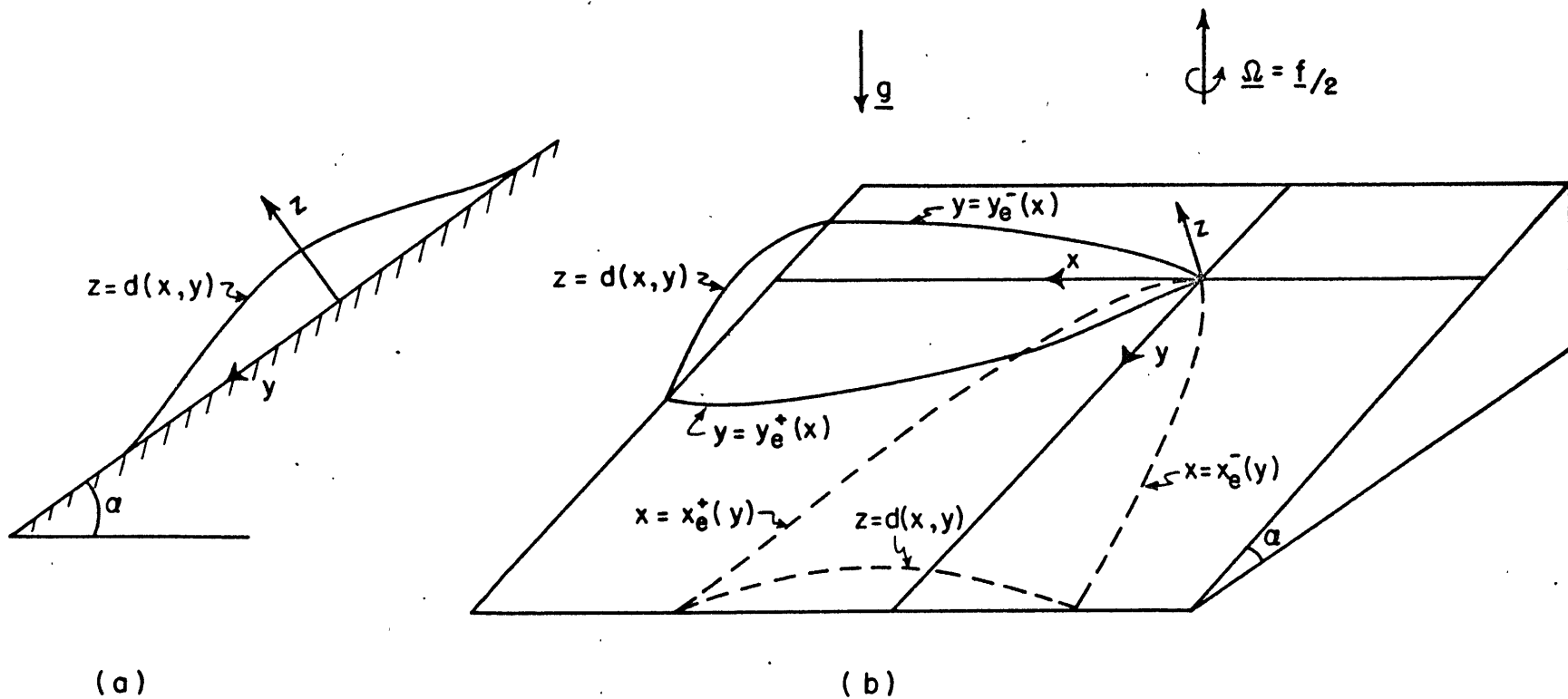


Figure 3-1. Schematic diagram of the geometry for the Ekman layer model.
 (a) side view, (b) front view.

$$\underline{u} \cdot \nabla u - \hat{f}(v + sw) = -\frac{1}{\rho} P_x + \nu_t \nabla^2 u, \quad (3.4)$$

$$\underline{u} \cdot \nabla v + \hat{f}u = -\frac{1}{\rho} P_y + \hat{g}s + \nu_t \nabla^2 v, \quad (3.5)$$

$$\underline{u} \cdot \nabla w + \hat{f}s = -\frac{1}{\rho} P_z - \hat{g} + \nu_t \nabla^2 w, \quad (3.6)$$

where
$$\underline{u} \cdot \nabla = u \frac{\partial}{\partial x} + v \frac{\partial}{\partial y} + w \frac{\partial}{\partial z}, \quad (3.7)$$

and
$$\nabla^2 = \frac{\partial^2}{\partial x^2} + \frac{\partial^2}{\partial y^2} + \frac{\partial^2}{\partial z^2}. \quad (3.8)$$

The parameters appearing in the equations are the bottom slope $s = \tan \alpha$, the Coriolis and gravitational constants $\hat{f} = 2|\underline{\Omega}| \cos \alpha$ and $\hat{g} = |g| \cos \alpha$, and the turbulent eddy viscosity ν_t .

The constraints applied at the boundaries of the flow are listed below.

(i) The "no slip" condition at the solid surface is

$$u = v = w, \quad \text{at } z = 0. \quad (3.9)$$

(ii) The zero stress, kinematic, and hydrostatic pressure conditions at the free surface are

$$u_z = -w_x + (v_x + u_y) dy + 2u_x dx, \quad (3.10)$$

$$v_z = -w_y + 2v_y dy + (v_x + u_y) dx, \quad (3.11)$$

$$w = u dx + v dy, \quad (3.12)$$

and

$$P = \rho_0 g H_0 + \rho_0 \hat{g} (s y - d) \quad \text{at } z = d(x, y) \quad (3.13)$$

where the curvature of the free surface has been assumed small and

ρ_0 and H_0 are the uniform density and depth at the origin
($x = y = 0$) for the upper layer.

(iii) The edge condition is simply

$$d = 0 \quad \text{at } y = y_e^-(x), y_e^+(x) \quad (3.14)$$

An auxiliary condition serves to specify the total downstream volumetric flow which is constant in the absence of entrainment,

$$Q = \int_{y_e^-}^{y_e^+} dy \int_0^d u dz \quad (3.15)$$

It is convenient at this point to introduce an alternate representation for the edge and flux conditions, (3.14) and (3.15), which will be used in the next chapter for the analysis of viscous dominated flows. In this case, the velocity is directed primarily in the downslope direction so the edges of the flow are defined more conveniently by $x = x_e^-(y), x_e^+(y)$ as indicated by the dashed curves in Figure 3-1(b). The corresponding mathematical constraints are,

$$d = 0 \quad \text{at } x = x_e^-(y), x_e^+(y) \quad (3.16)$$

and

$$Q = \int_{x_e^-}^{x_e^+} dx \int_0^d v dz \quad (3.17)$$

Using scales derived from the source flow parameters, the variables are made dimensionless in the following manner

$$(x, y, z) = L_1 (\hat{x}, \hat{y}, s\hat{z}),$$

$$(u, v, w) = U (\hat{u}, \hat{v}, s\hat{w}), \quad (3.18)$$

and

$$P = \rho_0 g H_0 + \rho \hat{g} (s y - z) + \rho \hat{g}_r s L_1 \hat{p}(\hat{x}, \hat{y}, \hat{z})$$

where $\hat{g}_r = \frac{\rho - \rho_0}{\rho} \hat{g}$ is the reduced gravity parameter, (3.19)

$$U = \frac{\hat{g}_r s}{\hat{f}}$$
 is the geostrophic velocity scale, (3.20)

and $L_1 = \left(\frac{\hat{f} Q}{s^2 \hat{g}_r} \right)^{1/2}$ is the source flow length scale. (3.21)

These definitions will be referred to as the "source flow" scaling since, in the resulting dimensionless system, the source strength is normalized to one. In terms of these variables, the equations of motion take the following form:

$$\hat{u}_{\hat{x}} + \hat{v}_{\hat{y}} + \hat{w}_{\hat{z}} = 0 \quad (3.22)$$

$$\epsilon \hat{u} \cdot \nabla \hat{u} - (\hat{v} + s^2 \hat{w}) = -\hat{p}_{\hat{x}} + E \left[\hat{u}_{\hat{z}\hat{z}} + s^2 (\hat{u}_{\hat{x}\hat{x}} + \hat{u}_{\hat{y}\hat{y}}) \right], \quad (3.23)$$

$$\epsilon \hat{u} \cdot \nabla \hat{v} + \hat{u} = -\hat{p}_{\hat{y}} + E \left[\hat{v}_{\hat{z}\hat{z}} + s^2 (\hat{v}_{\hat{x}\hat{x}} + \hat{v}_{\hat{y}\hat{y}}) \right], \quad (3.24)$$

$$\epsilon \hat{u} \cdot \nabla \hat{w} + s^2 \hat{u} = -\hat{p}_{\hat{z}} + s^2 E \left[\hat{w}_{\hat{z}\hat{z}} + s^2 (\hat{w}_{\hat{x}\hat{x}} + \hat{w}_{\hat{y}\hat{y}}) \right], \quad (3.25)$$

where

$$C = \left(\frac{\hat{q}_r^3 s^4}{\hat{f}^5 Q} \right)^{1/2} \quad \text{is the source flow Rossby number, (3.26)}$$

and

$$E = \frac{v_t \hat{q}_r}{\hat{f}^2 Q} \quad \text{is the turbulent Ekman number. (3.27)}$$

The boundary conditions corresponding to (3.9) through (3.14) are given by:

$$(i) \quad \hat{u} = \hat{v} = \hat{w} = 0 \quad \text{at} \quad \hat{z} = 0 \quad (3.29)$$

$$(ii) \quad \hat{u}_{\hat{z}} = s^2 \left[-\hat{w}_{\hat{x}} + (\hat{v}_{\hat{x}} + \hat{u}_{\hat{y}}) \hat{d}_{\hat{y}} + 2 \hat{u}_{\hat{x}} \hat{d}_{\hat{x}} \right], \quad (3.30)$$

$$\hat{v}_{\hat{z}} = s^2 \left[-\hat{w}_{\hat{y}} + 2 \hat{v}_{\hat{y}} \hat{d}_{\hat{y}} + (\hat{v}_{\hat{x}} + \hat{u}_{\hat{y}}) \hat{d}_{\hat{x}} \right], \quad (3.31)$$

$$\hat{w} = \hat{u} \hat{d}_{\hat{x}} + \hat{v} \hat{d}_{\hat{y}}, \quad (3.32)$$

$$\text{and} \quad \hat{p} = -(\hat{\gamma} - \hat{d}) \quad \text{at} \quad \hat{z} = \hat{d}(\hat{x}, \hat{y}), \quad \text{and} \quad (3.33)$$

$$(iii) \quad \hat{d} = 0 \quad \text{at} \quad \hat{y} = \hat{y}_e^-(\hat{x}), \hat{y}_e^+(\hat{x}). \quad (3.34)$$

Similarly, the volumetric flow rate is defined by,

$$1 = \int_{\hat{y}_e^-}^{\hat{y}_e^+} \hat{d}_{\hat{y}} \int_0^{\hat{d}} \hat{u} \, \hat{d}_{\hat{z}} \, \hat{d}_{\hat{x}}. \quad (3.35)$$

Estimates of typical Rossby numbers for the outflow currents may be derived from the flow properties at the initial profiles and the average physical constants (Tables I and II). These results indicate that convective

accelerations are small in the Norwegian Overflow ($\epsilon_N = .035$), but because of weaker rotation and stronger density contrast, this assumption is questionable for the Mediterranean Outflow ($\epsilon_M = 2.84$). Similarly, the Ekman numbers for typical outflow conditions may be estimated using turbulent eddy viscosities derived from Faller's criterion. The values obtained by this method are small in both cases ($E_N = .66 \times 10^{-4}$; $E_M = 1.72 \times 10^{-2}$). Since E measures the square ratio of the Ekman Layer length scale $(2\nu_t/\hat{f})^{1/2}$ to a vertical dimension based on the source flow length scale $sL_1 = (\hat{f}Q/\hat{q}_r)^{1/2}$, these magnitudes indicate that turbulent Ekman layer occupies only a small fraction of the outflow profile.

Attention will now be focused on viscous effects by assuming that the bottom slope is gradual,

$$s^2 \ll 1 \quad (3.36)$$

and by linearizing the momentum equations on the condition that the Rossby number is small, i.e.,

$$\epsilon \ll 1 \quad (3.37)$$

According to the scaling, the slope s is a measure of variations in layer thickness in directions parallel to the bottom. In fact, for geostrophic currents on which the scaling is based, the criterion for unidirectional flow in the layer is that the cross-stream gradient in thickness not exceed the slope at any point, i.e.,

$$d_y \leq s.$$

Therefore, the requirement that the bottom slope be slight implies that the aspect ratio of cross-stream profile is small also. Both these conditions are well satisfied by most of the outflow sections presented in the previous chapter. (See Figures 2-3 and 2-10.)

With these restrictions, the reduced pressure field is hydrostatic,

$$\hat{p} = -(\hat{y} - \hat{d}) \quad (3.38)$$

and the governing equations reduce to

$$\hat{u}_{\hat{x}} + \hat{v}_{\hat{y}} + \hat{w}_{\hat{z}} = 0, \quad (3.39)$$

$$-\hat{v} = -\hat{d}_{\hat{x}} + E \hat{u}_{\hat{z}\hat{z}}, \quad (3.40)$$

$$\hat{u} = 1 - \hat{d}_{\hat{y}} + E \hat{v}_{\hat{z}\hat{z}}, \quad (3.41)$$

with boundary conditions,

$$(i) \quad \hat{u} = \hat{v} = \hat{w} = 0 \quad \text{at} \quad \hat{z} = 0 \quad (3.42)$$

$$(ii) \quad \hat{u}_{\hat{z}} = \hat{v}_{\hat{z}} = 0 \quad \text{at} \quad \hat{z} = \hat{d}(\hat{x}, \hat{y}) \quad (3.43)$$

$$\hat{w} = \hat{u} \hat{d}_{\hat{x}} + \hat{v} \hat{d}_{\hat{y}} \quad (3.44)$$

$$(iii) \quad \hat{d} = 0 \quad \text{at} \quad \hat{y} = \hat{y}_e^-(\hat{x}), \hat{y}_e^+(\hat{x}). \quad (3.45)$$

The form of the flux condition, (3.35), is unchanged.

Apart from the desire to isolate frictional influence, there is strong mathematical justification for retaining the small viscous terms in this system. Since E multiplies the highest order derivatives in the momentum equations, the perturbing effects of small viscosity are singular in the sense that the boundary layers required to match boundary conditions which are not satisfied by the frictionless (geostrophic) flow change the character of that solution completely.

To facilitate the following derivation, the parameter E will be absorbed by redefining the vertical scale height in terms of the Ekman thickness, i.e.,

$$sL \rightarrow (2E)^{1/2} sL = \left(\frac{2\nu_t}{f} \right)^{1/2} = A. \quad (3.46)$$

The resulting normalization will be referred to as the "Ekman scaling" and is defined explicitly by the following relations,

$$(x, y, z) = \frac{A}{s} (\bar{x}, \bar{y}, s\bar{z}), \quad (3.47)$$

$$(u, v, w) = U (\bar{u}, \bar{v}, s\bar{w}),$$

and
$$P = \rho_0 g H_0 + \rho \hat{q} (s\gamma - z) + \rho \hat{q}_r A \bar{p}(\bar{x}, \bar{y}, \bar{z}),$$

where the velocity scale and hydrostatic pressure components are unchanged from the source flow scaling (3.18). Under this system, no parameters appear in the equations of motion,

$$\bar{u}_{\bar{x}} + \bar{v}_{\bar{y}} + \bar{w}_{\bar{z}} = 0, \quad (3.48)$$

$$-\bar{v} = -\bar{d}_{\bar{x}} + \frac{1}{2} \bar{u}_{\bar{z}\bar{z}}, \quad (3.49)$$

$$\bar{u} = 1 - \bar{d}_{\bar{y}} + \frac{1}{2} \bar{v}_{\bar{z}\bar{z}}, \quad (3.50)$$

or the boundary conditions,

$$(i) \quad \bar{u} = \bar{v} = \bar{w} = 0 \quad \text{at} \quad \bar{z} = 0 \quad (3.51)$$

$$(ii) \quad \bar{u}_{\bar{z}} = \bar{v}_{\bar{z}} = 0 \quad (3.52)$$

$$\bar{w} = \bar{u} \bar{d}_{\bar{x}} + \bar{v} \bar{d}_{\bar{y}} \quad \text{at} \quad \bar{z} = \bar{d}(\bar{x}, \bar{y}) \quad (3.53)$$

$$(iii) \quad \bar{d} = 0 \quad \text{at} \quad \bar{y} = \bar{y}_e^-(\bar{x}), \bar{y}_e^+(\bar{x}). \quad (3.54)$$

Instead, the Ekman number appears in the modified definition of the dimensionless source strength,

$$\int_{\bar{y}_e^-}^{\bar{y}_e^+} d\bar{y} \int_0^{\bar{d}} \bar{u} d\bar{z} = (2E)^{-1}. \quad (3.55)$$

It is worth noting that the appropriate Rossby number under the Ekman scaling is,

$$\bar{E} = \frac{\hat{q}_r S^2}{\hat{f}^2} \left(\frac{\hat{f}}{2\nu_t} \right)^{1/2} = (2E)^{-1/2} \epsilon, \quad (3.56)$$

which measures the magnitude of the convective accelerations in the Ekman layer.

A single equation governing the distribution of layer thickness, $\bar{d}(\bar{x}, \bar{y})$, may now be derived by a generalized Ekman layer analysis. The procedure is based on the computation of the divergence of the local layer fluxes. Using Leibnitz' rule and the kinematic condition in (3.53), integration of the continuity equation from the solid surface ($\bar{z}=0$) to the interface ($\bar{z}=\bar{d}$) lead to the condition for zero divergence of the integrated horizontal velocity components, i.e.,

$$\bar{U}_{\bar{x}} + \bar{V}_{\bar{y}} = 0, \quad (3.57)$$

where
$$\bar{U} = \int_0^{\bar{d}} \bar{u} d\bar{z}, \quad (3.58)$$

and
$$\bar{V} = \int_0^{\bar{d}} \bar{v} d\bar{z}. \quad (3.59)$$

Next the momentum equations are written in the form

$$\bar{u}_{\bar{z}\bar{z}} + 2\bar{v} = -2G,$$

$$\bar{v}_{\bar{z}\bar{z}} - 2\bar{u} = 2F,$$

where $G = -\bar{d}_{\bar{x}}$ and $F = \bar{d}_{\bar{y}}$. These expressions may be combined to give a single equation governing the complex velocity function

$$\tilde{V} = \bar{u} + i\bar{v} \quad (i = \sqrt{-1}),$$

$$\tilde{V}_{\bar{z}\bar{z}} - 2i\tilde{V} = -2(G - iF).$$

The general solution to this equation is expressed in terms of complex exponentials,

$$\tilde{V} = A e^{(1+i)\bar{z}} + B e^{-(1+i)\bar{z}} - (F+iG).$$

The complex constants, A and B, are determined by the appropriate boundary conditions at the bottom and free surface, i.e.,

$$(i) \quad \tilde{V} = 0 \quad \text{at} \quad \bar{z} = 0$$

$$(ii) \quad \tilde{V}_{\bar{z}} = 0 \quad \text{at} \quad \bar{z} = \bar{d}(\bar{x}, \bar{y}).$$

After expressing each constant as the sum of a real and imaginary part, the resulting horizontal velocity components are

$$\bar{u} = -F + (A_r \cos \bar{z} - A_i \sin \bar{z}) e^{\bar{z}} + (B_r \cos \bar{z} + B_i \sin \bar{z}) e^{-\bar{z}} \quad (3.60)$$

$$\bar{v} = -G + (A_r \sin \bar{z} + A_i \cos \bar{z}) e^{\bar{z}} + (B_i \cos \bar{z} - B_r \sin \bar{z}) e^{-\bar{z}} \quad (3.61)$$

where

$$A_r = \frac{1}{2D} [F(\cos 2\bar{d} + e^{-2\bar{d}}) + G \sin 2\bar{d}],$$

$$A_i = \frac{1}{2D} [F \sin 2\bar{d} - G(\cos 2\bar{d} + e^{-2\bar{d}})],$$

$$B_r = \frac{1}{2D} [F(\cos 2\bar{d} + e^{2\bar{d}}) - G \sin 2\bar{d}],$$

$$B_i = \frac{1}{2D} [F \sin 2\bar{d} + G(\cos 2\bar{d} + e^{2\bar{d}})],$$

for $F = \bar{d}_y - 1$, $G = -\bar{d}_x$

and $D = \cosh 2\bar{d} + \cos 2\bar{d}$.

The layer fluxes may now be computed by direct integration over the layer depth to give,

$$\bar{U} = (1 - \bar{d}_y) \bar{d} - \frac{\bar{d}_x}{2} \left(\frac{\sinh 2\bar{d} - \sin 2\bar{d}}{\cosh 2\bar{d} + \cos 2\bar{d}} \right) - \frac{1 - \bar{d}_y}{2} \left(\frac{\sinh 2\bar{d} + \sin 2\bar{d}}{\cosh 2\bar{d} + \cos 2\bar{d}} \right) \quad (3.62)$$

and

$$\bar{V} = \bar{d}_x \bar{d} - \frac{\bar{d}_x}{2} \left(\frac{\sinh 2\bar{d} + \sin 2\bar{d}}{\cosh 2\bar{d} + \cos 2\bar{d}} \right) + \frac{1 - \bar{d}_y}{2} \left(\frac{\sinh 2\bar{d} - \sin 2\bar{d}}{\cosh 2\bar{d} + \cos 2\bar{d}} \right) \quad (3.63)$$

After extensive algebraic manipulation, the divergence of these quantities was calculated and reduced to a single, nonlinear second-order partial differential equation governing the layer thickness function

$$\begin{aligned} & (\sinh 2\bar{d} - \sin 2\bar{d})(\cosh 2\bar{d} + \cos 2\bar{d}) (\bar{d}_x \bar{x} + \bar{d}_y \bar{y}) + 4 \sinh 2\bar{d} \sin 2\bar{d} (\bar{d}_x^2 + \bar{d}_y^2) \\ & = 4 \sinh 2\bar{d} \sin 2\bar{d} \bar{d}_y + 2 (\sinh^2 2\bar{d} - \sin^2 2\bar{d}) \bar{d}_x . \end{aligned} \quad (3.64)$$

Due to the complicated dependence of its coefficients on \bar{d} , this most general form of the thickness equation was judged intractable by analytic methods. Moreover, because the equation is elliptic, its numerical solution would require specification of the layer thickness profile at two cross-stream sections bounding the region of interest, in

addition to the conditions at the lateral edges of the flow (3.54). To carry out such computations, based on a series of arbitrary source and downstream thickness profiles, would contribute little toward understanding the nature of the interaction between viscous and rotational forces. Instead asymptotic methods will be employed to obtain analytical solutions to the two important limiting forms of equation (3.64), namely for 1) flows controlled by viscous forces, and 2) flows dominated by rotation. By isolating each effect in this manner, it is possible to evaluate the role it plays in the overall dynamical balance of this model and thereby gauge its importance in the oceanic case.

The mathematical definition of the viscous and rotational limits is expressed in terms of the magnitude of the normalized layer thickness variable, $\bar{d}(\bar{x}, \bar{y})$. For regions where $\bar{d} \ll 1$, the layer thickness is much smaller than the Ekman scale $(2\nu_t/\bar{f})^{1/2}$ and the flow is dominated by viscous forces. In this limit, the coefficients in equation (3.64) may be expressed to any desired accuracy by expanding the trigonometric and hyperbolic functions about $\bar{d} = 0$. If only the lowest order term in each coefficient is retained, the thickness equation takes the form

$$\bar{d}(\bar{d}_{\bar{x}\bar{x}} + \bar{d}_{\bar{y}\bar{y}}) + 3(\bar{d}_{\bar{x}}^2 + \bar{d}_{\bar{y}}^2) = 3\bar{d}_{\bar{y}} + 4\bar{d}^2\bar{d}_{\bar{x}} + O(\bar{d}^6), \quad (3.65)$$

for $\bar{d} \ll 1$.

To derive the corresponding velocity components in this limit, it is convenient to streamline the somewhat cumbersome expressions for the general case, (3.60) and (3.61). Making use of the relations among the

trigonometric and hyperbolic functions, the following simplified forms are obtained,

$$\bar{u} = (1-M)(1-\bar{d}\bar{y}) - N \bar{d}\bar{x} , \quad (3.66)$$

$$\bar{v} = (1-M) \bar{d}\bar{x} + N(1-\bar{d}\bar{y}) , \quad (3.67)$$

where

$$M = \mathcal{D}^{-1} [\cosh(2\bar{d}-\bar{z}) \cos \bar{z} + \cos(2\bar{d}-\bar{z}) \cosh \bar{z}]$$

$$N = \mathcal{D}^{-1} [\sinh(2\bar{d}-\bar{z}) \sin \bar{z} + \sin(2\bar{d}-\bar{z}) \sinh \bar{z}]$$

$$\mathcal{D} = \cosh 2\bar{d} + \cos 2\bar{d} .$$

Expansion of the terms in these expressions for $\bar{z} \ll \bar{d}$ yields the relations for the horizontal velocity components,

$$\bar{u} = -\bar{d}\bar{x} \bar{z} (2\bar{d}-\bar{z}) + \mathcal{O}(\bar{d}^6) , \quad (3.68)$$

$$\bar{v} = (1-\bar{d}\bar{y}) \bar{z} (2\bar{d}-\bar{z}) + \mathcal{O}(\bar{d}^6) . \quad (3.69)$$

The corresponding forms for the integrated layer fluxes are,

$$\bar{U} = -\frac{2}{3} \bar{d}^3 \bar{d}\bar{x} + \mathcal{O}(\bar{d}^7) , \quad (3.70)$$

and

$$\bar{V} = \frac{2}{3} \bar{d}^3 (1-\bar{d}\bar{y}) + \mathcal{O}(\bar{d}^7) ,$$

$$\text{for } \bar{d} \ll 1 . \quad (3.71)$$

With $\bar{d}(\bar{x}, \bar{y})$ defined by the layer thickness equation (3.65) and the appropriate boundary conditions, the horizontal velocity profiles in the viscous-dominated flow are parabolic, while the local layer fluxes are proportional to \bar{d}^3 . These are familiar results for two-dimensional viscous flows down inclines [see Batchelor (1967) p. 183]. Equations (3.65) and (3.68) to (3.71) provide a basis for the investigation of the weak rotation limit pursued in Chapter IV.

In contrast to the thin layer viscous limit, if the local layer thickness far exceeds the Ekman length scale ($\bar{d} \gg 1$), then rotational effects are dominant. In this situation, the hyperbolic functions of \bar{d} reduce to exponentials and the layer thickness equation becomes a simple diffusion equation,

$$\bar{d}_{\bar{x}\bar{x}} + \bar{d}_{\bar{y}\bar{y}} = 2\bar{d}_{\bar{x}} + \mathcal{O}(e^{-2\bar{d}}) \quad \text{for } \bar{d} \gg 1. \quad (3.72)$$

The horizontal velocity field is mainly geostrophic with a thin Ekman layer adjacent to the boundary,

$$\bar{u} = (1 - \bar{d}_{\bar{y}}) - [(1 - \bar{d}_{\bar{y}}) \cos \bar{z} + \bar{d}_{\bar{x}} \sin \bar{z}] e^{-\bar{z}} + \mathcal{O}(e^{-2\bar{d}}) \quad (3.73)$$

and

$$\bar{v} = \bar{d}_{\bar{x}} - [\bar{d}_{\bar{x}} \cos \bar{z} - (1 - \bar{d}_{\bar{y}}) \sin \bar{z}] e^{-\bar{z}} + \mathcal{O}(e^{-2\bar{d}}), \quad (3.74)$$

for $\bar{d} \gg 1$,

and the corresponding layer fluxes are given by

$$\bar{U} = \bar{d}(1 - \bar{d}\bar{y}) - \frac{1}{2}(1 - \bar{d}\bar{y} + \bar{d}\bar{x}) + \mathcal{O}(e^{-2\bar{d}}) \quad (3.75)$$

and
$$\bar{V} = \bar{d}\bar{d}\bar{x} + \frac{1}{2}(1 - \bar{d}\bar{y} - \bar{d}\bar{x}) + \mathcal{O}(e^{-2\bar{d}}) \quad \text{for } \bar{d} \gg 1. \quad (3.76)$$

These equations describe the flow in a thick geostrophic layer whose development is controlled by a viscous Ekman layer at its base. The singular nature of the inviscid limit is clear from these expressions, since, in the absence of friction, the Ekman layer structure would disappear from the horizontal velocity field and the diffusion term in the thickness equation would also vanish, leading to a non-shearing layer with an invariant thickness profile. These and other peculiar aspects of the strong rotation limit will be explored in Chapter V.

CHAPTER IV

Weak Rotation in the Ekman Layer Model

The foundation for the investigation of the weak-rotation limit of the Ekman layer model is a study of flow in the non-rotating case. A similarity solution for the asymptotic behavior of a steady, viscous source flow on an inclined plane has already been derived and demonstrated in the laboratory by Smith (1973) [hereafter referred to as S1]. In this situation, the primary dynamic balance is between the downslope component of gravity and retarding viscous forces. Lateral spreading of the flow is caused by the pressure gradient induced by the cross-stream variation in layer thickness. Furthermore, the decaying influence of the source conditions in the downstream region leads to a self-similar flow whose properties vary according to certain power laws of the downstream coordinate. A simple laboratory experiment confirms the following major features of the similarity solution (using present notation): i) a parabolic cross-stream variation in layer thickness; ii) spreading of the flow according to a $y^{3/7}$ power law; iii) thinning of the layer along streamlines like $y^{-1/7}$; and iv) surface velocities which vary as the square of the layer thickness.

The purpose of the present study is to extend the analysis of the purely viscous case to include weak rotational effects. Within the framework of a perturbation theory, corrections to the layer thickness profile and horizontal velocity field will be derived in terms of the similarity variables. However, the validity of the perturbation scheme

is limited to a finite downstream region beyond which the corrections to the viscous solution can no longer be considered small. Physically, the cumulative effects of the Coriolis force operating on the strong downslope component of velocity results in a significant shift of the current axis away from the centerline of the viscous flow. Thus, the asymptotic state associated with the viscous case is ultimately destroyed by any small amount of rotation. However, for sufficiently strong friction, the flow is expected to diverge very gradually from the basic solution and the conditions under which the weak rotation analysis is valid would therefore apply over a significant portion of the downstream flow field.

The derivation of the theoretical corrections to the viscous flow will be presented in the next section followed by a description of a laboratory experiment designed to test the important aspects of the extended similarity solution. A comparison of the theoretical and experimental results will be discussed in the final section.

IV.1 A Similarity Solution Including Weak Rotational Effects

The formulation of the source flow problem including weak rotational influence follows the lines established for the viscous case. The Cartesian coordinate system described in Chapter III is illustrated in Figure 3-1. The appropriate fluid boundaries, $z = d(x, y)$ and $x = x_e^-(y)$, $x_e^+(y)$, are indicated by the dashed curve in Figure 3-1(b).

In the downstream region, the natural length scale associated with the source dimensions has been eliminated. It is standard practice in such cases to form a reference length from the external parameters of the problem \hat{q}_r , ν_t , Q , s and \hat{f} . Two examples of this formal technique for normalizing variables are provided by the source flow (3.18) and Ekman layer (3.47) scalings presented in the previous chapter. However, because of the strong rotational influence implicit in these laws, they will be rejected in favor of an asymptotic scaling based on a characteristic downstream distance, Y . This procedure leads directly to the appropriate downstream balance for large Y and also serves to exhibit the dependence of small rotational terms on downstream distance through the form of the dimensionless rotation parameter. Under the asymptotic scaling, the variables are normalized as follows:

$$(x, y, z) = Y (\delta \tilde{x}, \tilde{y}, \beta \tilde{z}), \quad (4.1)$$

$$(u, v, w) = \mathcal{U} (\delta \tilde{u}, \tilde{v}, \beta \tilde{w}),$$

$$P = \rho_0 g H_0 + \rho \hat{q} (s y - z) + \rho \hat{f}(\tilde{x}, \tilde{y}, \tilde{z}),$$

where

$$\mathcal{U} = \left(\frac{\hat{q}_r^3 s^5 Q^4}{\nu_t^3 Y^2} \right)^{1/7},$$

$$\delta = \left(\frac{Q \nu_t}{\hat{g}_r s^4 Y^4} \right)^{1/7},$$

99.

$$\beta = \left(\frac{Q^2 \nu_t^2}{s \hat{g}_r Y^8} \right)^{1/7},$$

$$\rho = \rho \left(\frac{\hat{g}_r^5 Q^2 \nu_t^2}{s Y} \right)^{1/7}.$$

The dependence of the scaling quantities on the external parameters is determined by requiring the basic viscous-gravitational balance in the horizontal momentum equations, a hydrostatic reduced pressure field, and unity dimensionless source strength. Note that the lack of a precise definition for Y is justified since any length scale selected will be artificial in the sense that it cannot appear in the solution.

Substitution of (4.1) into the equations of motion (3.3) to (3.6) results in the following dimensionless system:

$$\tilde{u}_{\tilde{x}} + \tilde{v}_{\tilde{y}} + \tilde{w}_{\tilde{z}} = 0 \quad (4.2)$$

$$\tilde{\epsilon} (\tilde{u} \tilde{u}_{\tilde{x}} + \tilde{v} \tilde{u}_{\tilde{y}} + \tilde{w} \tilde{u}_{\tilde{z}}) - R (\tilde{u} + s^2 \tilde{w}) = -\tilde{p}_{\tilde{x}} + \tilde{u}_{\tilde{z}\tilde{z}} + s^2 \delta^2 (\tilde{u}_{\tilde{x}\tilde{x}} + \delta^2 \tilde{u}_{\tilde{y}\tilde{y}}) \quad (4.3)$$

$$\tilde{\epsilon} (\tilde{u} \tilde{v}_{\tilde{x}} + \tilde{v} \tilde{v}_{\tilde{y}} + \tilde{w} \tilde{v}_{\tilde{z}}) + s^2 R \tilde{u} = -\delta^2 \tilde{p}_{\tilde{y}} + \tilde{v}_{\tilde{z}\tilde{z}} + s^2 \delta^2 (\tilde{v}_{\tilde{x}\tilde{x}} + \delta^2 \tilde{v}_{\tilde{y}\tilde{y}}) \quad (4.4)$$

and

$$s^2 \delta^2 \tilde{\epsilon} (\tilde{u} \tilde{w}_{\tilde{x}} + \tilde{v} \tilde{w}_{\tilde{y}} + \tilde{w} \tilde{w}_{\tilde{z}}) + s^2 \delta^2 R \tilde{u} = -\tilde{p}_{\tilde{z}} + s^2 \delta^2 [\tilde{w}_{\tilde{z}\tilde{z}} + s^2 \delta^2 (\tilde{w}_{\tilde{x}\tilde{y}} + \delta^2 \tilde{w}_{\tilde{y}\tilde{y}})] \quad (4.5)$$

where $\tilde{\epsilon} = \left(\frac{s^3 Q^8}{\hat{g}_r^2 \nu_t^6 Y^{11}} \right)^{1/7}$ measures convective terms (4.6)

and the influence of rotation is measured by,

$$R = \left(\frac{Q^3 s^2 Y^2}{g_r^3 v_t^4} \right)^{1/7} \hat{f} . \quad (4.7)$$

Recall that for geophysical applications the centrifugal term has been incorporated into the gravitational acceleration.

The dimensionless boundary conditions are determined from (3.9) to (3.13) and (3.16),

$$(i) \quad \tilde{u} = \tilde{v} = \tilde{w} = 0 \quad , \quad \text{at} \quad \tilde{z} = 0 \quad , \quad (4.8)$$

(ii)

$$\begin{aligned} \tilde{u}_{\tilde{z}} &= s^2 \delta^2 [-\tilde{w}_{\tilde{x}} + (\tilde{v}_{\tilde{x}} + \delta \hat{u}_{\tilde{y}}) \hat{d}_{\tilde{y}} + z \hat{u}_{\tilde{x}} \hat{d}_{\tilde{y}}] \quad , \\ \tilde{v}_{\tilde{z}} &= s^2 \delta^2 [-\delta \tilde{w}_{\tilde{y}} + 2\delta \tilde{v}_{\tilde{y}} \hat{d}_{\tilde{y}} + (\tilde{v}_{\tilde{x}} + \delta^2 \hat{u}_{\tilde{y}}) \hat{d}_{\tilde{x}}] \quad , \\ \tilde{w} &= \hat{u} \hat{d}_{\tilde{x}} + \tilde{v} \hat{d}_{\tilde{y}} \quad , \end{aligned} \quad (4.9)$$

$$\hat{p} = -(\delta^2 \hat{y} - \hat{d}) \quad , \quad \text{at} \quad \tilde{z} = \hat{d}(\tilde{x}, \hat{y}) \quad ,$$

$$(iii) \quad \tilde{d} = 0 \quad \text{at} \quad \tilde{x} = \tilde{x}_e^-(\hat{y}) \quad , \quad \tilde{x}_e^+(\hat{y}) \quad . \quad (4.10)$$

Furthermore, the dimensionless source strength is defined by,

$$\int_{\tilde{x}_e^-}^{\tilde{x}_e^+} d\tilde{x} \int_0^{\hat{d}} \tilde{v} d\tilde{z} = 1 \quad . \quad (4.11)$$

The equations governing the downstream flow are now derived by assuming that the slope is small,

$$s^2 \ll 1 \quad , \quad (4.12)$$

the flow is jet-like in the sense that the downstream scale far exceeds that in the cross-stream direction,

$$\delta^2, \delta^2 R \ll 1, \quad (4.13)$$

and the convective accelerations are negligible, i.e.,

$$\tilde{\epsilon} \ll 1. \quad (4.14)$$

Note that the last two criteria will always be satisfied for sufficiently large Y . Under these conditions the pressure is hydrostatic and the equations are simplified considerably,

$$\tilde{u}_{\tilde{x}} + \tilde{v}_{\tilde{y}} + \tilde{w}_{\tilde{z}} = 0, \quad (4.15)$$

$$-R \tilde{U} = -\hat{d}_{\tilde{x}} + \tilde{u}_{\tilde{z}\tilde{z}}, \quad (4.16)$$

$$0 = 1 - \tilde{U}_{\tilde{z}\tilde{z}}, \quad (4.17)$$

with boundary conditions,

$$(i) \quad \tilde{u} = \tilde{v} = \tilde{w} = 0 \quad \text{at} \quad \hat{\tilde{z}} = 0, \quad (4.18)$$

$$(ii) \quad \hat{\tilde{u}}_{\tilde{z}} = \hat{\tilde{v}}_{\tilde{z}} = 0, \quad (4.19)$$

$$\tilde{w} = \tilde{u} \hat{d}_{\tilde{x}} + \tilde{v} \hat{d}_{\tilde{y}}, \quad \text{at} \quad \hat{\tilde{z}} = \hat{d}(\hat{\tilde{x}}, \hat{\tilde{y}}), \quad (4.20)$$

$$(iii) \quad \hat{d} = 0, \quad \text{at} \quad \hat{\tilde{x}} = \hat{x}_e^-(\hat{\tilde{y}}), \hat{x}_e^+(\hat{\tilde{y}}). \quad (4.21)$$

The momentum equations may be integrated twice with respect to \tilde{z} , using the boundary conditions (4.18) and (4.19) to give the horizontal velocity components,

$$\tilde{u} = -\hat{d}_{\tilde{x}} \tilde{z} (\hat{d} - \tilde{z}/2) + \frac{R\tilde{z}}{3} \left(\hat{d}^3 - \frac{\hat{d}\tilde{z}^2}{2} + \frac{\tilde{z}^3}{8} \right), \quad (4.22)$$

and
$$\tilde{v} = \hat{z} (\hat{d} - \tilde{z}/2), \quad (4.23)$$

while a third integration yields expressions for the local layer fluxes,

$$\tilde{U} = -\frac{\hat{d}_{\tilde{x}} \hat{d}^3}{3} + \frac{2R}{15} \hat{d}^5, \quad (4.24)$$

and

$$\tilde{V} = \frac{\hat{d}^3}{3}. \quad (4.25)$$

The vanishing divergence of the layer fluxes [$\hat{U}_{\tilde{x}} + \hat{V}_{\tilde{y}} = 0$; see equation (3.57)] then provides a single equation governing the layer thickness distribution,

$$\hat{d} \hat{d}_{\tilde{x}\tilde{x}} + 3 \hat{d}_{\tilde{x}}^2 = 3 \hat{d}_{\tilde{y}} + 2R \hat{d}^2 \hat{d}_{\tilde{x}}, \quad (4.26)$$

which is subject to (4.21) and the appropriate condition on the downstream flow rate,

$$\int_{\tilde{x}_e^-}^{\tilde{x}_e^+} \frac{\hat{d}^3}{3} d\tilde{x} = 1. \quad (4.27)$$

Note that the layer thickness equation (4.26) nearly corresponds to equation (3.65), which was derived from the general case for arbitrary rotation on the condition that the dimensional layer thickness be much smaller than the Ekman length scale. However, in the present formulation, the jet-like character of the flow ($\delta^2 \ll 1$) has been used to eliminate downstream derivatives as compared to those in the cross-stream direction. Also, the new factor multiplying the last term in equation (4.26) arises from the difference in scaling laws. Moreover, the expressions for the horizontal velocities and layer fluxes agree to lowest order with the relations derived from the general case, (3.68) to (3.71), except for the absence of \tilde{d}_y in the downslope component and a factor of two in the integrated velocities. Thus (4.13) is the only additional constraint that has been placed on the flow up to this point.

A perturbation scheme will now be developed for the case of weak rotation,

$$R = \left(\frac{Q^3 s^2 Y^2}{g_r v_t^4} \right)^{1/7} \frac{\hat{f}}{f} \ll 1. \quad (4.28)$$

Notice, however, that the direct dependence of R on $Y^{2/7}$ implies that this assumption is ultimately violated at some downstream point. Therefore, rather than describing a true asymptotic state, the solution will govern the behavior of the flow in an intermediate range where (4.13) and (4.14) are satisfied, yet R remains small.

The analysis begins with an expansion of the layer thickness function and velocity field in powers of R ,

$$\tilde{d}(\tilde{x}, \tilde{y}) = \sum_{n=0}^{\infty} R^n d_n(x, y) , \quad (4.29)$$

$$(\tilde{u}, \tilde{v}) = \sum_{n=0}^{\infty} R^n (u_n, v_n) .$$

Since the edges of the flow are free streamlines, their positions must also be expanded in the same manner, i.e.,

$$\tilde{x}_e^{\pm}(\tilde{y}) = \sum_{n=0}^{\infty} R^n x_{e_n}^{\pm} . \quad (4.30)$$

At lowest order, the layer thickness equation takes the form

$$d_0 d_{0\tilde{x}\tilde{x}} + 3 d_{0\tilde{x}}^2 = 3 d_{0\tilde{y}} , \quad (4.31)$$

with boundary conditions,

$$(i) \quad d_{0\tilde{x}} = 0 \quad \text{at} \quad \tilde{x} = 0 , \quad (4.32)$$

$$(ii) \quad d_0 = 0 \quad \text{at} \quad \tilde{x} = \pm x_{e_0} , \quad (4.33)$$

where the basic symmetry of the non-rotating case has been utilized.

The corresponding velocity components are given by

$$u_0 = - d_{0\tilde{x}} \tilde{z} (d_0 - \tilde{z}/2) , \quad (4.34)$$

$$v_0 = \tilde{z} (d_0 - \tilde{z}/2) , \quad (4.35)$$

and the transport condition is

$$\frac{2}{3} \int_0^{\chi_{e_0}} d_0 d\tilde{x} = 1. \quad (4.36)$$

A similarity solution for this lowest-order system is derived in Sl (using slightly different notation). The resulting expression for the layer-thickness variable predicts a parabolic cross-stream profile,

$$d_0 = \frac{c}{(a\tilde{y})^{1/7}} (1-\eta^2), \quad (4.37)$$

where $\eta = \tilde{x}/(a\tilde{y})^{3/7}$ is the similarity variable,

and $a = 6.9346$, with $c = \frac{3a}{14}$.

Furthermore, the value of η on the edge streamline has been normalized to one, which implies that

$$\chi_{e_0} = (a\tilde{y})^{3/7}. \quad (4.38)$$

Therefore, the flow spreads like $\tilde{y}^{3/7}$ and thins along streamlines ($\eta = \text{const.}$) as $\tilde{y}^{-1/7}$ in the non-rotating case.

Pursuit of the problem to first order in R leads to a linear second-order equation for the layer-thickness perturbation, $d_1(\tilde{x}, \tilde{y})$,

$$d_0 d_{1\tilde{x}\tilde{x}} + 6d_{0\tilde{x}} d_{1\tilde{x}} + d_{0\tilde{x}\tilde{x}} d_1 - 3d_{1\tilde{y}} = 2d_0^2 d_{0\tilde{x}}. \quad (4.39)$$

The form of the inhomogeneity in this equation coupled with the requirement that the first-order correction carry no net transport implies that

d_1 is an odd function of \tilde{x} . Therefore the appropriate boundary condition on the centerline is,

$$d_1 = 0 \quad \text{at} \quad \tilde{x} = 0. \quad (4.40)$$

Further use of this antisymmetry property in a Taylor series expansion of the edge boundary conditions (4.21) about the lowest-order edge positions ($\tilde{x} = \pm x_{e_0}$) yields a relation between the edge perturbations and the value of d_1 , i.e.,

$$x_{e_1}^+ = x_{e_1}^- = \frac{(a\tilde{y})^{4/7}}{2c} d_1(x_{e_0}, \tilde{y}) \equiv x_{e_1}. \quad (4.41)$$

This result signifies that the first-order corrections to the edge streamlines are equal in magnitude and the direction of shift is determined by the sign of the layer-thickness correction evaluated at the non-rotating edge. The modifications to the velocity field at this order are expressed in terms of the layer thickness correction as

$$u_1 = - \left(d_0 - \frac{\tilde{z}}{2} \right) \tilde{z} d_{1\tilde{x}} - d_{0\tilde{x}} \tilde{z} d_1 + \frac{\tilde{z}}{3} \left(d_0^3 - \frac{d_0 \tilde{z}^2}{2} + \frac{\tilde{z}^3}{8} \right), \quad (4.41)$$

$$v_1 = \tilde{z} d_1. \quad (4.42)$$

Finally, the transport condition (4.27) is satisfied to order R , since both edge-streamline and layer-thickness perturbations provide no net contribution to the total downstream volumetric flow rate.

A solution for d_1 was sought in terms of the similarity variable, η , and \tilde{y} . Its form was found to be,

$$d_1(\eta, \tilde{\gamma}) = 4c^2 (a\tilde{\gamma})^{1/7} G_1(\eta), \quad (4.43)$$

where G_1 satisfies the following equation,

$$(1-\eta^2) G_1'' - 6\eta G_1' - 4G_1 = -(\eta - 2\eta^3 + \eta^5), \quad (4.44)$$

$$\text{with} \quad G_1(0) = 0 \quad (4.45)$$

$$\text{and} \quad x_{e_1} = 2c (a\gamma)^{5/7} G_1(1) \quad (4.46)$$

where ' denotes differentiation with respect to η .

The equation for G_1 is a non-homogeneous, second-order ordinary differential equation with regular singular points at $\eta = \pm 1$. The general solution consists of two complementary solutions to the homogeneous equation plus a particular solution.

The complementary solutions may be readily obtained by a change of variables: $r = \eta^2$, $g(r) = G_1(\eta)$. Under this transformation, the homogeneous form of (4.44) reduces to a hypergeometric equation,

$$r(1-r) g'' + \left(\frac{1}{2} - \frac{7}{2}r\right) g' - g = 0; \quad (4.47)$$

$$\text{with} \quad g(0) = 0. \quad (4.48)$$

The solutions to (4.47) are well known in terms of the hypergeometric function $F(a, b; c; d)$ [see Abramowitz and Stegun (1970), p. 562]

$$g(r) = D F(a, b; \frac{1}{2}; r) + E F(a + \frac{1}{2}, b + \frac{1}{2}; \frac{3}{2}; r), \quad (4.49)$$

where
$$F(a, b; c; r) = \frac{\Gamma(c)}{\Gamma(a)\Gamma(b)} \sum_{n=0}^{\infty} \frac{\Gamma(a+n)\Gamma(b+n)}{\Gamma(c+n)} \frac{r^n}{n!},$$

and
$$a+b = 5/2, \quad ab = 1 \quad (4.50)$$

The odd symmetry of d_1 as expressed by (4.48) implies that $D = 0$. Moreover, analytic continuation of the odd solution to the neighborhood of $r = 1$ reveals that,

$$g(r) \sim \frac{\Gamma(2)\Gamma(3/2)}{\Gamma(a+1/2)\Gamma(b+1/2)} (1-r)^{-2} \quad \text{as } r \rightarrow 1.$$

Therefore, the condition that the solution be bounded near $r = 1$ requires that $(b + 1/2)$ be a negative integer, i.e.,

$$b + 1/2 = -n \quad n = 1, 2, 3, \dots$$

but, according to (4.50), $b + 1/2 = 1$ or $5/2$. Thus, the odd complementary solution must be rejected on physical grounds due to its singular behavior near the edges of the flow, i.e., $E = 0$.

Lacking acceptable complementary solutions, the general expression for $G_1(\eta)$ reduces to the particular solution. Its form is found to be an odd fifth-order polynomial whose coefficients are determined by balancing like powers of η in (4.44),

$$G_1(\eta) = \frac{1}{1890} [123\eta - 110\eta^3 + 35\eta^5]. \quad (4.51)$$

The corresponding results for the layer-thickness and edge-streamline perturbations are easily computed from (4.43) and (4.46),

$$d_1(\eta, \tilde{y}) = \frac{2c^2}{945} (a\tilde{y})^{1/7} [123\eta - 110\eta^3 + 35\eta^5], \quad (4.52)$$

and

$$x_{e_1} = \frac{16c}{315} (a\tilde{y})^{5/7}. \quad (4.53)$$

Finally, these relations along with (4.37) and (4.38) may be combined to give expressions for the layer-thickness function and edge-streamline positions which are valid to order R . Upon converting to dimensional form, the solutions are

$$d(\eta, \psi) = \left(\frac{Q^2 \nu_t^2}{s \hat{q}_r^2} \right)^{1/7} \frac{c}{(a\psi)^{1/7}} \left[(1-\eta^2) + \tilde{R} \frac{2c}{945} (a\tilde{y})^{2/7} (123\eta - 110\eta^3 + 35\eta^5) \right] \quad (4.54)$$

and

$$x_e^\pm(\psi) = \left(\frac{Q \nu_t}{\hat{q}_r s^4} \right)^{1/7} (a\psi)^{3/7} \left[\pm 1 + \hat{R} (a\psi)^{2/7} \frac{16c}{315} \right], \quad (4.55)$$

where

$$\tilde{R} = R \Upsilon^{-2/7} = \left(\frac{Q^3 s^2}{\hat{q}_r^3 \nu_t^4} \right)^{1/7} \hat{f},$$

and

$$\eta = \tilde{x}/x_{e_0} = \left(\frac{\hat{q}_r s^4}{Q \nu} \right)^{1/7} x / (a\psi)^{3/7},$$

with

$$c = \frac{3a}{14}, \quad a = 6.9346.$$

Note that, as anticipated, the artificial length scale, Υ , does not appear in this result.

For purposes of comparison with experimental results, the surface velocity components may be computed by combining (4.34) and (4.35) with (4.41) and (4.42) and evaluating at $\tilde{z} = \tilde{d}$. Thus, the horizontal velo-

city field at the surface of the layer is defined in dimensional terms by

$$u_s(\eta, \gamma) = \left(\frac{5 \hat{g}_r^2 Q^5}{\nu_t^4} \right)^{1/4} \frac{c^3 (1-\eta^2)}{(a\gamma)^{6/7}} \left[\eta(1-\eta) + \tilde{R} \frac{c(a\gamma)^{2/7}}{945} \right. \\ \left. \left\{ 4\eta^2(123 - 110\eta^2 + 35\eta^4) - (1-\eta^2)(123 - 330\eta^2 + 175\eta^4) \right. \right. \\ \left. \left. + \frac{1575}{8} (1-\eta^2)^3 \right\} \right], \quad (4.56)$$

and

$$v_s(\eta, \gamma) = \left(\frac{13 \hat{g}_r^5 Q^4}{9 \nu_t^3} \right)^{1/4} \frac{c^2 (1-\eta^2)}{2(a\gamma)^{4/7}} \left[1-\eta^2 + \frac{\tilde{R} 4c}{945} (a\gamma)^{2/7} (123\eta - 110\eta^3 + 35\eta^5) \right]. \quad (4.57)$$

Furthermore, the rate at which surface streamlines diverge from the non-rotating streamlines ($\eta = \text{const.}$) may be calculated from the ratio of the surface velocity components

$$\frac{d\tilde{x}}{d\tilde{y}} = \frac{\tilde{u}_s}{\tilde{v}_s} = -\hat{d}\tilde{x} + \frac{5}{12} R \hat{d}^2,$$

or

$$\frac{d\eta}{d\gamma} = \frac{1}{Y} \left[(a\gamma)^{3/7} \frac{d\tilde{x}}{d\tilde{y}} - \frac{3\eta}{7\gamma} \right] = \frac{\tilde{R} c^2}{3780 (a\gamma)^{5/7}} (591 - 510\eta^2 + 175\eta^4). \quad (4.58)$$

This result implies that the effect of rotation is to cause all surface streamlines (including the edge) to cross lines of constant η toward positive η at a rate proportional to \tilde{R} and $\gamma^{2/7}$.

Confirmation of these and other features of the first-order solution was sought by means of the rotating fluid dynamic experiment described in the next section.

IV.2 Weak Rotation Experiment

IV.2.1 Description of Experimental Methods

In order to examine the dynamical consistency of the extended similarity solution, the source flow experiment described in S1 was modified such that it could be performed on a rotating table. A square (3 x 3 ft.) plane of 1/4-inch thick plate glass was supported by an aluminum plate and mounted on a 4-ft.-diameter rotating table at an angle of $\alpha = 11.5^\circ$ to the horizontal [Figure 4-1(a)]. Furthermore, the plane was situated such that the axis of rotation intercepted the centerline of the viscous source flow ($x = 0$). The table turned on air bearings and its speed was controlled by a Graham variable-speed transmission coupled to the motor drive. Since the experiment was carried out in the laminar regime, the appropriate value of V_t is given by the molecular coefficient. The working fluid was a mixture of silicone oils (Dow Corning 200 Fluid), blended to achieve the desired viscosity (about 50 cs.). The kinematic viscosity coefficient of the oil was measured using a Cannon-Fenske calibrated viscometer. Also, since only a single liquid layer was used, the normal component of gravity was not reduced by the density of the upper fluid (air) in this experiment, i.e., $\hat{g}_r = g \cos \alpha$.

A uniform flow rate was maintained by a constant-head device, positioned at approximately the same radius as the top of the plane so that the net potential difference between the two points is unaltered by the centrifugal field due to rotation [see Figure 4-1(b)]. The fluid emanated from a 3/4-inch-diameter tube at the head of the plane and was collected at its base in an aluminum trough. From there it was pumped back

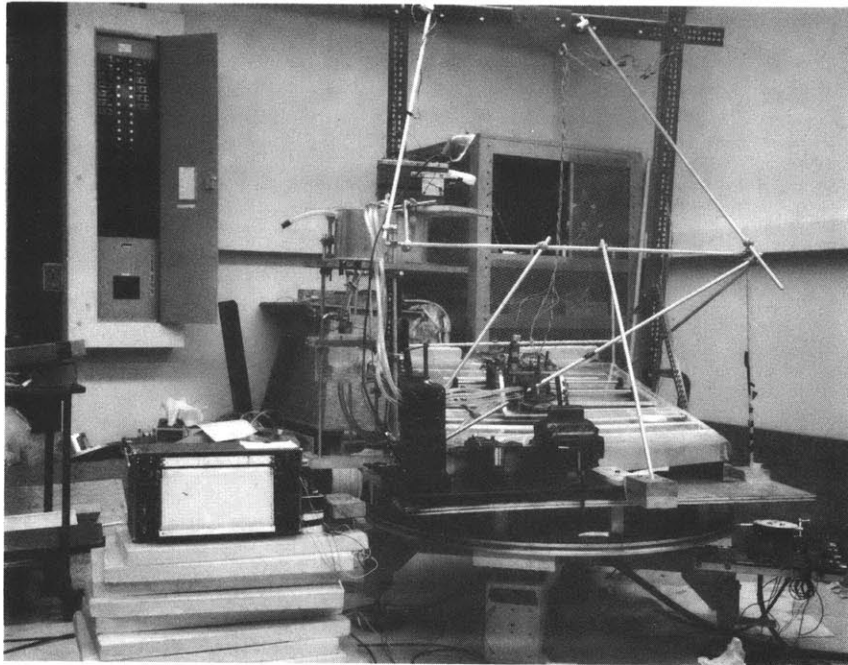


Figure 4-1(a). Overall view of experimental apparatus.

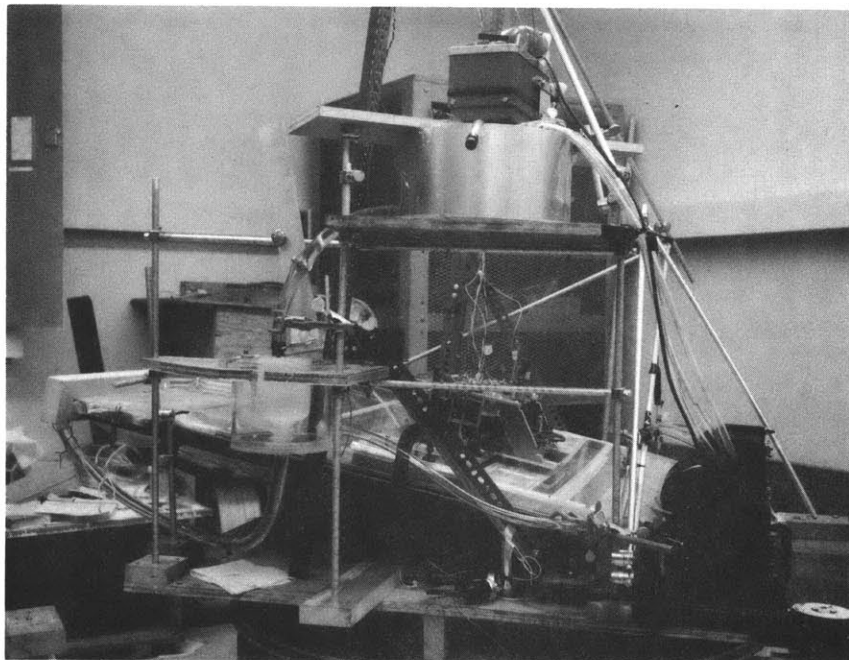


Figure 4-1(b). Circulation system (right to left): peristaltic pump, reservoir, constant-head device, source at top of plane.

into the reservoir. The flow rate was determined by measuring the volume of fluid samples taken at the end of the plane over intervals of approximately 20 sec. A plexiglas cover was used to shelter the flow from the wind field created by the rotation. To provide a basis for determining rotational effects, the non-rotating source flow was first established in each experiment and measurements were taken. Then the system was spun up and the procedure was repeated with rotation.

Two sets of measurements were taken. The first series was designed to trace the trajectory and velocity of surface particles. Small flakes of thin, glossy paper were dropped onto the surface of the oil and held there by surface tension as they were advected downstream. Using a strobe to multiply expose a photograph, the position of the flakes was marked periodically against a 0.1-inch grid which lay beneath the plane. The time lapse between strobe pulses was $.394 \pm .007$ sec. and a typical exposure shows the flake at 12 different points in the flow. High-contrast Polaroid film (type 51) was used so that the small white particles could be clearly distinguished against the darker background. The estimated accuracy with which the surface flake positions could be measured was ± 0.1 inch. Unfortunately, attempts to determine the position of the edge streamline from these photographs were frustrated by wetting of the plane during the transient stages of the experiment. The apparent edges in each picture indicated the boundary of maximum coverage by the flow over all phases of its development, and despite careful spin-up procedures, no consistent trend in the edge position could be discerned.

The aim of the second set of measurements was to determine the

layer thickness profile at a point $y = 63.6$ cm ($= 25$ in.) downstream from the source. For the purpose of traversing this section of the flow, a mechanized cart was built to run along hardened steel rods on linear bearings, driven by a small d.c. motor [see Figure 4-1(c)]. The cross-stream position of the cart was determined by counting the turns of a potentiometer coupled to the driving mechanism. A depth micrometer mounted on the carriage was driven in a direction normal to the plane by another small motor. Two separate electrical contacts, which completed a simple circuit containing a small battery, were attached to the vertical drive mechanism in order to 1) register every full revolution of the micrometer barrel (.025 in.), and 2) divide each revolution into twenty equal parts (.00125 in.). By this technique the position of the micrometer could be resolved to better than 0.001 in.

A thermistor needle probe, fastened to the tip of the micrometer arm, was used to sense the surface of the layer. Placed in one arm of a Wheatstone bridge, the probe was balanced against an identical thermistor mounted just above it in order to cancel the effects of temperature variations and local air currents. [See Figure 4-1(d).] Both the bridge output and the signal counting the micrometer turns were transmitted through the slip rings and displayed on a Mosley 7100B dual-channel chart recorder. When the probe entered the silicone oil, the bridge balance was radically altered and the layer thickness could be calculated using the micrometer reading at that point.

The reliability of the absolute thickness measurements hinges upon accurate knowledge of the distance between the glass plane and the trans-

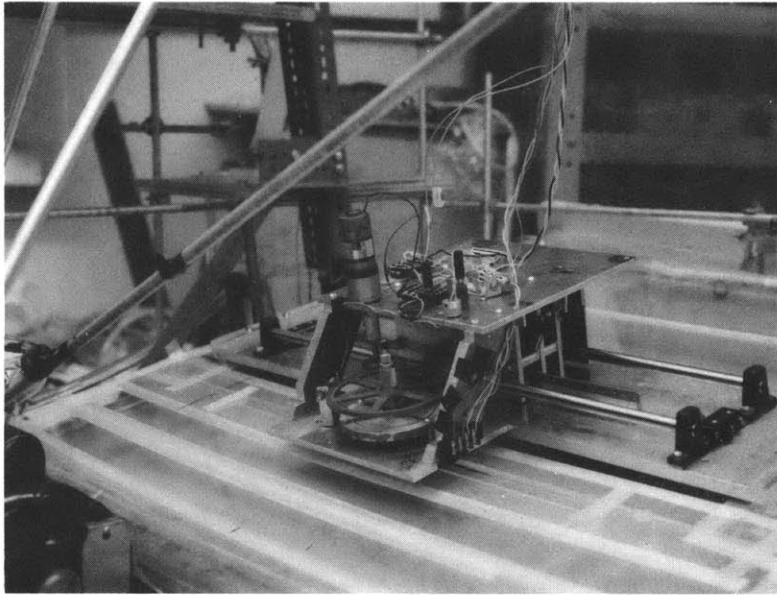


Figure 4-1(c). Horizontal traversing mechanism: motor-driven cart carrying micrometer.

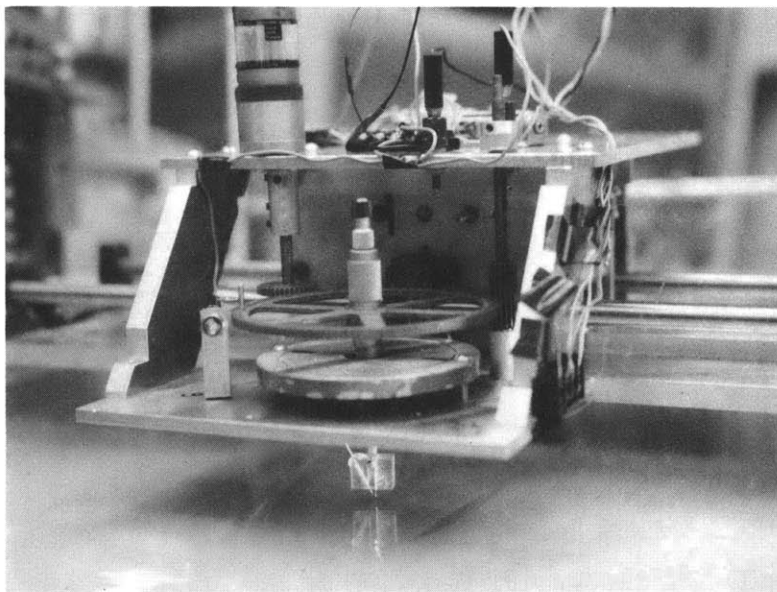


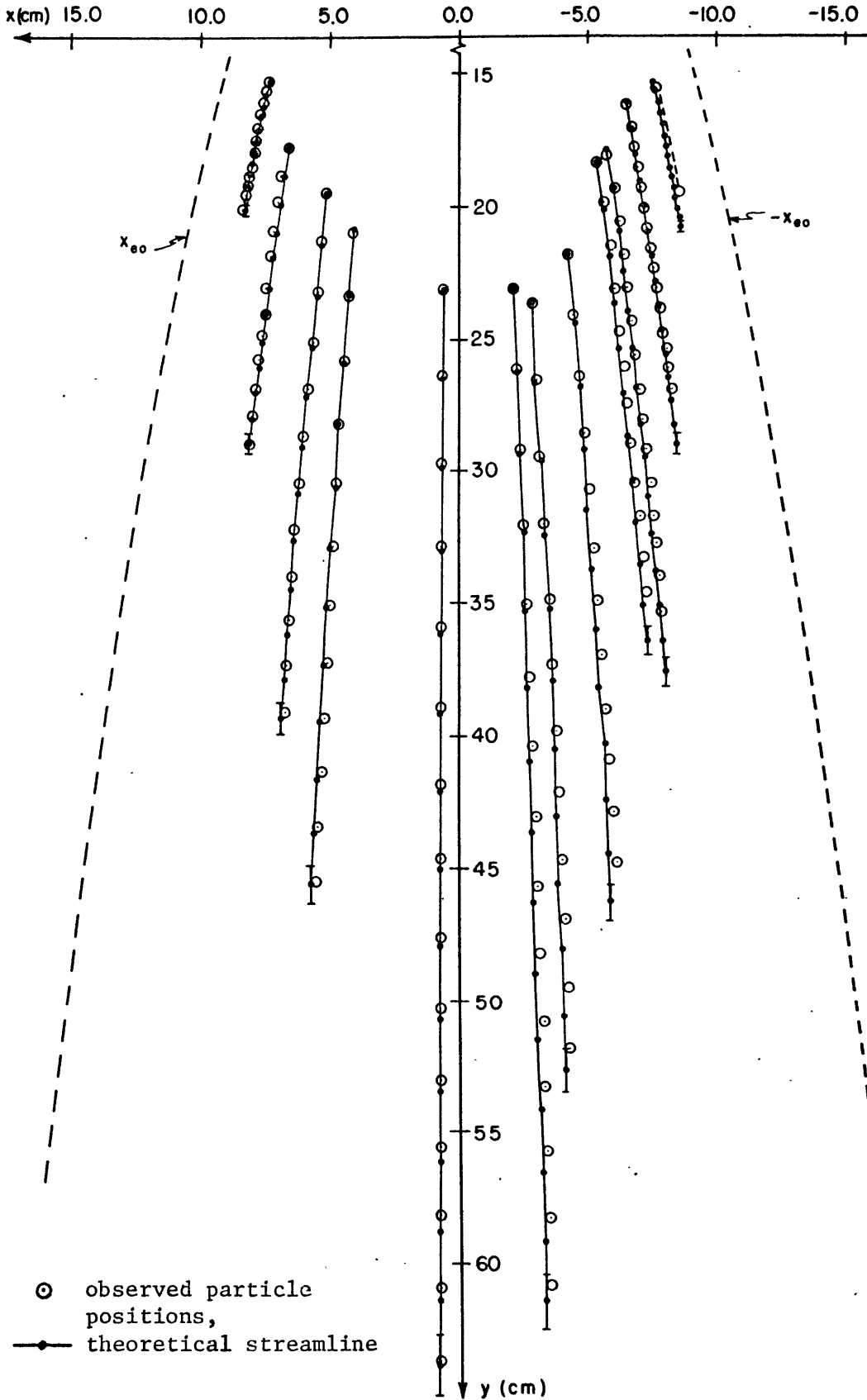
Figure 4-1(d). Close up of thermistor needle probe.

verse path of the micrometer. A small non-uniformity in this gap was traced to bending of the steel rods under the weight of the cart and leads to an uncertainty in the absolute thickness values of $\pm .0038$ cm. However, the measurement of relative thickness changes (due to rotation) at a given horizontal position were limited only by the precision to which the probe position could be determined and had an estimated error of $\pm .0008$ cm.

IV.2.2 Experimental Results

A. Streamline Data

Two surface-streamline experiments were performed with slightly different flow parameters. These quantities are listed in Table IV below. The trajectories of the surface particles in the non-rotating cases ($\hat{f} = 0$) are compared to the theoretical streamlines passing through the same initial point in Figures 4-2(a) and (b). The lowest-order edge streamline is also included for reference. Notice that the error bounds on the final theoretical points derive from uncertainties in the measured parameters. In both cases, the agreement on the lefthand side of the flow is quite satisfactory in terms of spreading and downstream displacement. However, observed streamlines in the negative half plane show a peculiar deviation from theory, not only in these results but also in rotating cases. The downstream displacements on this side of the flow are consistently smaller than predicted, while the spreading is enhanced slightly. The source of this discrepancy is believed to be related to a blockage of the flow which occurred at the righthand edge of the plane, but the detailed interaction is not understood. Fortunately, the trend is suffi-



\odot observed particle positions,
 \bullet theoretical streamline

Figure 4-2(a). Comparison of surface streamline results for non-rotating experiments with theory in Experiment 5-26.

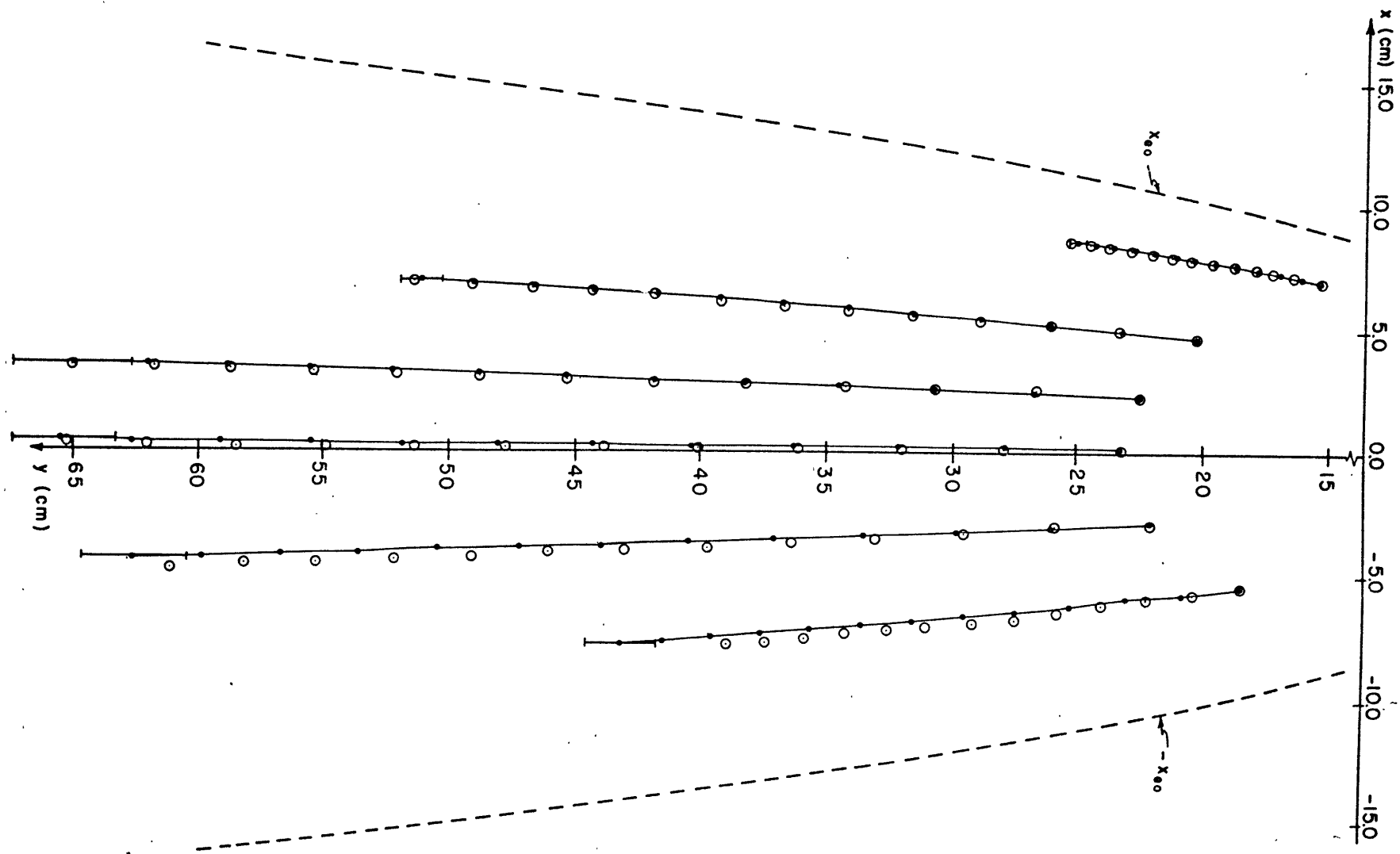


Figure 4-2(b). Comparison of surface streamline results for non-rotating experiments with theory in Experiment 5-16. \circ observed particle positions, $\text{---}\bullet\text{---}$ theoretical streamline.

<u>Parameter</u>	<u>Exp. 5-26</u>	<u>Exp. 5-16</u>
source strength, Q	$13.5 \pm .6 \text{ cm}^3/\text{sec}$	$17.5 \pm .8 \text{ cm}^3/\text{sec}$
kinematic viscosity, ν_t	$.628 \pm .017 \text{ cm}^2/\text{sec}$	$.432 \pm .010 \text{ cm}^2/\text{sec}$
slope, $s = \tan\alpha$.205	.205
normal component of gravity, \hat{g}_r	$959.3 \text{ cm}/\text{sec}^2$	$959.3 \text{ cm}/\text{sec}^2$
Coriolis parameter, $\hat{f} = 2\Omega \cos\alpha$	$\begin{Bmatrix} 0.0 \\ .74 \pm .01 \\ 1.30 \pm .01 \end{Bmatrix} \text{ sec}^{-1}$	$\begin{Bmatrix} 0.0 \\ .19 \pm .01 \\ .73 \pm .01 \\ 1.30 \pm .01 \end{Bmatrix} \text{ sec}^{-1}$

TABLE IV. Flow Parameters for Surface-Streamline Experiments

ciently systematic in the non-rotating experiments that the effect may be accounted for in the rotating results by adjusting the observed displacements by the amount of the discrepancy found at the same point in the flow for $\hat{f} = 0$. The maximum correction called for by this method was 16% of the total downstream displacement, and only points for which $\eta \leq -0.2$ were affected. The implicit assumption in this procedure is that the spurious effect operates independently from the rotation, so that the physical effects are separable.

In the absence of rotation, theory predicts that the downstream coordinate of the last flake position is given by the following formula (see S1),

$$y_{lt_0} = a^{-1} \left[(ay_i)^{9/7} + 3c^3 \left(\frac{S^5 g_r^3 Q^4}{\nu_t^3} \right)^{1/7} (1-\eta^2)^2 \Delta t \right]^{7/9}, \quad (4.59)$$

where y_i is the initial coordinate and Δt is the total time elapsed. The most striking evidence of rotation occurred in this integrated measure of downslope component of surface velocity. These results are displayed in Figures 4-3 and 4-4. For a given surface flake, the difference between the final downstream positions, with and without rotation, $(y_l - y_{lt_0})$, was normalized by the total downstream displacement in the non-rotating case $(y_{lt_0} - y_i)$ and plotted against the mean value of η over the particle trajectory. Experimental points for $\eta \leq -0.2$ (about 25% of the data) have been adjusted to account for the displacement anomalies observed in the non-rotating results.

The basic antisymmetric displacement pattern which indicates a similar structure in the surface velocity field compares well with theory

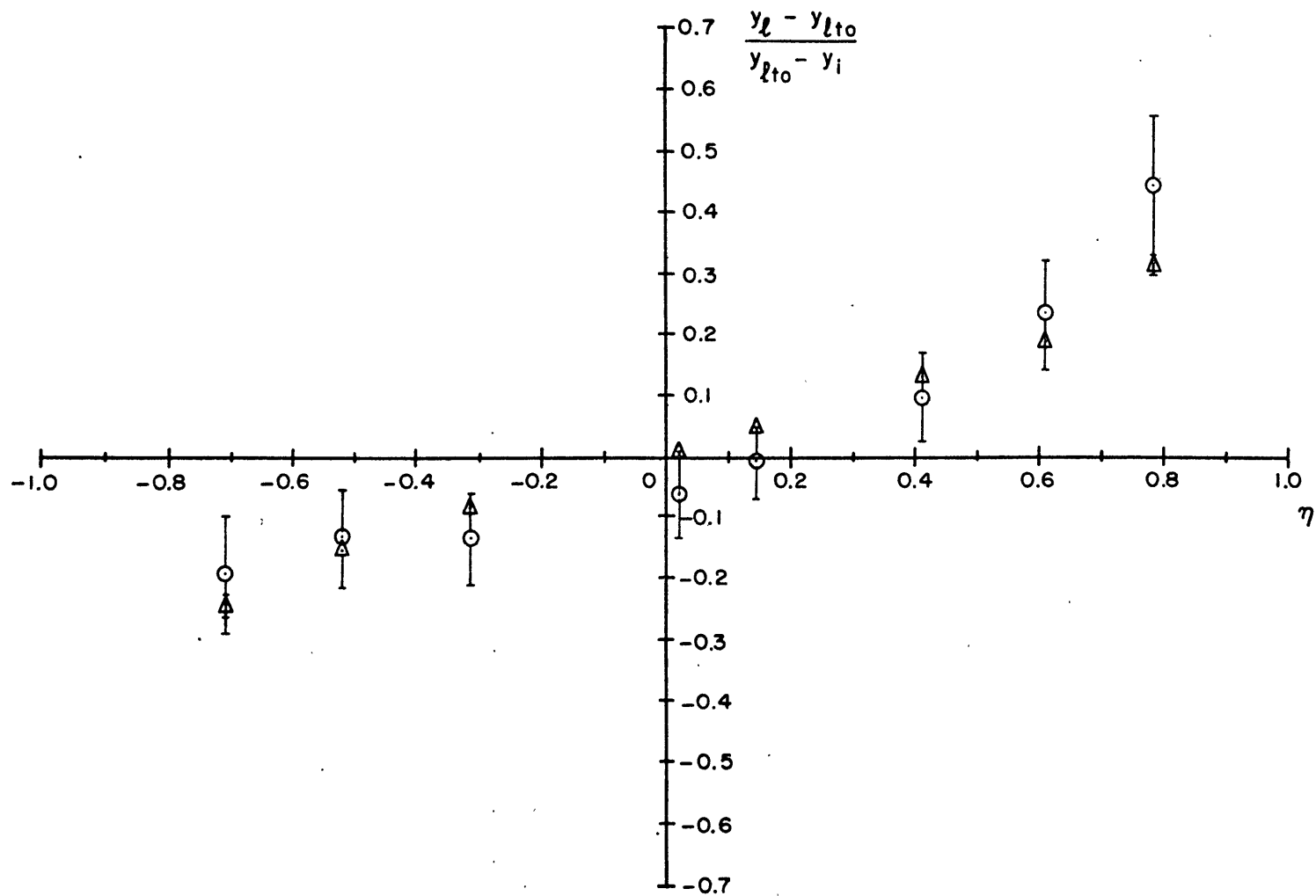


Figure 4-3(a). Excess downstream displacement vs. mean value of η on surface streamline for Experiment 5-26, $\hat{f} = 0.74 \text{ sec}^{-1}$. ○ observed differences, △ theory.

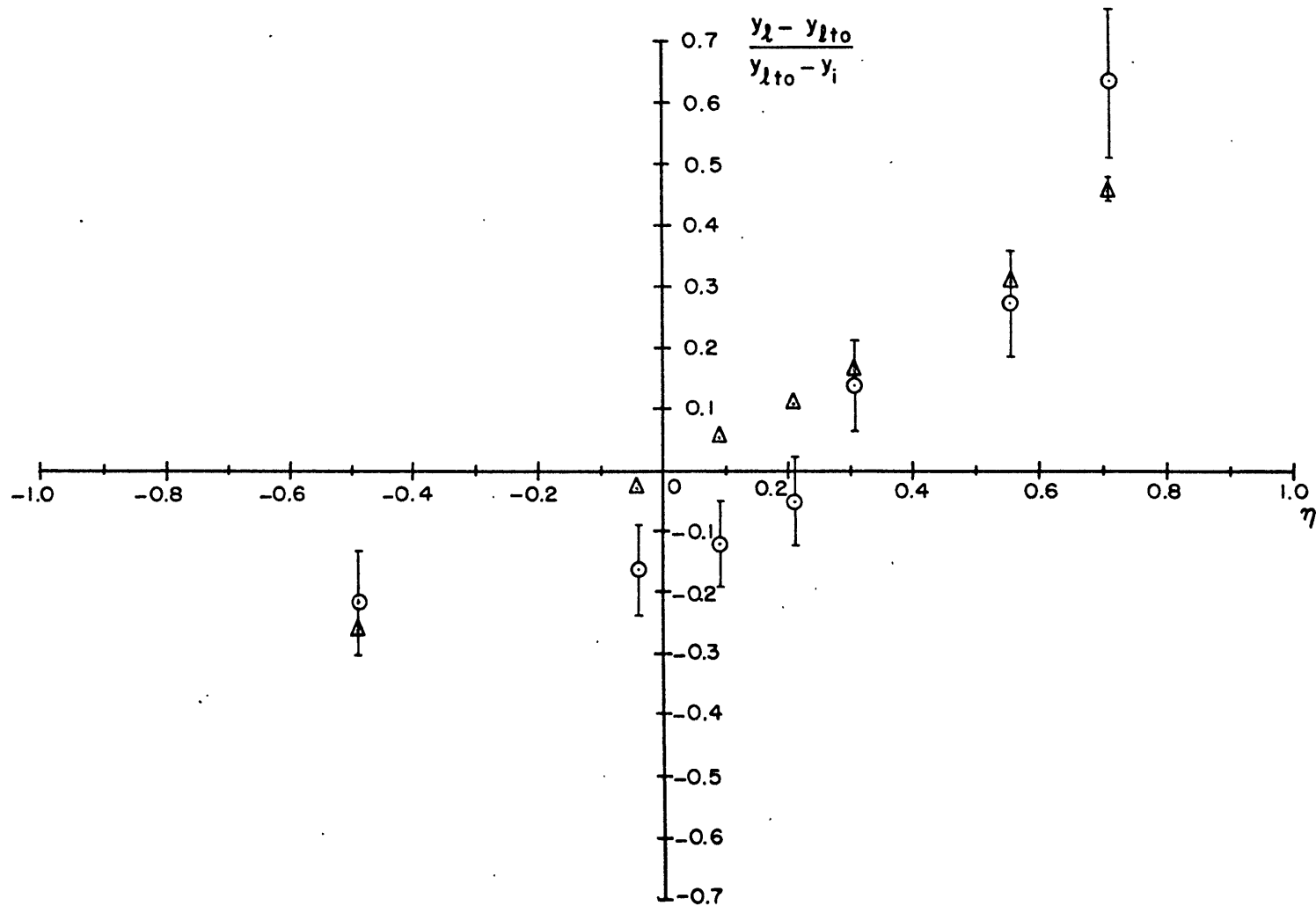


Figure 4-3(b). Excess downstream displacement vs. mean value of η on surface streamline for Experiment 5-26, $\bar{f} = 1.30 \text{ sec}^{-1}$. \circ observed differences, Δ theory.

in all cases. For the lowest rotation rate [Figure 4-4(a)], this effect is barely visible above the noise level of the measurement. At moderate speeds [Figures 4-3(a) and 4-4(b)], the perturbations are more pronounced, so the agreement with the theoretical points is more significant. However, superposed on the observed perturbation profiles for these cases are systematic deficits and excesses of downstream displacement in the central and edge regions respectively. At the highest rotation rate [Figure 4-4(c)], these discrepancies are even larger and rise substantially above the experimental error. This phenomenon is attributable to centrifugal effects which will be discussed further with regard to the thickness measurements.

The error bounds on the displacement measurements arise both from observational errors in γ_L and imprecise knowledge of γ_{L_0} due to uncertainties in the flow parameters. The error limits tend to be augmented near the edge of the flow and diminished in the center because of the opposite trend in the total displacement, $(\gamma_{L_0} - \gamma_i)$. The inaccuracy of the theoretical values corresponds roughly to the size of the triangular points except where error bars are shown explicitly.

At the small rotation rates required to minimize centrifugal influence on the surface-particle trajectories, the distinctive cross-stream features predicted by theory, i.e., the bending of the surface streamlines toward positive x , were effectively masked by observational errors and uncertainties in the flow parameters. According to the integrated surface velocity, the lateral shift due to rotation of the last particle position on the longest streamline should vary from less than 0.1 in. for the lowest rotation rates to nearly 0.4 in. at the highest speeds.

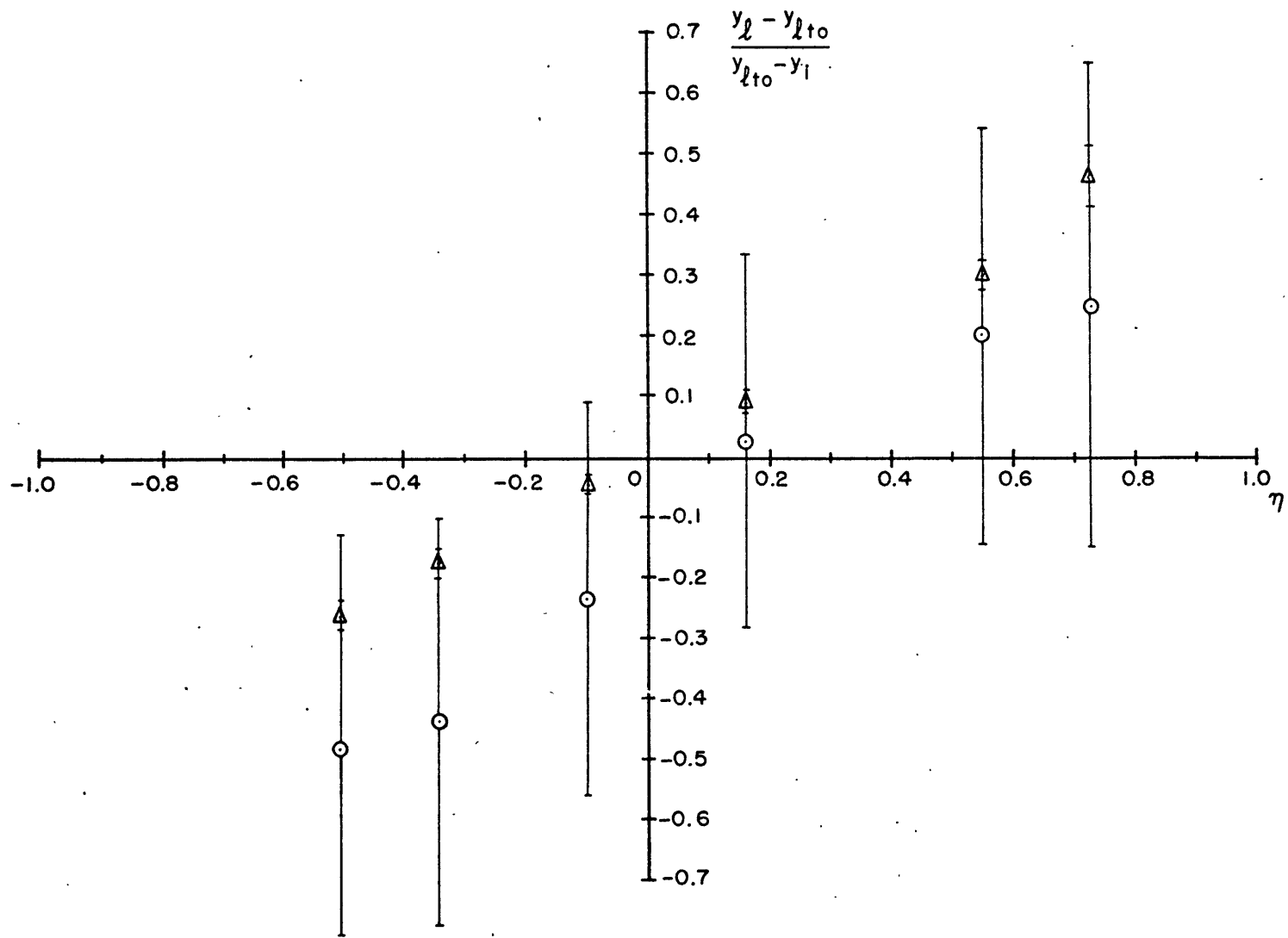


Figure 4-4(a). Excess downstream displacement vs. mean value of η on surface streamline for Experiment 5-16, $\hat{f} = 0.19 \text{ sec}^{-1}$. \odot observed differences, \triangle theory.

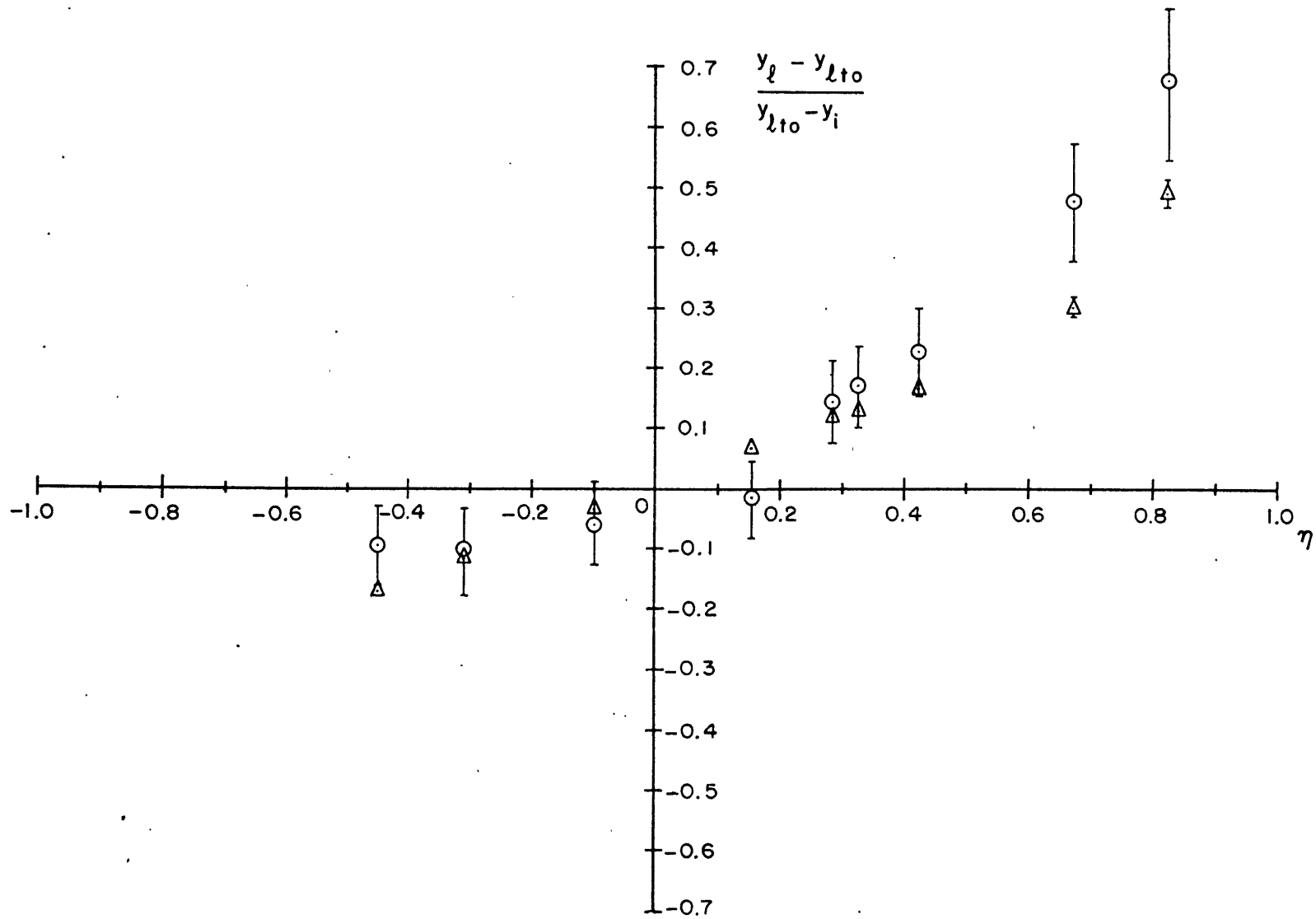


Figure 4-4(b). Excess downstream displacement vs. mean value of η on surface streamline for Experiment 5-16, $\hat{f} = 0.73 \text{ sec}^{-1}$. ○ observed differences, △ theory.

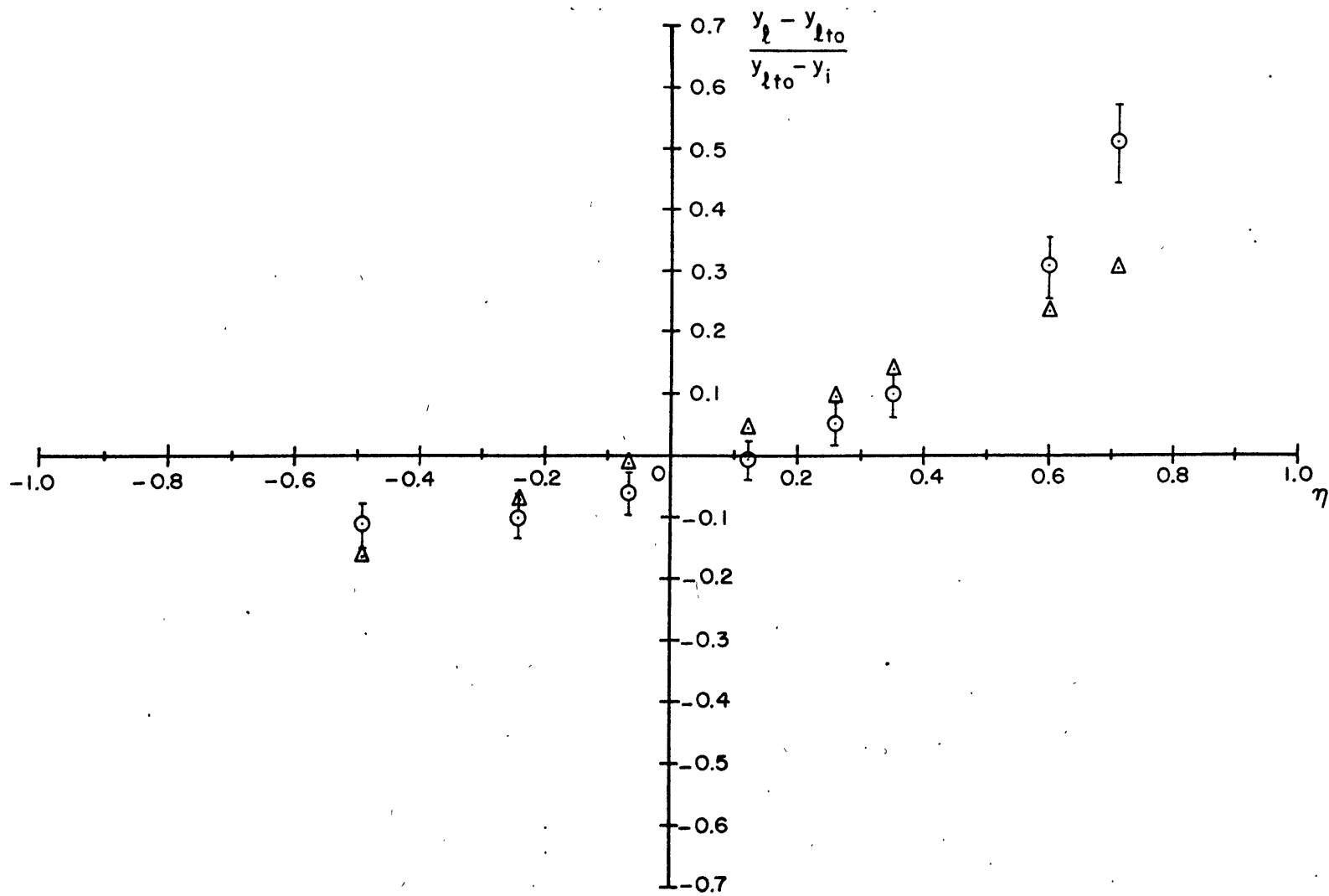


Figure 4-4(c). Excess downstream displacement vs. mean value of η on surface streamline for Experiment 5-16, $\hat{f} = 1.30 \text{ sec}^{-1}$. \odot observed differences, \triangle theory.

Although the largest of these differences could have been resolved from the photographs, the contamination by centrifugal effects was significant in those cases and the expected trend was not observed. Therefore, there was a need to corroborate the evidence offered by the downstream displacement patterns with careful measurements of the layer thickness.

B. Thickness Data

The layer thickness data derive from three separate experiments in which the thickness profile was measured at a point $y = 63.6$ cm downstream. To correct for the flow pattern anomalies observed in the streamline experiments, the source was moved closer to the center of the plane. As a result, no such inconsistency appeared in the thickness data. The parameters for each case are given in Table V, below.

Due to the excessive time (about 1 hr.) required to measure each thickness profile, it was found that the viscosity of the silicone oil changed significantly over the course of each experiment because of selective evaporation of its more volatile (less viscous) components from the large layer-surface area. The values of ν_t quoted in Table V represent mean viscosity for each trial as determined by averaging the viscometer readings taken before and immediately after each profile measurement.

A comparison between the thickness measurements in the non-rotating cases and the parabolic theoretical profile is presented in Figure 4-5. The agreement is striking in all cases, with minor discrepancies falling within the bounds of experimental error. Inaccuracies in the absolute values of d ($\pm .0038$ cm) result mainly from difficulty in gauging the distance between the micrometer and the solid plane. On the other hand,

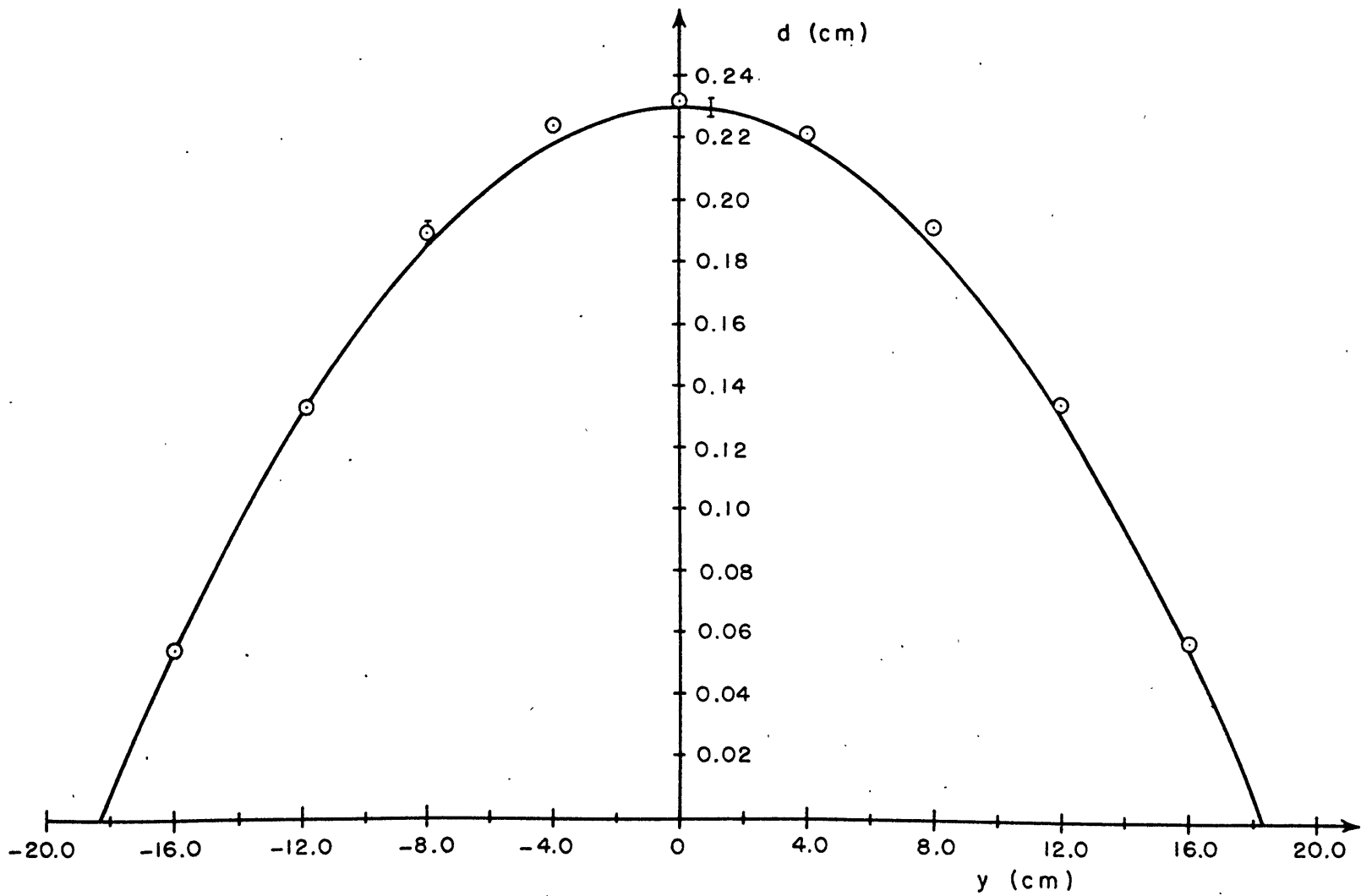


Figure 4-5(a). Comparison of measured thickness profile with theory for Experiment 6-14, $\hat{f} = 0.0 \text{ sec}^{-1}$. \odot measurement, — theory.

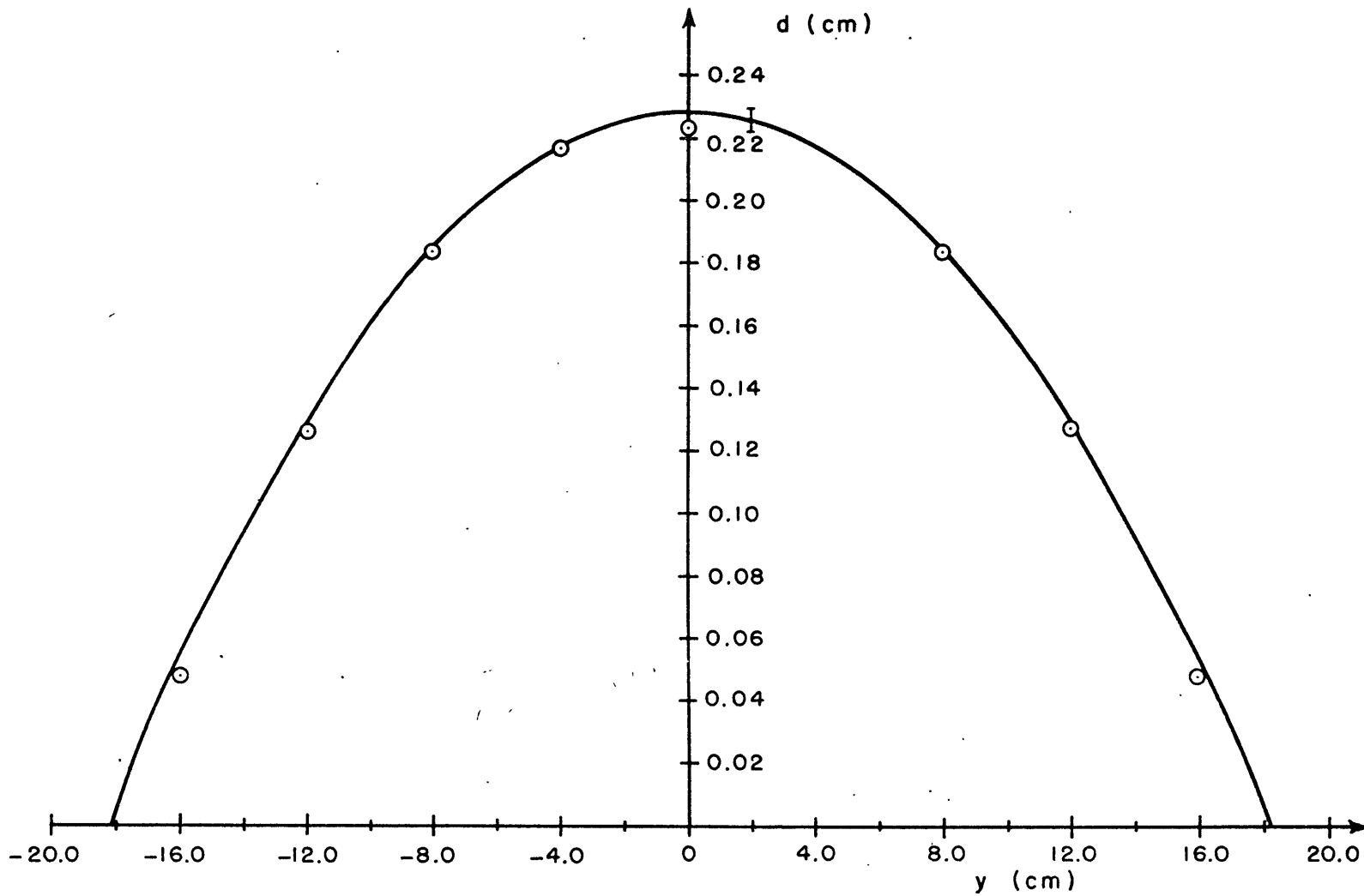


Figure 4-5(b). Comparison of measured thickness profile with theory for Experiment 6-12, $\hat{f} = 0.0 \text{ sec}^{-1}$. \odot measurement, — theory.

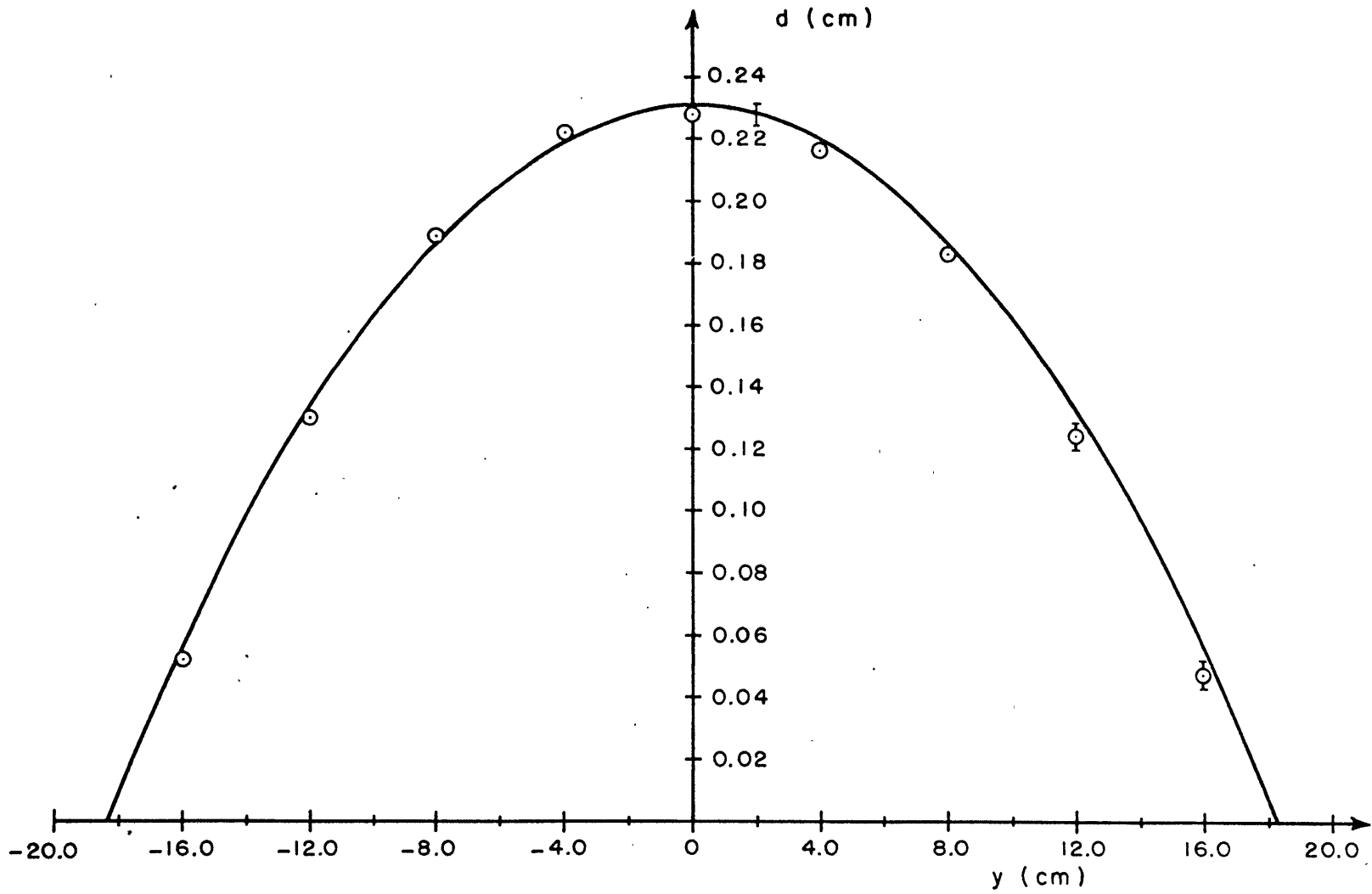


Figure 4-5(c). Comparison of measured thickness profile with theory for Experiment 6-13, $\hat{f} = 0.0 \text{ sec}^{-1}$. \odot measurement, — theory.

<u>Parameter</u>	<u>Exp. 6-14</u>	<u>Exp. 6-12</u>	<u>Exp. 6-13</u>
flow rate, Q	$14.5 \pm .3 \text{ cm}^3/\text{sec}$	$19.7 \pm .5 \text{ cm}^3/\text{sec}$	$17.3 \pm .4 \text{ cm}^3/\text{sec}$
slope, $s = \tan\alpha$.205	.205	.205
normal component of gravity, $\hat{g}_r = g \cos\alpha$	$959.3 \text{ cm}/\text{sec}^2$	$959.3 \text{ cm}/\text{sec}^2$	$959.3 \text{ cm}/\text{sec}^2$
kinematic viscosity, ν_t	$\left\{ \begin{array}{l} .917 \pm .019 \\ .955 \pm .019 \\ .974 \pm .019 \\ .993 \pm .019 \end{array} \right\} \text{ cm}^2/\text{sec}$	$\left\{ \begin{array}{l} .662 \pm .019 \\ .700 \pm .019 \end{array} \right\} \text{ cm}^2/\text{sec}$	$\left\{ \begin{array}{l} .781 \pm .019 \\ .837 \pm .019 \end{array} \right\} \text{ cm}^2/\text{sec}$
Coriolis parameter, $\hat{f} = 2\Omega \cos\alpha$	$\left\{ \begin{array}{l} 0.0 \\ .216 \pm .010 \\ .478 \pm .010 \\ .756 \pm .010 \end{array} \right\} \text{ sec}^{-1}$	$\left\{ \begin{array}{l} 0.0 \\ .750 \pm .010 \end{array} \right\} \text{ sec}^{-1}$	$\left\{ \begin{array}{l} 0.0 \\ 1.316 \pm .010 \end{array} \right\} \text{ sec}^{-1}$

TABLE V. Flow Parameters for Layer-Thickness Experiments

confidence in the theoretical curves ranges from $\pm 1.2\%$ to $\pm 1.5\%$ depending on the precision to which the flow parameters could be measured.

The thickness measurements made in the rotating system were taken at symmetric intervals across the flow and the results were decomposed into a symmetric mean profile and a skew component, i.e.,

$$d = d_m + \Delta d_a \quad (4.60)$$

where d_m is the average value for two symmetric data points and Δd_a is the observed deviation from the mean. Recall that the axis of rotation in the experiments intercepts the centerline of the non-rotating flow. This renders the centrifugal effects on the thickness profile symmetric about the y-axis. Therefore, the decomposition facilitates the comparison to theory by isolating the predicted Coriolis effects in Δd_a . Furthermore, an attempt was made to minimize calibration errors in the data by removing from Δd_a a small but systematic anti-symmetric component Δd_o which was noted in the non-rotating profiles. By placing the entire traverse on a flat mill block, the cause of Δd_o was determined to be the flexure of the traverse rods under the weight of the carriage. Finally, the data were normalized by the theoretical centerline thickness,

$$D_o = \left(\frac{Q^2 v_t^2}{S \hat{q}_r^2} \right)^{1/7} \frac{c}{(\alpha y)^{1/7}}, \quad (4.61)$$

where $y = 63.6$ cm.

The resulting measure of the influence of the Coriolis forces on

the basic viscous flow field,

$$\Delta = \frac{\Delta d_a - \Delta d_o}{D_o} , \quad (4.62)$$

is plotted against the normalized cross-stream variable, η , in Figures 4-6 and 4-7. Agreement with the theoretical curves is quite satisfactory throughout the entire range of rotation rates. The only significant departure from this pattern occurs near the edges of the flow, particularly at the higher rotation rates. One possible explanation is that horizontal position errors produce asymmetries in the measured profiles at the edge because of the steepness of the thickness gradient there. In fact, for a typical gradient of 0.02 and positional error of $\pm .058$ cm, the corresponding uncertainty in Δ (about $\pm .005$) is comparable to the observed discrepancies. Finally, the confidence limits on the theoretical contours range in magnitude from $\pm 3\%$ to 7% and are indicated by an error bar at the end of each curve. Where error bars are not shown explicitly on the data points, the bounds correspond roughly to the size of the point.

An estimate of the importance of centrifugal effects may be obtained by computing the difference between the symmetric mean profiles measured in the rotating experiments and the parabolic profile that would exist without rotation. The appropriate dimensionless measure of these differences is,

$$\Delta_c = \frac{d_m - d_t}{D_o} , \quad (4.63)$$

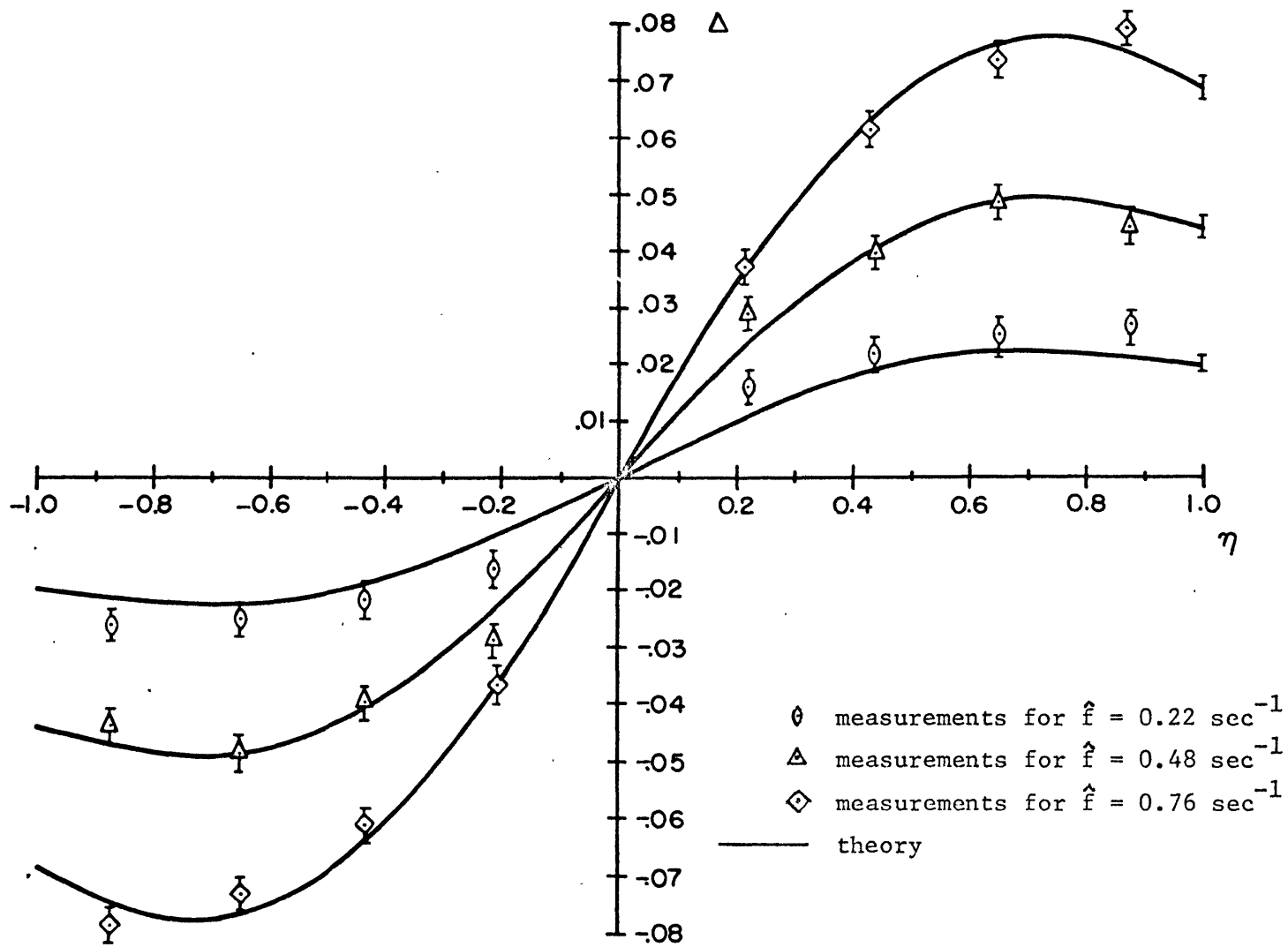


Figure 4-6. Antisymmetric perturbations to layer thickness profile for Experiment 6-14.

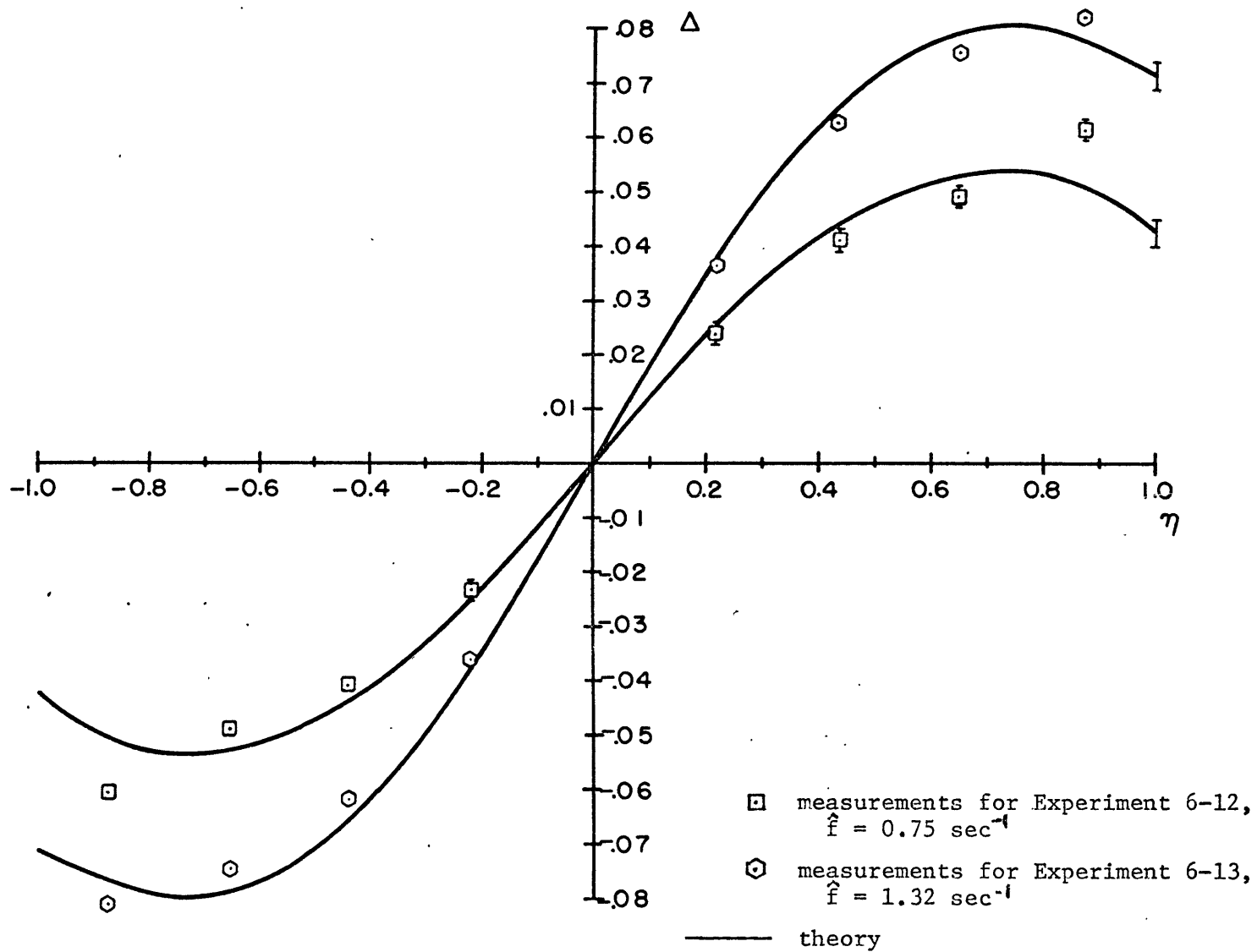
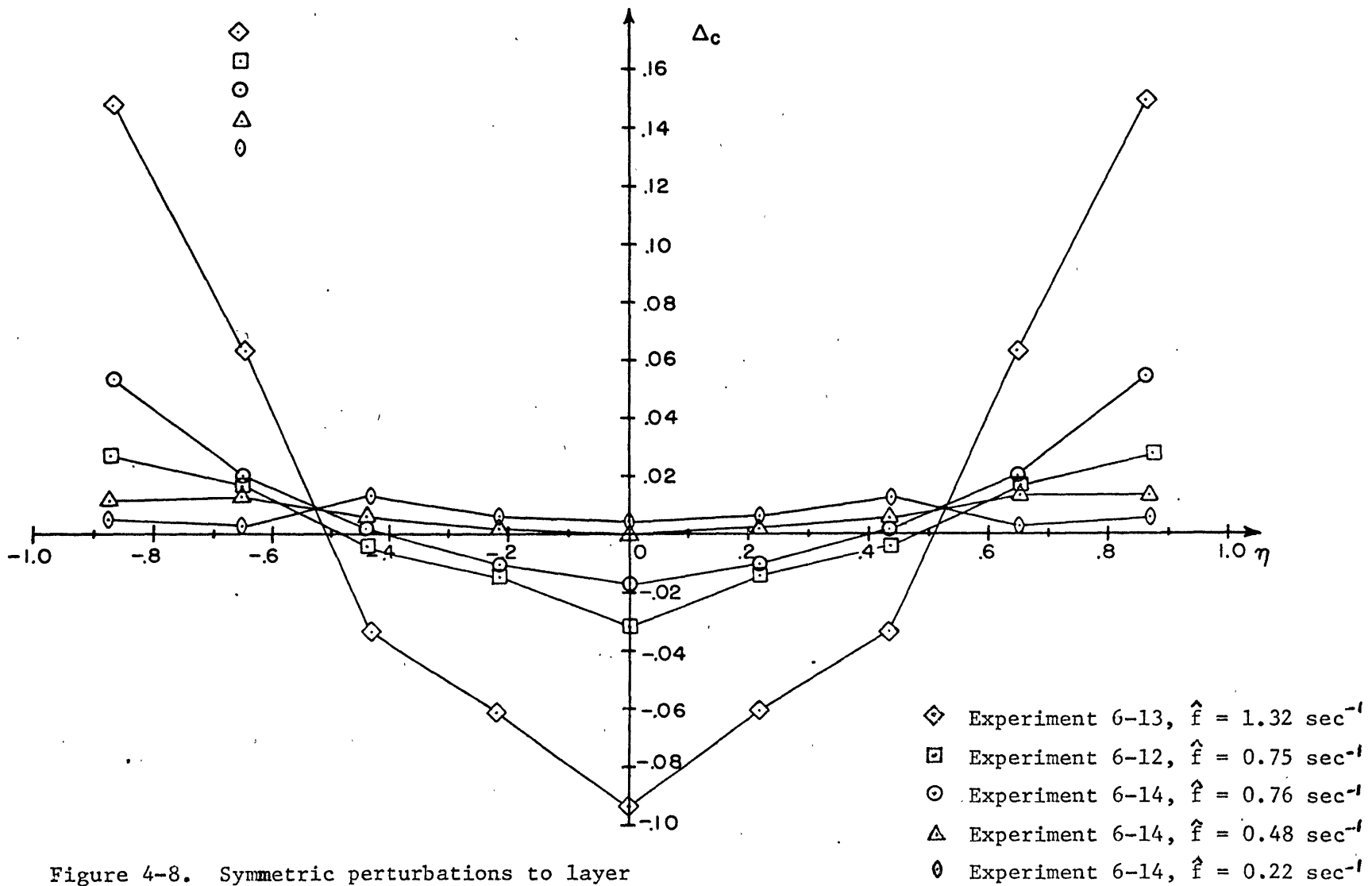


Figure 4-7. Antisymmetric perturbations to layer thickness profile.

where the subscript t signifies a theoretical calculation with $\hat{f} = 0$. Again the thicknesses have been normalized by the centerline value given by (4.61).

The centrifugal data for all three experiments is presented in Figure 4-8. As might be expected, the centrifugal forces lead to a "dishing out" of the layer-thickness profile, characterized by negative values of Δ_e in the center of the flow and positive deviations near the edge. This effect is not discernible above the noise level at the lowest rotation rate ($\hat{f} = .216 \text{ sec}^{-1}$) and is only barely visible at $\hat{f} = .478 \text{ sec}^{-1}$. However, at moderate rates ($\hat{f} = .750, .756 \text{ sec}^{-1}$), the pattern emerges and the effects are quite pronounced at the highest value, $\hat{f} = 1.316 \text{ sec}^{-1}$. Direct comparison of Figures 4-6 and 4-7 with 4-8 reveals that at moderate turning rates the magnitude of the anti-symmetric perturbations is more than twice that of the symmetric disturbances, whereas at the highest rates the levels are comparable. Therefore, the desire to maintain Coriolis forces as the dominant rotational influence constrains the Coriolis parameter to these low values for this experiment.



IV.3 Discussion

The layer-thickness experiments, together with the surface streamline results, confirm most of the important aspects of the similarity solution with weak rotation. However, in order to test the theory adequately, a careful tailoring of the experimental parameters was required to minimize extraneous influences. First of all, the rotation parameter

$$R = \left(\frac{s^2 Q^3 Y^2}{\hat{q}_r^3 \nu_t^4} \right)^{1/4} \hat{f} \quad \text{in each experiment had to be made small but finite}$$

in the region of interest. Using the coordinate of the thickness profile measurements as the downstream scale ($Y = 63.6$ cm), the value of R ranged from .104 to .776 over all experiments. At the same time, the constraints on the convective accelerations ($\tilde{\epsilon} \ll 1$) and jet-like character of the flow ($\delta^2 \ll 1$) had to be satisfied. These parameters were typically of order 10^{-2} at the thickness-measurement station. Furthermore, the flow field was subject to the implicit restriction that the interface remain stable. It was found that waves on the free surface could be suppressed by adhering to the stability criterion for the growth of long waves on a two-dimensional layer of thickness βY [see Yih (1969) p. 502], namely

$$\frac{6sRe}{5} \leq 1 \quad (4.64)$$

where $Re = \frac{\hat{q}_r s}{3\nu_t^2} \left(\frac{Q^2 \nu_t^2}{s \hat{q}_r^2 Y} \right)^{3/4} = \frac{U\beta Y}{3\nu_t}$ is the Reynolds number

based on the average velocity in the layer. Specifically in the region

where

$$Y > .118 \left(\frac{Q^6 \hat{g}_r^4 s^{11}}{\nu_t^8} \right)^{1/3},$$

all irregularities in the interface were damped and the surface appeared smooth.

Because of the intersection between the centerline of the viscous flow ($x = 0$) and the axis of rotation, it was possible to discriminate (at least qualitatively) the antisymmetric Coriolis influence from the symmetric centrifugal effects. As demonstrated by the thickness measurements, the consequence of the centrifugal forces is a "dishing out" of the thickness profile away from the mid-plane. Since the surface velocities of the lowest-order flow field are proportional to d^2 , the discrepancies noticed in the streamline experiments between observed and theoretical downstream displacements [see Figures 4-3 and 4-4] may be explained in terms of the cross-stream pattern of centrifugal thickness perturbations [Figure 4-8]. Moreover, if the radial distance from the rotation axis is represented by a characteristic cross-stream length, then a scaling argument provides an estimate of the relative magnitudes of the centripetal and Coriolis accelerations, i.e.,

$$\frac{\text{cent.}}{\text{Cor.}} \sim \frac{\hat{f}^2 \delta Y}{4 \hat{f} \nu} = \frac{\hat{f}}{4s} \left(\frac{\nu_t^4 Y^5}{\hat{g}_r^4 s^2 Q^3} \right)^{1/7}. \quad (4.65)$$

Evaluation of this ratio at the thickness measurement station ($Y = 63.6$ cm) for typical values of the flow parameters reveals that this ratio approaches unity for $\hat{f} = 5/\text{sec}$, which is in rough agreement with the experimental evidence that the two effects are comparable at $f = 1.3/\text{sec}$.

Since the theory is modelled after geophysical flows in which centrifugal effects are negligible, the desire to produce the same situation experimentally requires that the quantity in (4.65) be small.

Finally, another influence which must be considered in the laboratory flows is surface tension σ . In the rotating experiments, surface tension held fluid on portions of the plane which were wetted during the transient phases of the flow, thus disguising the position of the true edge. Furthermore, it probably played a role in producing the peculiar asymmetry observed in the non-rotating surface streamline patterns which seemed to be linked to a buildup of fluid along the righthand border of the plane. The maintenance of this blockage effect and its interaction with the rest of the flow are thought to involve surface tension to some degree. Apart from this isolated feature, however, surface tension is not expected to exert a strong influence on the basic dynamical balances within the layer. If terms involving σ are included in the theoretical formulation, then the parameter which appears in the dimensionless system to measure their importance is

$$\Gamma = \frac{\sigma}{\rho \hat{q}_r s^2 \nu^2}$$

which represents the square ratio of the surface tension length $(\sigma/\rho \hat{q}_r)^{1/2}$ to the cross-stream scale. Using the average value of ν for the silicone oil (20.8 dyne/cm.), Γ is found to be of order 10^{-4} in the region of interest and $(\sigma/\rho \hat{q}_r)^{1/2} = .15$ cm. Furthermore, if its gradients are neglected, the physical effects of surface tension

are introduced at the edges of the flow where the layer-thickness gradient must be adjusted to the proper contact angle with the solid plane. The basis for ignoring these effects is that the resulting modifications to the flow field are expected to be small (order Γ to some power) and confined to within a surface tension length scale of the edges.

With the necessary conditions satisfied and special laboratory effects accounted for, the experimental evidence of the surface-streamline and layer-thickness results demonstrates the following distinctive, rotational features of the theoretical solution:

- (i) the downstream component of surface velocity is enhanced in the positive half-plane and diminished correspondingly on the negative side, with corrections which grow with downstream distance like $y^{2/7}$;
- (ii) moreover, the layer-thickness perturbations also depend on $y^{2/7}$ and are distributed antisymmetrically across the stream according to a fifth-order polynomial in the normalized cross-stream variable, η ;
- (iii) furthermore, the lateral shifting of mass indicated by the perturbed thickness profile implies that the axis of the flow as well as all surface streamlines including the edges are systematically bent toward positive x (or η), diverging from the non-rotating streamlines ($\eta = \text{const.}$) at a rate proportional to $y^{-5/7}$.

The magnitude of the deviations from the lowest-order viscous solution is controlled by the rotation parameter $R = \left(\frac{s^2 Q^3 Y^2}{g^3 v_t^4} \right)^{1/4} \frac{\Delta}{f}$, and the

corrections are therefore directly proportional to the rotation rate.

An estimate of the range of validity of the theoretical solution is obtained by requiring $R \leq 1$, or

$$Y \leq \left(\frac{\nu_t^4 g_r^3}{f^7 s^2 Q^3} \right)^{1/2} \quad (4.66)$$

Although this constraint could be easily satisfied in the laboratory, its application to the geophysical flows considered in this study is severely limited. Specifically, if typical parameters from the Norwegian and Mediterranean outflows (Tables I and II) are combined with estimates of the turbulent eddy viscosity using Faller's formula (Chapter III), the maximum downstream scale over which (4.66) would apply is less than a kilometer. This assessment is consistent with the small values of the source flow Ekman number derived from the outflow parameters in Chapter III, which indicates that while the weak rotation analysis may apply to unusually thin outflow layers and provide useful insight into the dynamical balances which do exist, the actual outflow currents are dominated by rotation subject to weak frictional effects. The treatment of this strong rotation limit is the subject of the next chapter.

CHAPTER V

Strong Rotation in the Ekman Layer Model

The mathematical problem in the strong-rotation limit of the Ekman layer model is considerably more complicated than that for the viscous limit. Unlike the rotational perturbations to the viscous flow which could be made arbitrarily small in the limit as $R \rightarrow 0$, the frictional effects remain significant as the viscosity vanishes, but become concentrated in a very thin region adjacent to the boundary. Therefore, the major difficulties of this analysis occur near the edges of the flow where the thick-layer approximation breaks down and the general equation (3.64) must be applied to account for viscosity. Moreover, the orientation of the edge streamline is not known a priori, but must be determined as part of the solution.

Due to these complexities, an analytical solution valid over the entire flow in this limit remains inaccessible. In its place, a similarity solution for the thick central portion of the stream will be derived using a multiple-scale expansion technique. The determination of this solution is not complete however, but requires a single constant to be specified by the upstream boundary condition. A similar problem was encountered by Clarke (1968) in his analysis of two-dimensional flow of a viscous liquid jet under gravity. He found that the asymptotic expansion for the downstream flow could be fitted to a viscous solution near the orifice by matching a single variable on the symmetry axis. In the present formulation, the quantity which governs the

similarity forms is taken to be the position of the upper boundary of the thick layer, and a parametric study of the similarity forms is presented in terms of this variable. The similarity solution for the central core of the stream is supplemented by an approximate solution for the viscous edge region, which is derived by the method of characteristics and predicts the formation of a front along the upslope edge under certain conditions.

In addition to the mathematical treatment, a series of exploratory experiments will be described whose purpose was to test certain aspects of the theoretical results while providing further insight into the analysis. Despite temporal variability in the laboratory flow, the qualitative features of the approximate solutions are confirmed. However, the poor quality of the detailed measurements precludes making a quantitative comparison with theory. The general picture which emerges from the combined results of theory and experiment is that viscous processes acting along the lower boundary of the central core pump dense fluid down the slope in a thin layer of Ekman scale and thereby drain the geostrophic layer over a downstream distance proportional to the source flow length scale $L_1 = \left(\frac{\hat{q} Q}{\hat{q}_r s^2} \right)^{1/2}$ magnified by the inverse square root of the Ekman number, $E = \nu_t \hat{q}_r / \hat{q}^2 Q$. The similarity solution, once determined, provides an estimate for the extinction point of the thick layer beyond which the strong rotation approximation breaks down and the equations for the general case apply.

The theoretical analysis will be presented in the next section, followed by a description of the experiment and a discussion of the results.

V.1 Approximate Theories for the Strong-Rotation Limit of the Ekman-Layer Model

As demonstrated in Chapter III, the general equation (3.64) governing the layer-thickness distribution in the Ekman layer model reduces to a simple diffusion equation, (3.72), in the limit where the layer thickness greatly exceeds the Ekman scale. In order to make use of this approximation, the flow field in the downstream region will be divided into three regimes as illustrated in Figure 5-1. In the central portion (region II), the layer is thick and the flow is basically geostrophic with an Ekman layer near the bottom. This region is assumed to be simply connected and bounded by two contours $\psi = \psi_T^\pm(x)$ along which the layer thickness approaches the Ekman scale [$d = O(1)$] and the simple diffusion equation ceases to apply.

Bounding the central core are the upper- and lower-edge zones (regions I and III), in which the thickness varies from the scale of the Ekman layer at the transition lines to zero at the edge streamlines, $\psi = \psi_e^\pm(x)$. The disappearance of the overlying geostrophic current in these regions means that the characteristic Ekman spiral is no longer required and the dynamic effects of rotation and viscosity are comparable throughout the layer. Although its orientation is unknown, the existence of a distinct edge streamline near the upper boundary of the thick layer is assured, since there is no physical mechanism in the viscous regime by which the dense fluid can propagate up the slope. Moreover, the downstream component of velocity in the adjacent geostrophic flow implies an Ekman flux away from the upper edge. Clearly, this cross-stream transport must vanish near $\psi = \psi_T^-(x)$, since the viscous

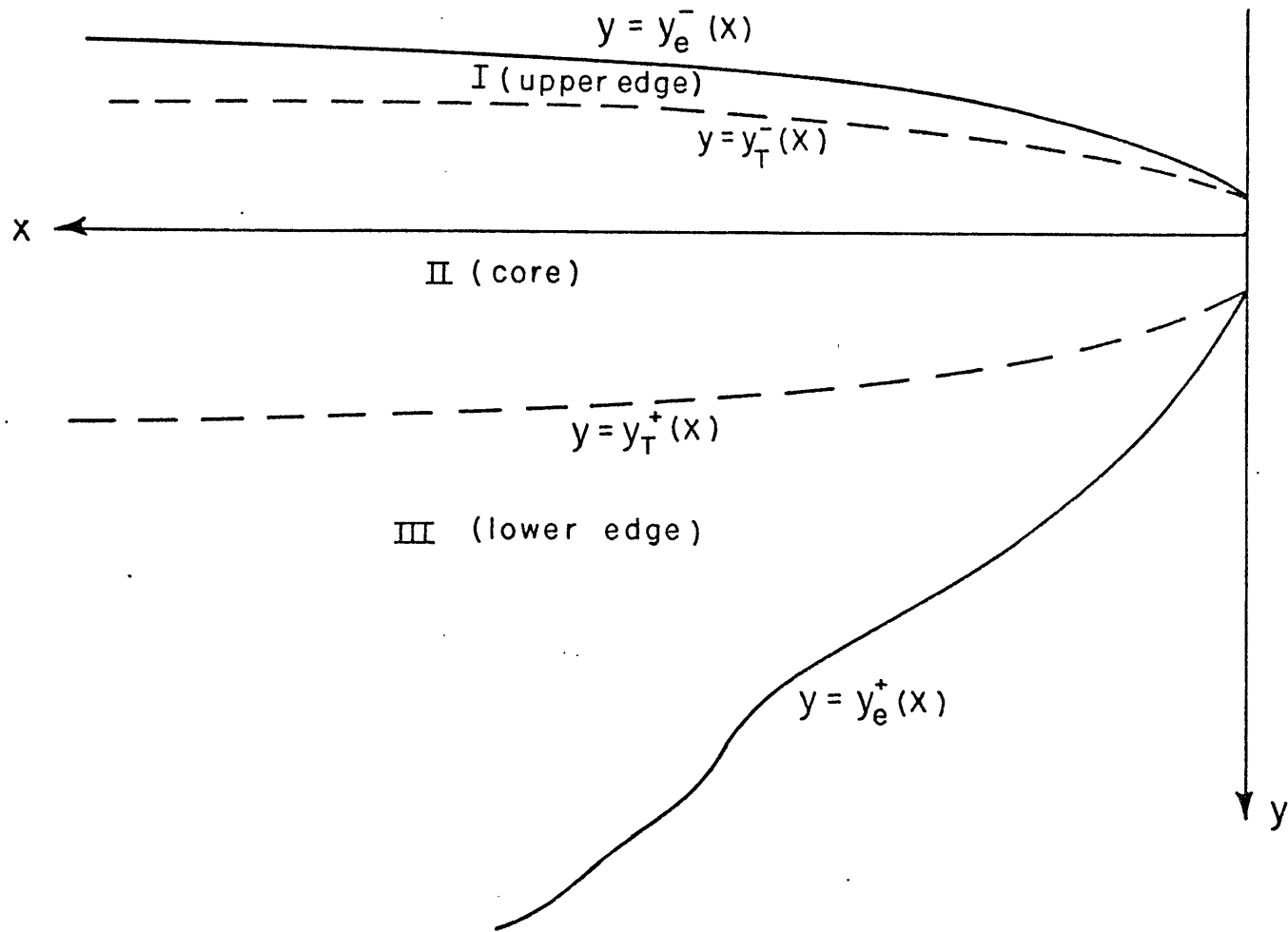


Figure 5-1. Flow regimes for strong rotation limit.

zone has no sources of mass. Thus, the upper edge region is narrow and passive and contains very little mass.

On the other hand, the shape of the lower-edge streamline is not evident. The Ekman flux out of the geostrophic layer at $y = y_T^+(x)$ continually feeds fluid into the lower edge region where its deceleration by the viscous forces causes the flow to spread out in downslope direction. The analysis of the weak rotation limit indicates that the free edge of a source flow in this regime is deflected toward positive x at a very slow rate proportional to $y^{2/7}$. Nevertheless, because of the limitations of the perturbation scheme, it is not possible to state categorically that a distinct lower-edge streamline exists at finite y over the entire downstream range considered in the following analysis. The point is moot, however, since the lowest-order solution in the central region may be derived by specifying continuity conditions along the transition contours, $y = y_T^\pm(x)$, and does not require a detailed knowledge of the solution in the lower edge regime. Moreover, the treatment of the viscous zone near the upper edge by the method of characteristics provides a local solution which is based on initial data along the source profile and is independent of the dynamics near the lower edge.

V.1.1 Multiple-scale Analysis of the Central Region

For the purpose of applying a two-scale expansion procedure to the flow in the thick geostrophic core of the stream, the dimensionless variables of the source flow scaling will be utilized. The relationship between these variables and those under the Ekman layer scaling is expressed in terms of the square root of the source flow Ekman number, i.e.,

$$(\hat{x}, \hat{y}, \hat{d}) = 2\gamma (\bar{x}, \bar{y}, \bar{d}), \quad (5.1)$$

where $\gamma = (E/2)^{1/2}$ and $E = \frac{Vg_r}{f^2 Q}$.

In this system, the strong rotation limit of the layer thickness equation takes the form,

$$\gamma (\hat{d} \hat{x} \hat{x} + \hat{d} \hat{y} \hat{y}) = \hat{d} \hat{x} \quad (5.2)$$

Notice that, in these terms, the transition to the viscous edge regime occurs where the dimensionless layer thickness is order γ , that is,

$$\hat{d} = O(\gamma) \quad \text{at} \quad \hat{y} = \hat{y}_T^{\pm}(\hat{x}). \quad (5.3)$$

To complete the formulation of the problem for the core region, the vanishing of the cross-stream transport on the upslope side of the flow is specified, i.e.,

$$\hat{V} = 0 \quad \text{at} \quad \hat{y} = \hat{y}_T^-(\hat{x}). \quad (5.4)$$

Then the form of the conservation principle for the downstream flow rate may be revised as follows. If the integral in equation (3.35) is divided into three intervals across the edge and central sections,

$$\mathbf{1} = \left\{ \int_{\hat{y}_e^-}^{\hat{y}_T^-} + \int_{\hat{y}_T^-}^{\hat{y}_T^+} + \int_{\hat{y}_T^+}^{\hat{y}_e^+} \right\} \hat{U} d\hat{y}, \quad (5.5)$$

then the mass carried in the upper edge zone is negligible. Moreover,

the ambiguity associated with the position of the lower edge streamline may be avoided by relating the flux in the last segment of (5.5) to the accumulation of cross-stream transport at the lower boundary of the core region, i.e.,

$$\int_{\hat{y}_T^+}^{\hat{y}_e^+} \hat{U} d\hat{y} = \int_0^{\hat{x}} \hat{V} \Big|_{\hat{y}=\hat{y}_T^+} d\hat{x}.$$

Thus, the modified version of the integral constraint appropriate to the analysis of the thick layer is

$$\int_{\hat{y}_T^-}^{\hat{y}_T^+} \hat{U} d\hat{y} = 1 - \int_0^{\hat{x}} \hat{V} \Big|_{\hat{y}=\hat{y}_T^+} d\hat{x}, \quad (5.6)$$

where the expressions for the local layer fluxes in source flow variables are given by

$$\hat{U} = (1 - \hat{d}\hat{y}) \hat{d} - \gamma [1 - \hat{d}\hat{y} + \hat{d}\hat{x}], \quad (5.7)$$

and

$$\hat{V} = \hat{d}\hat{x} \hat{d} + \gamma [1 - \hat{d}\hat{y} - \hat{d}\hat{x}]. \quad (5.8)$$

Notice that the flow rate in the central zone is not constant but is diminished by losses due to the Ekman flux at its downslope edge.

The appearance of the small parameter, γ , multiplying the diffusion terms in equation (5.2) indicates that the weak influence of friction acts over a long distance in the downstream direction. This implies the existence of a long downstream scale defined by,

$$X = \gamma \hat{x}, \quad (5.9)$$

and forms the basis for the multiple-scale analysis. Assuming the layer thickness is a function of this variable as well as the other geometrical coordinates, \hat{d} is expanded in an asymptotic series of the form,

$$\hat{d}(\hat{x}, \hat{y}, X) = \sum_{n=0}^{\infty} \gamma^n d_n(\hat{x}, \hat{y}, X) = d_0 + \gamma d_1 + O(\gamma^2). \quad (5.10)$$

In addition, the locations of the transition lines depend on γ and are expressed by similar expansions,

$$\hat{y}_{T^{\pm}}(\hat{x}, X) = \sum_{n=0}^{\infty} \gamma^n y_{T_n^{\pm}}(\hat{x}, X) = y_{T_0^{\pm}} + \gamma y_{T_1^{\pm}} + O(\gamma^2). \quad (5.11)$$

Notice that the lowest-order contours do not correspond to the inviscid edge streamlines because of the explicit dependence of $y_{T_0^{\pm}}$ on X . These asymptotic sequences are associated with the limit process, $\gamma \rightarrow 0$ for fixed \hat{x} , and represent an application of the general two-variable expansion procedure set forth by Cole (1968).

The object of the two-variable technique is to construct an expansion of the solution in such a way that the first term is uniformly valid over the region of interest. In the present case this is accomplished by allowing the basic solution to be modulated on the long downstream scale, thereby eliminating secular growth of the first-order corrections on the short downstream scale, \hat{x} . Substituting the expansions (5.10) and (5.11) into (5.2) to (5.8) then equating like orders in γ leads to the following sequence of problems. At order one,

$$d_{0\hat{x}} = 0 \quad \therefore d_0 = d_0(\hat{y}, X), \quad (5.12)$$

with $d_0 = 0$ at $\hat{y} = \gamma_{\tau_0}^{\pm}(X)$, (5.13)

and
$$\int_{\gamma_{\tau_0}^-}^{\gamma_{\tau_0}^+} d_0 d\hat{y} = 1 - X + \int_0^X d_0 \hat{y} \Big|_{\hat{y} = \gamma_{\tau_0}^+} dX. \quad (5.14)$$

Thus, on the short downstream scale, $0 \leq \hat{x} \ll \gamma$, the layer thickness profile is invariant with \hat{x} and the geostrophic flow parallels bottom contours. According to (5.14), however, the initial dimensionless transport of unity in the thick layer is strongly modified on the long downstream scale. In fact, the form of the last two terms in this expression, which represent an integration of the Ekman flux at $\hat{y} = \gamma_{\tau_0}^+$ over X , implies that the core region is destroyed for X of order one. In dimensional terms, this means that the geostrophic layer is entirely drained at a distance of approximately $\gamma^{-1} L$ downstream.

At order γ , the thickness equation leads to the following relation between the lowest- and first-order variables,

$$d_{1\hat{x}} = d_0 \hat{y} \hat{y} - d_0 X$$

To insure uniform validity of d_0 over the scale of X , secular growth of d_1 on the short downstream scale is eliminated by setting the right-hand side of this equation to zero, i.e.,

$$d_0 \hat{y} \hat{y} = d_0 X. \quad (5.15)$$

Furthermore the vanishing of the cross-stream transport at the upper boundary, (5.4), provides a value for the thickness gradient there,

$$d_0 \hat{y} = 1 \quad \text{at} \quad \hat{y} = \gamma_{\tau_0}(X) . \quad (5.16)$$

This condition implies that, to lowest order, the interface of the dense fluid intersects the sloping bottom horizontally (i.e., $d_y = s$) and the flow stagnates, as demonstrated by substituting (5.16) along with (5.12) and (5.13) into (5.7) and (5.8).

Thus the lowest-order layer-thickness distribution in the downstream region is governed by (5.13) to (5.16). Although the present analysis will not be extended to higher order, it is worth noting that all corrections to the thickness profile in this formulation satisfy the same equations:

$$d_n \hat{y} \hat{y} = d_n X \quad \text{for } n = 1, 2, 3, \dots,$$

due to the linearity of (5.2).

Because of the absence of a natural length scale for the rotationally dominated flow in the downstream region, a similarity solution was sought for d_0 . The form of the similarity function was selected by reference to the transport condition (5.14),

$$d_0(\hat{y}, X) = f(r) F(\xi) , \quad (5.17)$$

where $r = 1 - X$ and $\xi = g(r) \hat{y}$. The general forms of f and g are determined by substituting (5.17) into the governing equation (5.15) and imposing the conditions of similarity, so that

$$\begin{aligned} f &= c (ar + b)^{-n/2} , \\ g &= (ar + b)^{-1/2} , \end{aligned} \quad (5.18)$$

and

where a , b , and c are free constants. If these expressions are substituted into (5.14), then a balance between the transport in the thick layer and the first two terms on the righthand side requires that

$$n = -1.$$

With this determination of the scaling function, it is convenient to re-define the similarity variable in order to eliminate free constants in the equation for F , i.e.,

$$\eta = \left(\frac{a}{2}\right)^{1/2} \xi = \hat{Y}/(2r+b')^{1/2} \quad \text{where} \quad b' = \frac{2b}{a} \quad . \quad (5.19)$$

Thus the similarity function, $F(\eta)$, is governed by the following ordinary differential equation,

$$F'' - \eta F' + F = 0 \quad (5.20)$$

where ' denotes differentiation with respect to η . Furthermore, the layer thickness is given by,

$$d_0(\hat{Y}, X) = D (r + b'/2)^{1/2} F(\eta) , \quad (5.21)$$

where $D = ca^{1/2}$, and the transition contours are related to the constant limiting values of η along which F vanishes, i.e.,

$$F(\eta^+) = F(\eta^-) = 0 , \quad (5.22)$$

and

$$\gamma_{\tau_0}^{\pm} (X) = (2r+b')^{1/2} \eta^{\pm}. \quad (5.23)$$

In terms of the similarity solution, the transport relation, (5.14), may be rewritten as follows:

$$\left[2^{1/2} \mathcal{D} (1+b'/2) \int_{\eta^-}^{\eta^+} F d\eta - 1 \right] - \left[2^{1/2} \mathcal{D} \int_{\eta^-}^{\eta^+} F d\eta - 1 + \frac{\mathcal{D}}{2^{1/2}} F'(\eta^+) \right] X = 0.$$

In order to satisfy this condition in general, both the constant term and the coefficient of X must vanish. This requirement leads to the following expressions for the free constants,

$$b' = F'(\eta^+) / \int_{\eta^-}^{\eta^+} F d\eta, \quad (5.24)$$

and

$$\mathcal{D} = 2^{1/2} / \left[2 \int_{\eta^-}^{\eta^+} F d\eta + F'(\eta^+) \right]. \quad (5.25)$$

Finally, the boundary condition on the cross-stream thickness gradient, (5.16), reduces to

$$1 = d_0 \hat{\gamma} \Big|_{\eta = \eta_{\tau_0}^-} = \frac{\mathcal{D}}{2^{1/2}} F'(\eta^-), \quad (5.26)$$

or, making use of (5.25),

$$F'(\eta^-) - F'(\eta^+) = 2 \int_{\eta^-}^{\eta^+} F d\eta. \quad (5.27)$$

Notice that the success of the similarity approach hinges on the disappearance of explicit dependence of $d_0 \eta$ on X . This insures the proper form of the boundary condition at the upper transition contour, (5.26), and allows the downstream integration in the transport condition to be performed along the lower contour, $\eta = \eta^+$.

As a result of the similarity transformation, the shape of the cross-stream thickness profile is governed by equation (5.20) with boundary conditions (5.22) and (5.27). Recognizing that the similarity function obeys Hermite's equation ($y'' - xy' + my = 0$) for $m = 1$, a change of variables,

$$z = \eta^2 / 2, \quad G(z) = F(\eta),$$

transforms (5.2) into a confluent hypergeometric equation,

$$z G_{zz} + \left(\frac{1}{2} - z\right) G_z + \frac{1}{2} G = 0,$$

which has a regular singular point at $z = 0$ and an irregular singular point at $z = \infty$. The general solution to this equation is well known in terms of confluent hypergeometric functions [see Abramowitz and Stegun (1970), p. 492]. Returning to the similarity variables, the solution for $F(\eta)$ is given by,

$$F(\eta) = A\eta + B M(\eta), \quad (5.28)$$

where

$$M(\eta) = M\left(-\frac{1}{2}, \frac{1}{2}, z\right) = \frac{\Gamma(1/2)}{\Gamma(-1/2)} \sum_{n=0}^{\infty} \frac{\Gamma(-1/2+n)}{\Gamma(1/2+n)} \frac{\eta^{2n}}{2^n n!}, \quad (5.29)$$

is a convergent infinite series known as Kummer's function, and the linear term is the first Hermite polynomial. Noting that the amplitude of the layer thickness is prescribed by D , the value of B may be set to one without loss of generality, i.e.,

$$B \equiv 1 \quad (5.30)$$

and A then measures the partitioning of d_0 between its symmetric and antisymmetric components.

The boundary conditions must now be used to determine relations among the free constants η^+ , η^- and A which appear in the solution. Notice that the expression given in (5.27) is not a true boundary condition but a particular integral of the governing equation for F . To show this, (5.20) is written in the form

$$F'' - (\eta F)' + 2F = 0, \quad (5.31)$$

which on integration across the profile leads to (5.27). Therefore this condition provides no independent information about the solution and is automatically satisfied for any determination of the parameters.

Substituting the general form for F into (5.22) results in the following conditions,

$$F(\eta^+) = A \eta^+ + M(\eta^+) = 0, \quad (5.32)$$

$$F(\eta^-) = A \eta^- + M(\eta^-) = 0. \quad (5.33)$$

These expressions may be combined to give a single relation between η^+ and η^- ,

$$\bar{G}(\eta^+, \eta^-) = \eta^+ M(\eta^-) - \eta^- M(\eta^+) = 0 \quad (5.34)$$

Equation (5.34) was solved numerically on an IBM System 360 computer to determine η^+ in terms of η^- using Newton's method of successive approximation. For a specified value of η^- , the magnitude of η^+ was first estimated, then corrected using a Taylor expansion of \bar{G} about zero. This technique required the calculation of $M(\eta)$ and its first derivative which were approximated by,

$$M(\eta) = \frac{\Gamma(1/2)}{\Gamma(1/2)} \sum_{n=0}^N \frac{\Gamma(1/2+n)}{\Gamma(1/2+n)} \frac{\eta^{2n}}{2^n n!} \quad (5.35)$$

$$M' = \frac{dM}{d\eta} = \frac{\Gamma(1/2)}{\Gamma(1/2)} \sum_{n=0}^N \frac{\Gamma(1/2+n)}{\Gamma(1/2+n)} \frac{\eta^{2n-1}}{2^{n-1} (n-1)!} \quad (5.36)$$

The results of the computation were found to be independent of the order of the summation for $N > 20$ and the correction procedure was iterated until the magnitude of \bar{G} in (5.34) was less than 10^{-6} . Once the appropriate value of η^+ has been found, the other constants in the similarity solution $b'/2$, D , and A may be determined from (5.24), (5.25), and (5.32). These parameters along with η^+ are plotted for the range $-3 \leq \eta^- \leq 0$ in Figure 5-2(a), where the free constant $b'/2$ in the similarity variable has been combined with one to form

$$X_E = 1 + b'/2 \quad (5.37)$$

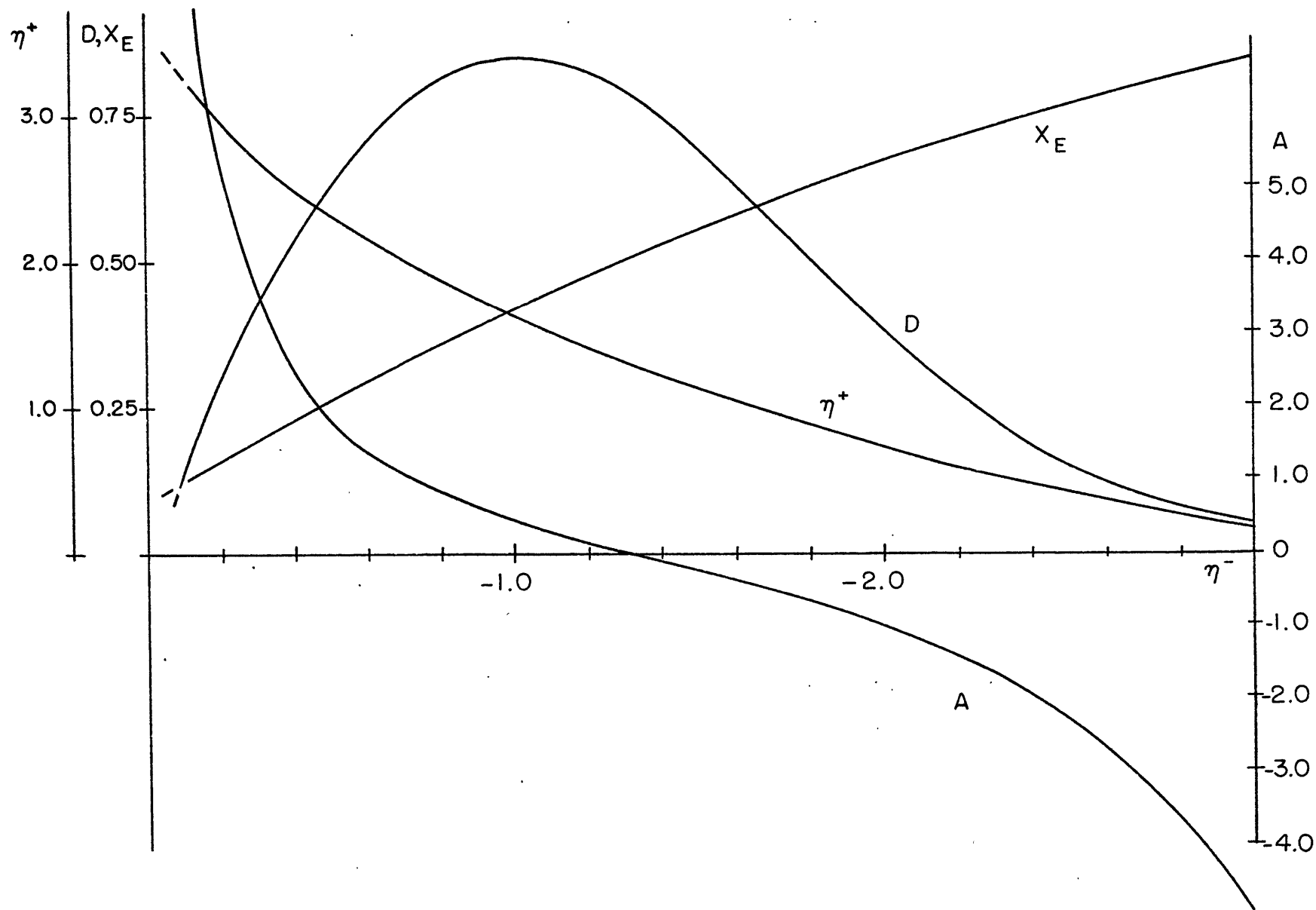


Figure 5-2(a). Free parameters in thick-layer similarity solution.

The results show that η^+ decreases as the magnitude of η^- increases whereas X_E increases monotonically. At the point where A is zero, the profile is symmetric ($\eta^+ = -\eta^- = 1.3$) while the amplitude of the similarity function D reaches a maximum near $\eta^- = -1$. Sample profiles of $F(\eta)$ for $\eta^- = -1.0, -1.3$ and -1.75 are displayed in Figure 5-2(b). Outside of this range, the shape of the profile becomes highly distorted with a steep slope on one side or the other due to the growth of the antisymmetric component.

The problem of determining the similarity solution for the lowest-order downstream flow field has now been reduced to evaluating a single constant by application of the upstream boundary condition. In principle this may be accomplished by matching asymptotically with the first term in the expansion for a single flow variable in the upstream region at a point where both expansions are valid [see Clarke (1968)]. Once the specification is complete, the velocity and transport functions may be expressed in terms of the gradients of the layer thickness variable,

$$\hat{d}\hat{x} = \frac{\delta D}{2(X_E - X)^{1/2}} [\eta F' - F], \quad (5.42)$$

and

$$d\hat{y} = \frac{D}{2^{1/2}} F'. \quad (5.43)$$

The dimensionless horizontal velocity components in the source flow variables are then given by,

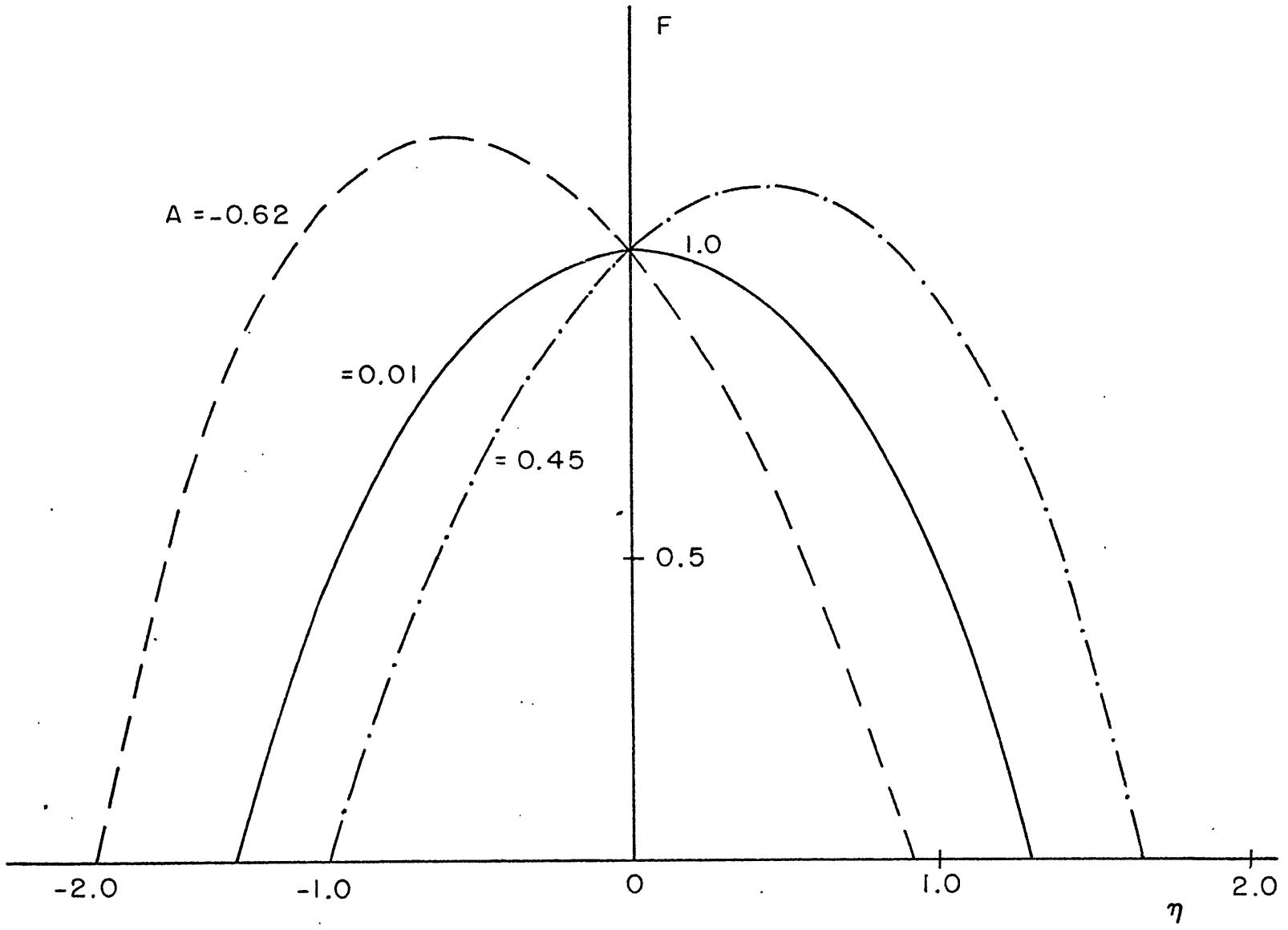


Figure 5-2(b). Sample profiles of similarity function for $\eta^{-1} = -1.0, -1.3, -1.75$.

$$\hat{u} = 1 - \hat{d}\hat{q} - [(1 - \hat{d}\hat{q}) \cos \gamma + \hat{d}\hat{x} \sin \gamma] e^{-\gamma}, \quad (5.44)$$

and

$$\hat{v} = \hat{d}\hat{x} - [\hat{d}\hat{x} \cos \gamma - (1 - \hat{d}\hat{q}) \sin \gamma] e^{-\gamma}, \quad (5.45)$$

where $\gamma = \hat{z}/2\gamma \equiv \bar{z}$. Similarly, the transport functions are expressed by (5.7) and (5.8). The corresponding dimensional forms may be obtained by inverting the flux scaling given by (3.18).

Several very interesting aspects of the downstream flow are evident from the form of the similarity solution. First of all, the thick central core of the stream is extinguished at a downstream point defined by

$$X_E = \frac{L_1 X_E}{\gamma} \quad (5.46)$$

Physically, this means that the cumulative effects of Ekman suction and leakage from the lower edge of the geostrophic layer serve to reduce its dimension to the Ekman scale across the entire flow leading to a breakdown of the thick layer approximation. Furthermore, notice that the behavior of the downstream thickness gradient, $\hat{d}\hat{x}$, is singular as X approaches X_E . This aspect of the solution is anticipated since the multiple-scale analysis neglects the highest-order downstream derivative in equation (5.2). The implication of this result is that the downstream derivatives become important near the extinction point, $X = X_E$, where the transition contours meet.

Before proceeding to a description of the laboratory experiment,

the method of characteristics will be employed to obtain simple results for the viscous flow near the upslope edge streamline which gives insight into the upper edge dynamics and provides justification for the constraints applied at the upper transition contour.

V.1.2 Method of Characteristics for Flow at the Upper Edge

Because of the existence of a distinct edge streamline along the upslope boundary of the flow in region I (see Figure 5-1), a more restrictive approximation may be applied to the layer-thickness equation (3.65) derived for the weak rotation under the Ekman scaling. If the second derivatives of \bar{d} are well-behaved at the upper extremity of the edge regime, then the vanishing of the layer thickness implies that an approximate balance exists among the first derivatives, i.e.,

$$\bar{d}_x^2 + \bar{d}_y^2 = \bar{d}_y \quad \text{for } \bar{d} \rightarrow 0. \quad (5.47)$$

The standard analysis of this nonlinear first-order partial differential equation by the method of characteristics is presented in Appendix C. The initial data for the computation are specified on the source profile along $\bar{x} = 0$, that is,

$$\begin{aligned} \xi = \bar{x} = 0, \\ \Delta(0, \bar{y}; t) = \bar{y} - \bar{y}_e(0) = t, \\ \bar{d}(0, \bar{y}) = u_0(t), \\ \bar{d}_x(0, \bar{y}) = p_0(t), \\ \text{and} \\ \bar{d}_y(0, \bar{y}) = q_0(t), \end{aligned} \quad (5.48)$$

where $t = \bar{y} - \bar{y}_e(0)$ is the parameter for the initial data, (ξ, Δ) defines the trajectory in the (\bar{x}, \bar{y}) plane of the characteristic emanating from the point t on the initial line, and u_0 , p_0 , and q_0 are the initial values of the thickness variable and its first derivatives. For physical and mathematical reasons, the cross-stream thickness gradient on the source profile, q_0 , must be bounded from above and below, i.e.,

$$0 < q_0 < 1. \quad (5.49)$$

With this constraint, the solutions along characteristics may be inverted to yield expressions for the characteristic paths and the layer thickness function in terms of the geometric coordinates (\bar{x}, \bar{y}) and the initial data,

$$\bar{y}(\bar{x}, t) - \bar{y}_e(0) = \frac{2q_0 - 1}{2\sqrt{q_0(1-q_0)}} \bar{x} + t, \quad (5.50)$$

and

$$\bar{d}(\bar{x}, \bar{y}; t) = \frac{q_0}{2\sqrt{q_0(1-q_0)}} \bar{x} + u_0(t). \quad (5.51)$$

The restrictions on the magnitude of q_0 cause the value of \bar{d} to increase in the downstream direction, so that ultimately the assumption of vanishing thickness will be violated and second derivatives must be included. Furthermore, the characteristics issuing from the

initial profile tilt downslope since

$$\frac{d\bar{y}}{d\bar{x}} = \frac{2q_0 - 1}{2\sqrt{q_0(1-q_0)}} > 0. \quad (5.52)$$

This result supports the contention that the dense fluid cannot move upslope in the viscous edge regime. To obtain additional information about the solution requires a more detailed specification of the source profile. In particular, it is reasonable to assume that for a balanced inlet profile, the thickness gradient decreases in the cross-stream direction so that the interface tends to parallel the bottom. This implies that the second derivative of \bar{d} with respect to \bar{y} is less than zero, i.e.,

$$\frac{dq_0}{d\bar{y}} = \bar{d}_{\bar{y}\bar{y}}(0, \bar{y}) < 0.$$

For steadily decreasing q_0 , crossing characteristics are anticipated because the characteristics nearest the edge pitch downslope most steeply. This condition leads to the development of a front at the upper edge.

The envelope of characteristics which forms the front is defined by the locus of points that satisfy the trajectory equation (5.50) and the condition, $\frac{d\Delta}{dt} = 0$, simultaneously. Thus the coordinates of the envelope (ξ_c, Δ_c) are obtained parametrically in terms of the initial data,

$$\xi_c = - \frac{4(q_0 - q_0^2)^{3/2}}{q_0'} , \quad (5.53)$$

and

$$\Delta_c = \frac{2q_0}{q_0'} (2q_0^2 - 3q_0 + 1) + t, \quad (5.54)$$

where

$$q_0' = \frac{dq_0}{dt} = \bar{d} \bar{y} \bar{y} (0, \bar{y}; t).$$

Note that for $0 < q_0 < 1$ and $q_0' < 0$, the intersection of characteristics occurs downstream from the initial line ($\xi_c > 0$) and also downslope from the origin of the characteristic since

$$\Delta_c - t = \frac{2q_0}{q_0'} (2q_0 - 1)(q_0 - 1) > 0$$

Mathematically, the envelope consists of those points where the inversion from characteristic to geometric coordinates first becomes multi-valued. Beyond the intersection points, the method of characteristics breaks down as the front develops.

In the laboratory experiments described in the following section a detailed knowledge of the source profile was unavailable, so that quantitative comparison with characteristic results was precluded. However, confirmation was sought for the qualitative aspects of the approximate solution, particularly the development of the front, in addition to the salient features of the similarity solution, i.e., the Ekman flux drainage leading to extinction of the geostrophic layer in the downstream.

V.2 Laboratory Experiments for the Strong Rotation Limit

V.2.1 Design of the Experiment and Apparatus

The strong rotation experiments were performed in the laboratory of Dr. W. Malkus at M.I.T. on a turntable designed and built by Drs. K. Saunders and R.C. Beardsley (1972). A view of the apparatus for the experiment is given in Figure 5-3(a). The table rides on an air bearing and is driven with a piece of magnetic tape by a small hysteresis synchronous motor. The 42-inch diameter basin consists of a sheet of Masonite fastened to the perimeter of a circular piece of plywood with a piece of 1/4-inch plate glass set inside, to form a flat bottom. The tank is supported by three leveling screws above another piece of plywood which in turn is raised from the table on aluminum posts. The circulation system for the source flow is shown in Figure 5-3(b). A reservoir with a capacity of approximately two liters is mounted on the rotation axis and feeds dense fluid down through a solenoid valve into the constant head device below. From there the descending fluid is carried by a section of 3/8-inch Tygon tubing to the source point on an inverted plexiglas cone, which is glued to the bottom of the basin. The fluid is collected at the base of the cone and returned to the reservoir by two Cole Parmer Masterflex peristaltic pumps. The suction is distributed evenly around the outer rim of the basin bottom by pumping through the walls of a plexiglas tube which has been drilled with holes of varying dimension depending on the length of the travel path to the pump. This was done to avoid drawing in the light upper fluid through the thin layer of dense fluid at the bottom of the tank.

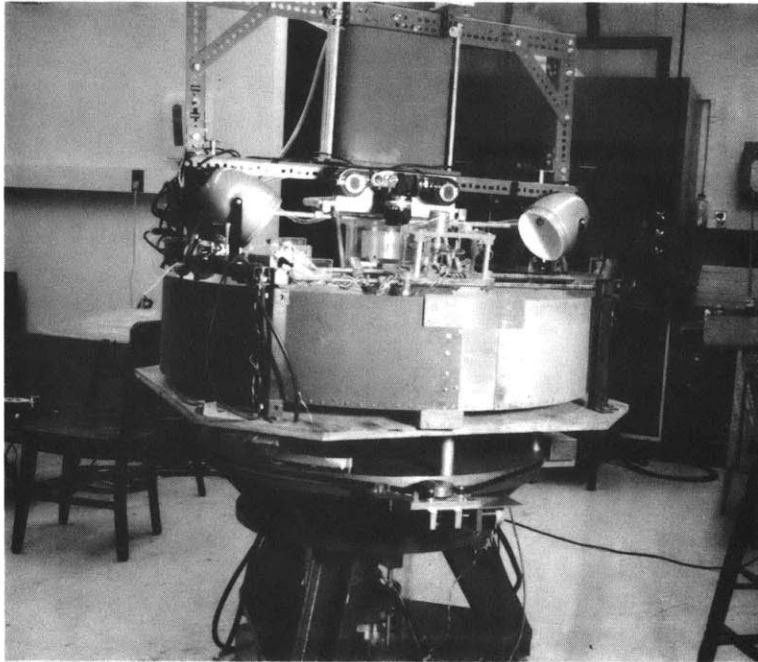


Figure 5-3(a). View of apparatus for strong rotation experiments.

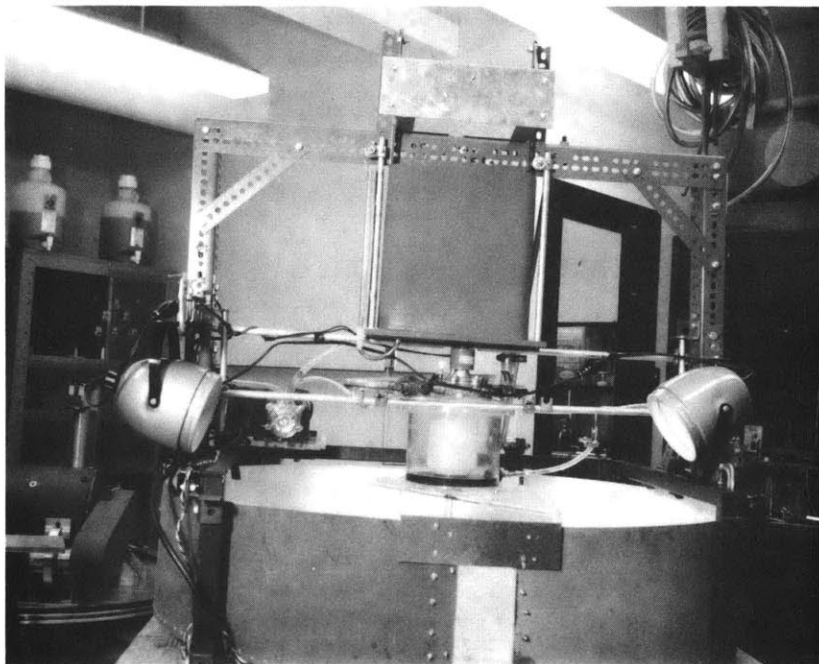


Figure 5-3(b). Circulation system showing reservoir, solenoid valve, constant-head device, and peristaltic pump.

The design of an experiment whose physics adequately matched that of the theoretical model proved to be very difficult. First of all, to achieve the right parameter range ($\epsilon \ll 1$, $E \ll 1$), it is necessary to reduce gravity in a two-layer system with a small density contrast. The presence of a viscous upper fluid leads to a stress, which is absent in the theory, at the interface between the dense bottom current and the resting layer above. An extensive search was carried out to find suitable fluids for the two layers. Immiscible fluids were found to be unsatisfactory because of the influence of interfacial tension which controlled the dynamics of the edge regions and destroyed the viscous-rotational balance there. Specifically, in an experiment using a mixture of methanol and water over Nujol, a heavy mineral oil, the source flow seemed to contract in the downstream and showed no evidence of draining by the Ekman flux mechanism. A measurement of the interfacial tension by the drop-weight method [Davies and Rideal (1963), p. 42] showed that the interfacial tension length scale $(\sigma_i / \rho \hat{g}_r)^{1/2}$ exceeded the Ekman scale $(2\nu t / \hat{f})^{1/2}$ for this case. Therefore, the dominance of interfacial forces is anticipated in the edge regime. Moreover, attempts to blend different fluids to lower their interfacial tension as described by Hart (1972) lead to a splintering of the stream into thin veins. It was concluded that miscible fluids were needed if viscous mechanisms were to be observed in the thin edge regions. However, care had to be exercised to maintain a laminar flow and avoid unwanted mixing. After further study, the upper and lower fluids were chosen to be salt water and a mixture of glycerine and water, respec-

tively. The high viscosity of glycerine means that stresses at the interface produce relatively weak shearing within the lower fluid. Moreover, the viscosity of the glycerine-water solution could be easily modified by changing its composition, and the density contrast could be adjusted by varying the salt content of the upper layer.

Another problem encountered was the strong centrifugal potential field which accompanied the rapid rotation rates required in the experiments. To account for this effect, the conical bottom slope was machined with a parabolic correction in the radial direction, such that

$$Z_e = H - sR_c + \frac{\Omega^2 R_c^2}{2g},$$

where Z_e is the height of the cone surface above the glass bottom and R_c is the radial distance from the rotation axis. In this configuration, the potential surfaces due to gravity g and rotation intersect the cone surface at a constant angle so that the body force component along the cone is invariant. The equivalence of the governing equations for the laboratory flow and those derived in Chapter III for the Ekman layer model may be easily established if the upper layer is motionless and the curvatures of the cone surface are small. Notice that choice of this form for the bottom shape fixes the rotation rate for all experiments ($\Omega = 2.21 \text{ rad/sec}$).

Finally, the laboratory flows show a strong tendency to be time dependent. This was first noticed in some two-dimensional preliminary experiments aimed at focusing on the Ekman drainage mechanism. A ring of dense fluid, initially contained behind a plastic barrier, was re-

leased and allowed to adjust to a natural state. Using a stability diagram derived experimentally by Saunders (1973) for the case of a flat bottom, an attempt was made to avoid baroclinic instability in the ring by fixing the Taylor and internal Froude numbers at stable values. However, a steady azimuthal flow was never attained in the adjusted state. Instead, the ring would break into a distinct number of vortices which propagated around the cone. With reference to Saunders' results, it is apparent that the slope exerts a destabilizing influence. In spite of the unsteadiness, a thin layer was observed extending down the slope from the base of the larger vortices as they moved. In general, though, the flow was too confused to discern a consistent pattern. The temporal variability was not confined to the ring experiments. Attempts to produce steady flow fields in the initial series of source flow experiments were not completely successful and consequently the results show some interesting transient features.

V.2.2 Procedures for the Source Flow Experiments

At the beginning of each source flow experiment, the value of Q was determined by adjusting the flow rate from the reservoir such that the constant-head device was brimmed but not overflowing, then measuring the volume of samples collected in a certain interval of time. The viscosity was also measured with a Cannon-Fenske viscometer. Next the flow was cut off by closing the solenoid valve, the dense fluid was pumped out of the basin, and the system was spun up. When the relative motion in the tank had decayed sufficiently, the valve was opened again

and the source flow was established. This usually occurred within 10 - 20 rotation periods. After another 10 periods, the measurements of the flow were made. This procedure was followed in order to avoid the strong mixing that would occur if the two fluids were in contact during spinup. All measurements were completed before any of the dense fluid was pumped back into the reservoir so that the properties of the supply fluid would not be altered. At the end of the measurements, the solenoid valve was closed and the dense fluid returned to the reservoir before spinning down.

In the small number of exploratory experiments performed so far, two types of measurements were made. The first was simply an overall view of the downstream region obtained from a Polaroid photograph taken from a point on the frame above the tank. For visualization purposes, the dense fluid was dyed with blue ink and the conical bottom surface was scribed with radial and azimuthal lines at 2-inch and 15-degree intervals.

The second set of measurements was more detailed and made use of a motor-driven micrometer similar to that shown in Figure 4-1(d). A probe stem shown in Figure 5-4(a) was attached to the micrometer arm and lowered in a direction normal to the local bottom slope. The stem was constructed of stainless steel tubing and carried two types of probes. Conductivity probes sensed the interface between the glycerine solution and the salt water, while small tubes were used to inject dyed glycerine solution into the flow for the purpose of measuring velocity. The five conductivity probes are mounted at the corners of the frame

and in the center. Each consists of platinum wire (.014") soldered to a lead wire and encased in a glass tube which is sealed with epoxy. The tip of the probe has been ground off to expose the platinum so that the current path through the fluid is from the probe tip to the central member of the stem. When the probe entered the glycerine, the resistance changed radically and the position of the interface was recorded. The diagram for the probe circuit is given in Figure 5-5. Velocity measurements were made by injecting dyed glycerine solution into the flowing layer with a motor-driven syringe shown in Figure 5-4(b). Care was taken to make the dyed fluid neutrally buoyant in the glycerine solution used for the source. The image of the dyed fluid was deflected by a series of mirrors to the lens of a Nikon camera which took a rapid sequence of pictures as the dye streak lengthened. The displacement of the tip of the streak between frames could be used to estimate the local velocity at a known depth within the layer. The height of each probe except the center one was adjustable due to a slip fit between the glass tube and its plastic carrier. Therefore the distance of each probe above the solid surface could be gauged by lowering each probe to touch the cone surface at the same point that the center probe hit.

The flow parameters for the exploratory experiments to be discussed below are given in Table VI. The source point for all experiments was located at a distance of $R_c = 9.1 \text{ inch} = 23.1 \text{ cm}$ from the axis of rotation.

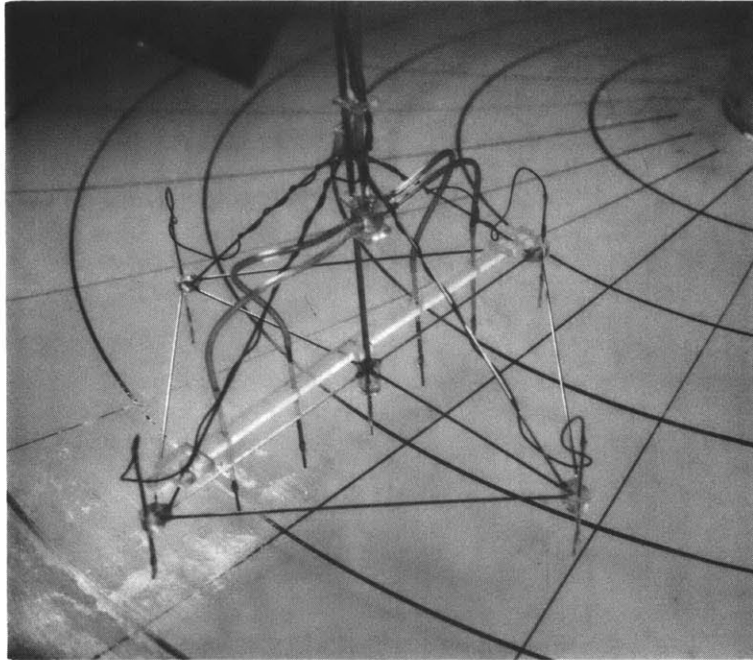


Figure 5-4(a). Probe stem carrying conductivity probes and injection tubes for dyed fluid.

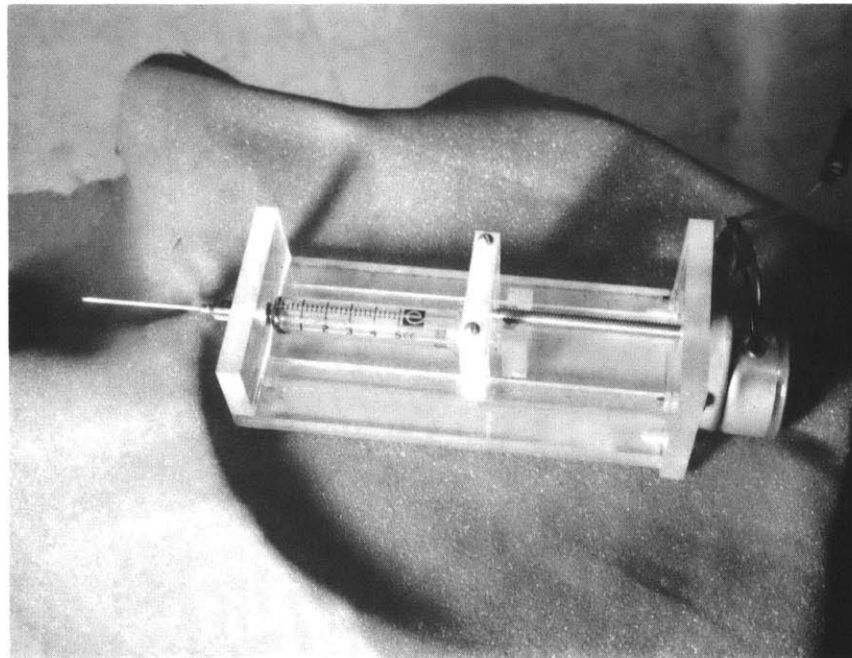


Figure 5-4(b). Motor-driven syringe.

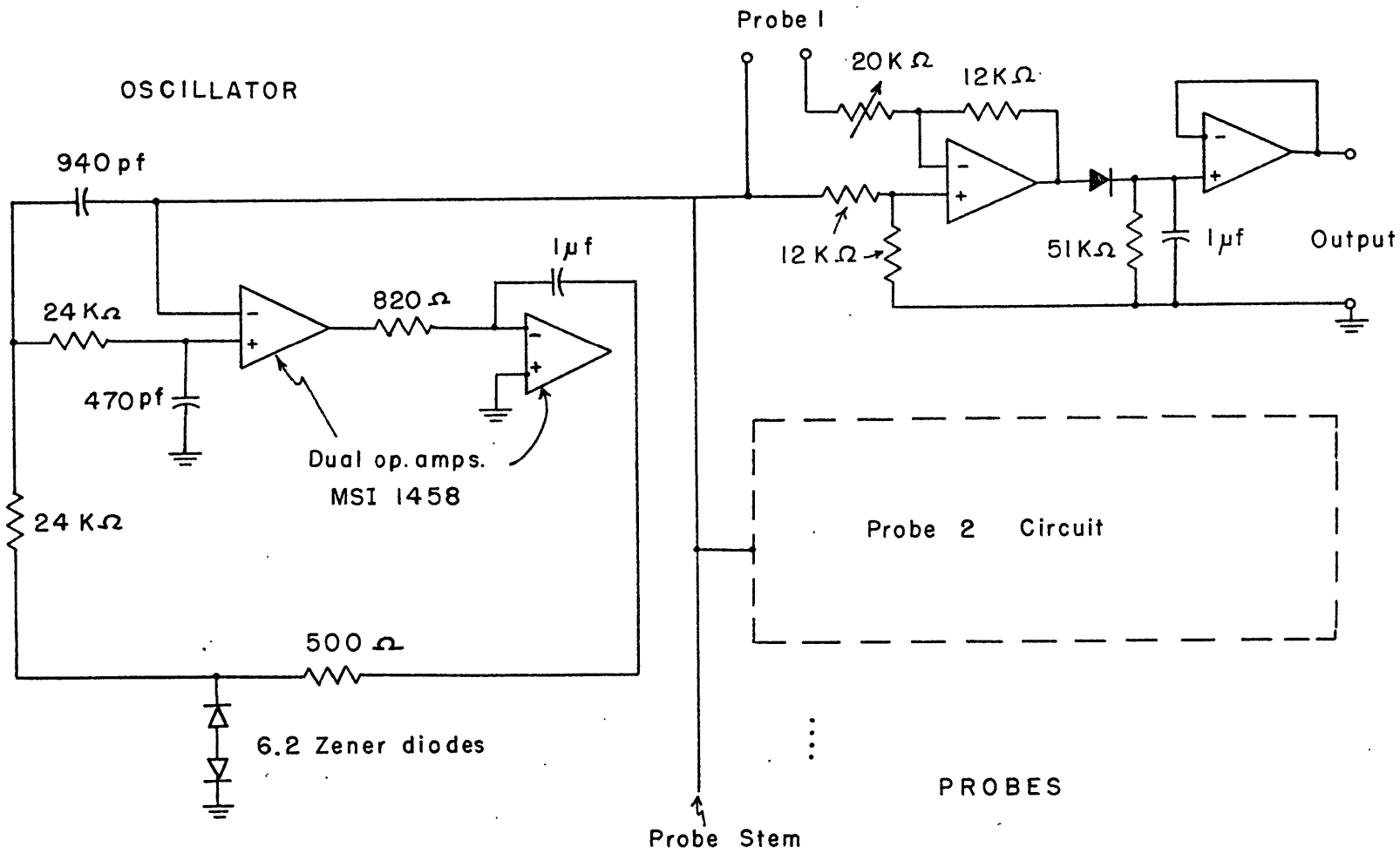


Figure 5-5. Circuit diagram for conductivity probe.

Experiment	Q (cm ³ /sec)	v _t (cm ² /sec)	\hat{g}_r (cm/sec ²)	\hat{f} (/sec)	s	L (cm)	γ
7-30.2	10.0 ± 0.6	0.12 ± .01	16.4 ± 0.8	4.29	0.25	3.2	0.073
7-30.3	9.9 ± 0.4	0.10 ± .01	14.0 ± 0.8	4.29	0.25	3.5	0.062
7-20.1	9.7 ± 0.3	0.23 ± .01	4.1 ± 0.8	4.29	0.25	13.0	0.050
7-21.2	9.6 ± 0.3	0.19 ± .01	6.60 ± 0.8	4.29	0.25	10.1	0.058
7-21.3	10.1 ± 0.5	0.18 ± .01	17.3 ± 0.8	4.29	0.25	6.4	0.090

TABLE VI. Parameters for the Source Flow Experiments

V.2.3 Experimental Results

The qualitative aspects of the source flow are apparent from the photographs in Figure 5-6. In these pictures, the source appears in the upper righthand corner and the base of the cone is at the bottom. One striking feature of these results is the appearance of a distinct upper edge streamline in accordance with the physical and mathematical arguments presented in the last section. On the other hand, there is no lower edge streamline in the field of view and the entire slope below the upper edge is darkened by the presence of dyed fluid. In these experiments, the boundary of the glycerine solution below the source was observed to lie roughly along a radial line upstream from the mouth of the source. The dense fluid in this region was supplied by a counter flow near the upper edge of the current which feeds fluid back along the side of the tube and then down the slope. The flow at this boundary and near the base of the slope was light in color indicating the presence of a thin layer.

Layer thickness and velocity measurements were made in experiments 7-20.1, 7-21.2, and 7-21.3. The thickness results showed the presence of low frequency waves on the layer surface. The amplitude of the waves varied from almost zero to roughly 40% of the total layer depth in the thickest regions of the flow as determined by the descent of the probe from the point where the first crest touched to where it remained submerged in the glycerine. In spite of the movement of the layer surface, the interface remained sharp indicating that there was little mixing associated with the transient flow. The time interval Δt between

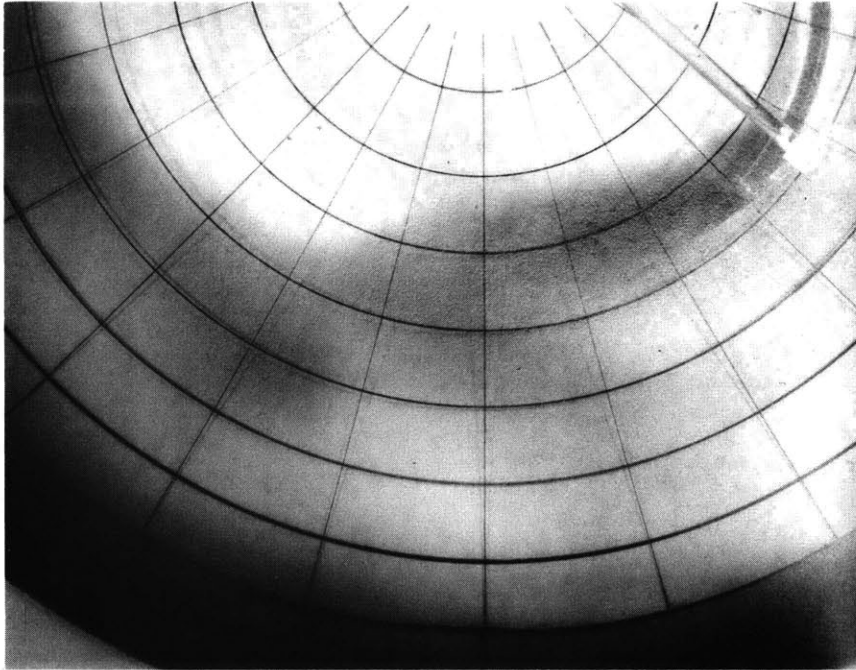


Figure 5-6(a). Source flow for Experiment 7-30.2.

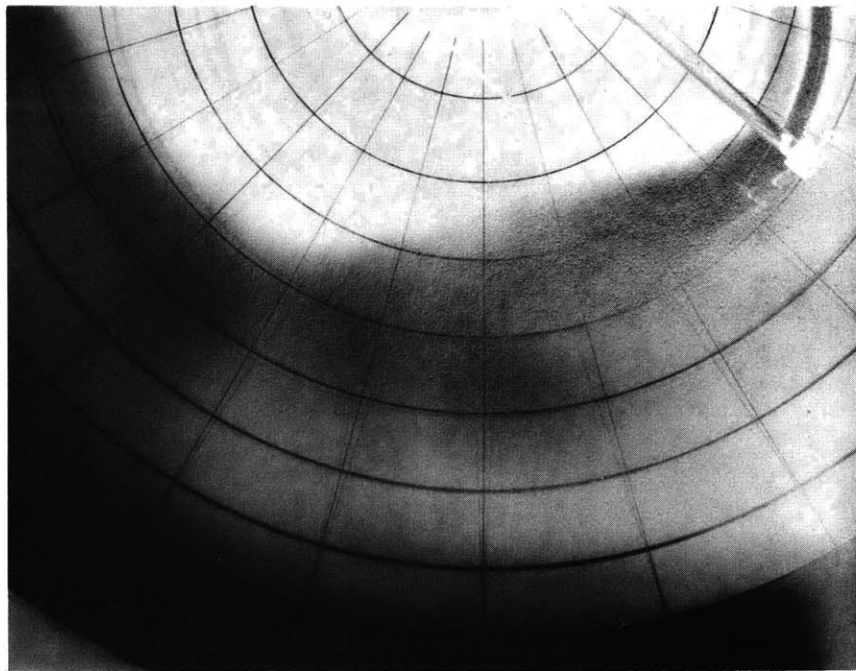


Figure 5-6(b). Source flow for Experiment 7-30.3.

waves was quite stable at a single probe, but the period was observed to increase sharply with downstream distance. A plot of the variation of Δt , normalized by the rotation period, versus dimensionless downstream distance \hat{x} is given in Figure 5-7. The error brackets on certain points indicate the variation in Δt over several waves, while the absence of these bounds on the other points implies that only a single estimate was available. The photographs for the velocity measurements were taken at a constant rate of two frames per second but the changes in the length of the dye streak in successive frames varied by as much as 50%, indicating that the velocities are also irregular. In general, the path of the streak tilted downslope and measurements at different levels indicated that the magnitude of the velocity diminished toward the solid surface. However, due to the variability, no consistent pattern could be discerned, so these data will not be presented.

An attempt was made to use the qualitative data in Figure 5-6 to determine the upstream boundary condition for use in the similarity solution. In experiment 7-30.3, the upper edge begins to move down the slope at a point roughly 30° downstream from the source and crosses the downstream axis defined by the source position at 75° approximately. If this point is taken as the extinction point for the geostrophic layer, then the corresponding value of X_E is computed to be 0.26, which implies that the upper edge lies at $\eta^- = -0.5$ according to Figure 5-2(a). But if the value of η^- is calculated using this value of X_E at the point where the edge streamline begins its descent, is $\eta^- = -2.3$, which corresponds to an extinction point much further downstream. Several

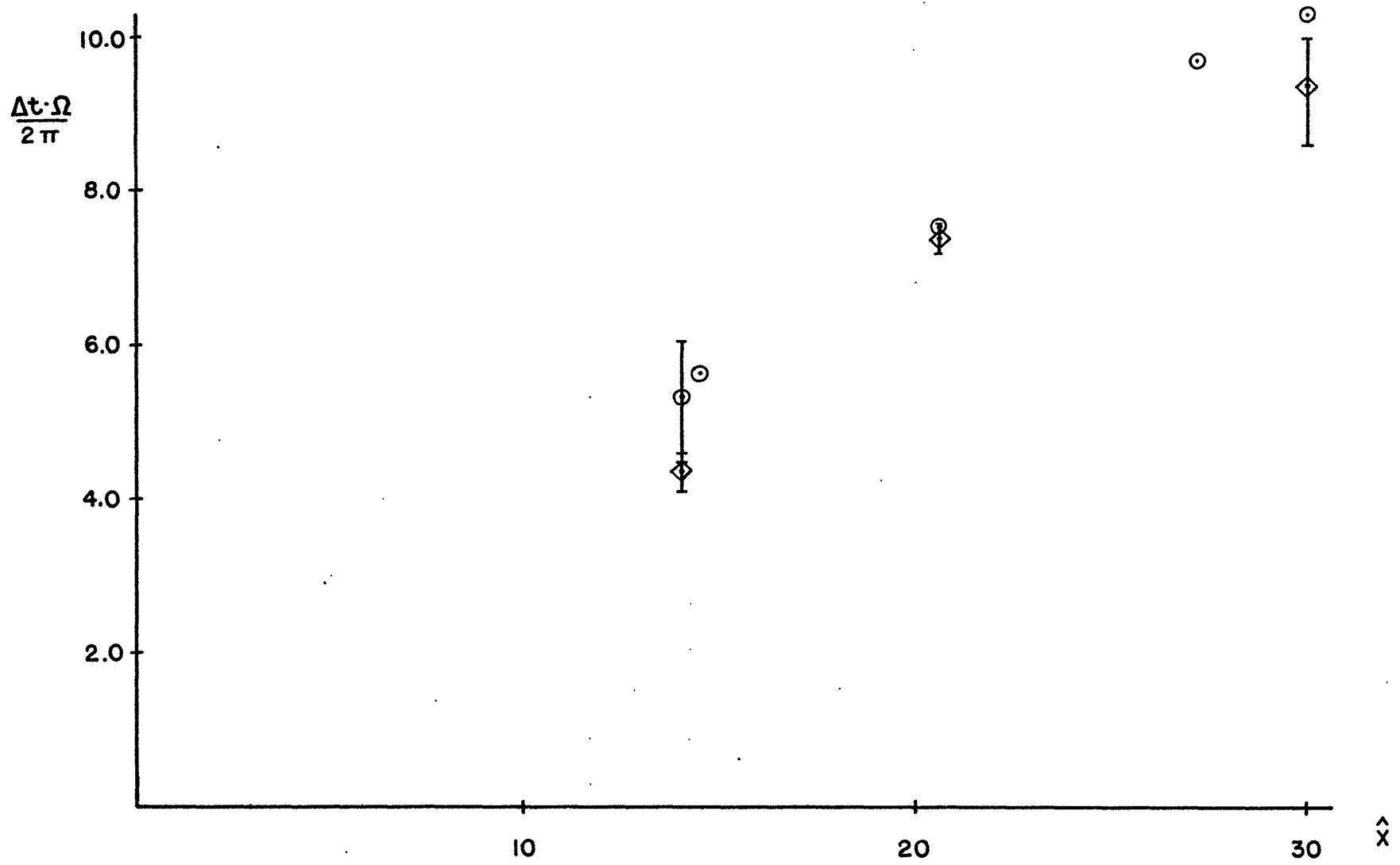


Figure 5-7. Period of interfacial waves normalized by rotation period. \odot Experiment 7-21.2, \diamond Experiment 7-21.3.

reasons for this discrepancy may be offered. First of all, the stress at the interface exerts a drag on the moving layer which decelerates the flow and may cause it to move slightly downslope because of the reduction in the Coriolis acceleration. If this were true, then the point at which the upper edge crosses the downstream axis would not represent the true extinction point for the thick layer. Moreover, the time dependent processes may influence the shape of the edge streamline such that the apparent descent of the upper edge is part of a weak meander pattern in the flow.

Finally, an effort was made to analyze the thickness data in terms of dimensionless variables. For each measurement, an average value of the layer thickness \hat{d} was defined by normalizing the mean height of the wavy interface with $sL = \left(\frac{\hat{Q}}{q_r}\right)^{1/2}$. These results are plotted against the dimensionless coordinates (X, \hat{y}) in Figure 5-8. In the hope of obtaining information experimentally about the symmetry properties of the downstream thickness profile, the theoretical depth contours for the symmetric profile ($A = 0.01$, $\psi^- = -1.3$) in Figure 5-2(b) are superposed on the data. In view of the uncertainty in the thickness measurement, the magnitude and general trend of the data are in reasonable agreement with the theoretical distribution. However, due to poor coverage in the downstream region and the ambiguities involved with the waves, no statement can be made about the character of the cross stream profile.

It is clear from these results that more definitive measurements are required in order to analyze the detailed properties of the down-

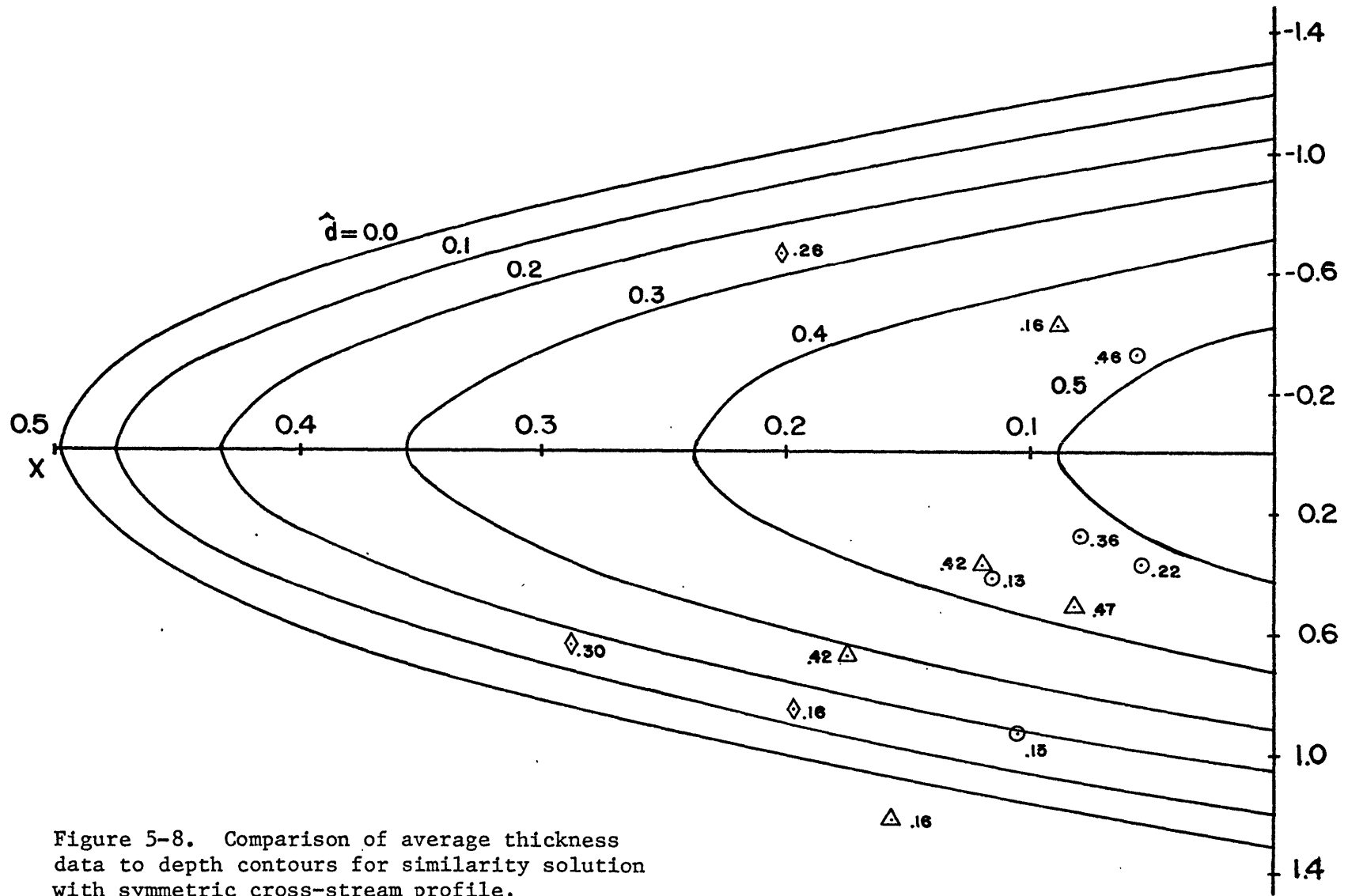


Figure 5-8. Comparison of average thickness data to depth contours for similarity solution with symmetric cross-stream profile.

○ Experiment 7-20.1, △ Experiment 7-21.2, ◇ Experiment 7-21.3.

stream flow. Nevertheless, these pilot experiments are of value in confirming some basic features of the Ekman layer model such as the flux of dense fluid down the slope in a thin layer below the main current. Moreover, the results are useful in demonstrating the feasibility of the experimental techniques and in defining some of the problem areas in both the theoretical and laboratory models. In the next series of experiments, care must be taken to produce a steady flow for comparison with theory. In reviewing the experimental results, it was noticed that the average value of the exit velocity at the mouth of the source exceeded a typical geostrophic velocity scale $U = \frac{g_r S}{f}$ by close to an order of magnitude in most cases. In the streamtube model of Chapter II, such an imbalance leads to the production of steady topographic meanders, while in the laboratory flow it is believed to induce the low-frequency waves observed in the experiment. Once a steady flow is achieved, extensive thickness and velocity measurements must be made to encompass the entire flow field for the thick layer. In this way, the upstream boundary condition for the similarity solution may be determined experimentally and the resulting theoretical predictions could then be compared to the downstream measurements. Moreover, it is of interest to investigate the structure of the flow in the lower edge regime and near the extinction point to determine layer characteristics where the effects of viscous and rotational forces are comparable. Finally, some thought should be devoted to a mathematical treatment of the flow in the source region for the purpose of defining the upstream boundary condition analytically. If this can be accomplished then the

need to rely on the accuracy of the experimental measurements is eliminated since the theoretical solution is completely specified.

V.3 Conclusion

In closing, it is important to attempt some comparison between the theoretical solution for the strong rotation Ekman layer model and the observational data presented in Chapter II. The streamtube model results provide an estimate of the strength of the frictional forces in the outflow currents through the value of the empirical drag coefficient K derived from the observations. Moreover, the Norwegian Overflow data would be best suited for the comparison since the entrainment and ambient stratification exert a weaker influence on this current than in the case of the Mediterranean Outflow. Using the optimum value of K for the Norwegian Overflow, it is possible to estimate a value for the turbulent eddy viscosity on an order-of-magnitude basis. If the average velocity gradient in the outflow current is approximated by the ratio of the geostrophic velocity scale to the mean layer depth, then equating the resultant viscous stress $\rho \nu_t \bar{V}/h$ at the lower boundary to the cross-stream average stress in the streamtube model $\rho K \bar{V}^2/\ell$ gives $\nu_t = K \bar{V} h/\ell$, where h is the characteristic layer depth and ℓ is the cross-stream scale. For the quantities listed in Table III, the value of the turbulent eddy viscosity is $2.4 \times 10^4 \text{ cm}^2/\text{sec}$, which is in sharp contrast to the value of $4 \text{ cm}^2/\text{sec}$ obtained in Chapter III by Faller's criterion. The former value is undoubtedly high due to an underestimate of the shear at the base of the outflow by use of the total layer depth, whereas the latter value is small because of its dependence on the weak geostrophic velocity

scale. Adopting a median value of $\nu_t = 100 \text{ cm}^2/\text{sec}$ for the calculation of the source flow Ekman number leads to

$$\gamma = (E/2)^{1/2} = 0.045,$$

whereas the appropriate source flow length scale is given by

$$L_1 = \left(\frac{\hat{f} Q}{\hat{q}_r s^2} \right)^{1/2} = 32 \text{ km}.$$

For a representative value of the extinction point $X_E = 0.5$, the thick geostrophic core of the Norwegian Overflow would be extinguished at a point 360 km. downstream from the Denmark Strait where the stream would begin to shift significantly downslope by the action of viscosity. Despite the uncertainty in ν_t , this hypothesis is not unreasonable in view of the observed descent of the Norwegian Sea water along the Greenland continental slope as demonstrated in Figure 2-3. Specifically, the traces of outflow water which are observed high on the slope at Section III are not present at that level in Section IV or V indicating that the contour-following tendency of the geostrophic current has been altered. Notice that the proposed mechanism for draining of the geostrophic layer by the Ekman flux leads to a different picture of the flow near the source from that offered by the streamtube model. According to the detailed model, the rotational forces are strongest in the upstream region where the layer is thick and therefore a major portion of the stream tends to run along the slope. In contrast, the streamtube model predicts that the maximum pitch of the flow axis occurs at the

source followed by a gradual turning along the slope due to entrainment. The qualitative aspects of cross-sectional data for the Norwegian Overflow suggest that the Ekman layer model provides a more accurate description of the dynamical balance in this deep boundary current, but a more comprehensive survey of the flow in that vicinity is needed to test this conclusion.

Finally, to emphasize the ongoing nature of this investigation, it is fitting to close the present phase of analysis with a speculative note concerning the low frequency waves observed in the strong rotation experiments. In the data collected by Worthington (1969) during his attempt to measure the overflow through the Denmark Strait, a distinct oscillation with a period of approximately four days is observed in the velocity and temperature records. This time scale is not inconsistent with the measured oscillation of four rotation periods at the farthest upstream points in the source flow experiments. However, the explanation of this coincidence awaits further study.

APPENDIX A

Streamtube Model Equations

The integral streamtube equations may be derived in a number of equivalent ways. Here a formal approach will be taken, and the derivation will proceed from the differential equations of motion in order to emphasize the detailed assumptions made about nature of the flow.

In the geometry of Figure 2-1, the steady equations governing the mean flow of a turbulent, incompressible, linearly-stratified, rotating fluid are:

$$\nabla \cdot \underline{u} = 0, \quad (\text{A.1})$$

$$\nabla \cdot (\rho \underline{u}) = 0, \quad (\text{A.2})$$

$$\rho(\underline{u} \cdot \nabla \underline{u} + \underline{f} \times \underline{u}) = -\nabla P + \frac{\partial \tau_{ij}}{\partial x_j} + \rho \underline{g}, \quad (\text{A.3})$$

where

$$\rho = \rho_e + \Delta \rho, \quad \rho_e = \rho_0 [1 + T \cos \alpha (s_y - z)], \quad (\text{A.4})$$

and

$$\underline{f} = 2 \underline{\Omega}.$$

The stress tensor, τ_{ij} ($i, j = x, y, z$), includes both laminar and turbulent Reynolds stresses, i.e., $\tau_{xy} = \mu \frac{\partial u}{\partial y} - \rho \overline{u'v'}$, where μ is the mole-

cular viscosity coefficient and ' denotes a turbulent fluctuation.

Next, a hydrostatic component is removed from the pressure field by writing,

$$P(x, y, z) = P_w(y, z) + p(x, y, z) \quad , \quad (A.5)$$

where $P_w(y, z) = \rho_0 \hat{g} \left[(s_y - z) + \frac{\hat{T}}{2} (s_y - z)^2 \right]$, $\hat{T} = T \cos \alpha$,

and $p(x, y, z)$ is the reduced pressure.

The following assumptions are now introduced:

- (i) The bottom slope is assumed small ($s = \tan \alpha \ll 1$).
- (ii) Furthermore, in line with observed characteristics of overflow currents, assume that the fields of excess density and turbulence are concentrated near the bottom in a thin layer, which implies that,
- (iii) within the stress and pressure fields, variations normal to the bottom exceed those in tangential directions ($\frac{\partial}{\partial z} \gg \frac{\partial}{\partial x}, \frac{\partial}{\partial y}$), and
- (iv) vertical velocities and stresses are small so that the reduced pressure field is nearly hydrostatic.

Under these constraints, the component form of the equations in the bottom fixed coordinates is:

$$u_x + v_y + w_z = 0 \quad (A.6)$$

$$(\rho u)_x + (\rho v)_y + (\rho w)_z = 0 \quad (\text{A.7})$$

$$\rho [u u_x + v u_y + w u_z - \hat{f} v] = -p_x + \frac{\partial T_{xz}}{\partial z}, \quad (\text{A.8})$$

$$\rho [u v_x + v v_y + w v_z + \hat{f} u] = -p_y + \frac{\partial T_{yz}}{\partial z} + S \hat{g} \Delta \rho, \quad (\text{A.9})$$

and
$$p_z = -\hat{g} \Delta \rho, \quad (\text{A.10})$$

where
$$\Delta \rho = \rho - \rho_e, \quad \rho_e(y, z) = \rho_0 [1 + \hat{T}(sy - z)] \quad (\text{A.11})$$

and
$$\hat{f} = 2\Omega \cos \alpha, \quad \hat{g} = g \cos \alpha, \quad \text{and} \quad \hat{T} = T \cos \alpha \quad (\text{A.12})$$

The equations are next transformed to streamwise coordinates (ξ, η) . (See Figure 2-1.) The transformation associates every point (x, y) in the neighborhood of the current with a distance from the axis, η , and a corresponding point on the axis, ξ , where ξ is the distance from the source measured along the axis. Since the flow is steady, the value of ξ defines a unique point in the fixed coordinates $[X(\xi), Y(\xi)]$ and a pitch angle, $\beta(\xi)$, between the stream- and x-axes. Hence the equations for the path of the stream are given by:

$$\frac{dX}{d\xi} = \cos \beta \quad (\text{A.13})$$

and
$$\frac{dY}{d\xi} = \sin \beta. \quad (\text{A.14})$$

Analytically, the coordinate transformation has the form,

$$x = X(\xi) - \eta \sin \beta(\xi), \quad (\text{A.15})$$

$$y = Y(\xi) + \eta \cos \beta(\xi), \quad (\text{A.16})$$

and the tangential velocity components,

$$u(\xi, \eta, z) = u \cos \beta + v \sin \beta, \quad (\text{A.17})$$

and
$$v(\xi, \eta, z) = -u \sin \beta + v \cos \beta, \quad (\text{A.18})$$

represent a local rotation of the coordinate axes through the pitch angle, β .

The form of the equations in streamwise coordinates contains additional terms relating to the curvature of the stream axis:

$$\frac{1}{h} \mu_{\xi} + v_{\eta} + w_z - \frac{k}{h} v = 0, \quad (\text{A.19})$$

$$\frac{1}{h} (\rho \mu)_{\xi} + (\rho v)_{\eta} + (\rho w)_z - \frac{k}{h} \rho v = 0, \quad (\text{A.20})$$

$$\rho \left[\frac{1}{h} \mu \mu_{\xi} + v \mu_{\eta} + w \mu_z - \frac{k}{h} v \mu - \hat{f} v \right] = -\frac{1}{h} P_{\xi} + \frac{\partial T_{\xi z}}{\partial z} + s \hat{g} \Delta \rho \sin \beta, \quad (\text{A.21})$$

$$\rho \left[\frac{1}{h} \mu v_{\xi} + v v_{\eta} + w v_z + \frac{k}{h} \mu^2 + \hat{f} \mu \right] = -P_{\eta} + \frac{\partial T_{\eta z}}{\partial z} + s \hat{g} \Delta \rho \cos \beta, \quad (\text{A.22})$$

and
$$P_z = -\hat{g} \Delta \rho, \quad (\text{A.23})$$

where $h(\xi, \eta) = (1 - \eta k)$ and $k(\xi) = \frac{d\beta}{d\xi}$ is the curvature of the stream axis. (A.24)

The stress components are given by,

$$\begin{aligned} \tau_{\xi z}(\xi, \eta, z) &= \cos \beta \tau_{xz} + \sin \beta \tau_{yz}, \quad \text{and} \\ \tau_{\eta z}(\xi, \eta, z) &= -\sin \beta \tau_{xz} + \cos \beta \tau_{yz}, \end{aligned} \quad (\text{A.25})$$

and

$$\Delta \rho(\xi, \eta, z) = \rho - \rho_e, \quad \rho_e(\xi, \eta, z) = \rho_d [1 + \hat{T}(s_y(\xi, \eta) - z)]. \quad (\text{A.26})$$

To derive the integral forms of these equations, further explicit assumptions are made concerning the structure of the flow field:

- (v) A strong axial velocity dominates the component in the cross-stream direction, i.e.,

$$u = V(\xi, \eta, z) \gg v$$

Similarly, the magnitude of the turbulent Reynolds stresses are related to the intensity of the mean current in that direction, so

$$\tau_{\xi z} \gg \tau_{\eta z}.$$

(Note, this assumption is related to the self-similar character of the turbulent velocity profiles. See (vi).)

- (vi) The velocity and excess density fields are confined to a region adjacent to the bottom, bounded by the contour, $z = d(\xi, \eta)$, along which both quantities are negligible, i.e.,

$$\begin{aligned} \Delta \rho &\doteq 0, \\ V &\doteq 0, \end{aligned} \quad \text{at } z = d(\xi, \eta).$$

Furthermore, the profiles of these quantities exhibit a self-similar form, so that the structure of the turbulence and specifically the frictional stresses and rate of entrainment may be related solely to the mean velocity and density contrasts. For convenience, these properties will be assumed uniform over the cross section, i.e.,

$$V = V(\xi; d) \quad \text{and} \quad \Delta\rho = \Delta\rho(\xi; d).$$

Otherwise, unknown form factors must appear in the integral equations.

- (vii) The aspect ratio of the cross section is small, which implies that the pressure gradient terms are negligible with respect to the gravitational accelerations. Specifically, if the half width of the cross section is l ,

$$d/l \ll s.$$

Then, since the pressure is hydrostatic and $\Delta\rho$ is uniform in z ,

$$\left. \begin{aligned} p_x &= \hat{g} \Delta\rho dx \\ p_y &= \hat{g} \Delta\rho dy \end{aligned} \right\} \ll s \hat{g} \Delta\rho.$$

This also implies that $\hat{T}z$ is negligible in the expression for external density, i.e., $\rho_e(\xi, \eta) \doteq \rho_0 [1 + \hat{T}sy]$.

- (viii) Finally, the current is narrow in the sense that the cross-stream scale is much less than the local radius of curva-

ture of the stream axis, i.e.,

$$l \ll k^{-1} = l / \frac{d\theta}{d\xi}.$$

This condition insures that the transformation to stream-wise coordinates exists for the entire flow, and furthermore

$$h = 1 - \eta k \doteq 1.$$

Also, if the ambient stratification is sufficiently weak, the external density may be evaluated at the stream axis, that is,

$$\rho_e = \rho_0 [1 + \hat{\tau} s Y(\xi)] = \rho_e(\xi),$$

provided

$$|y(\xi, \eta) - Y(\xi)| = |\eta \cos \beta| \ll 1/s\hat{\tau}.$$

With these restrictions, the differential equations (A.19) - (A.22) take the form,

$$V_{\xi} + w_z = 0, \tag{A.27}$$

$$(\rho V)_{\xi} + (\rho w)_z = 0, \tag{A.28}$$

$$\rho V V_{\xi} + \rho w V_z = \frac{\partial \tau_{\xi z}}{\partial z} + s \hat{g} \Delta \rho \sin \beta, \quad \text{and} \tag{A.29}$$

$$\rho V \left(\hat{\tau} + V \frac{d\theta}{d\xi} \right) = s \hat{g} \Delta \rho \cos \beta. \tag{A.30}$$

Equations (A.27) - (A.30) may then be suitably combined and integrated over the stream cross section giving:

$$\frac{d}{d\xi} (AV) = \int_{l^-}^{l^+} w_e d\eta, \quad (\text{A.31})$$

$$\frac{d}{d\xi} (\rho AV) = \rho_e \int_{l^-}^{l^+} w_e d\eta, \quad \text{and} \quad (\text{A.32})$$

$$\frac{d}{d\xi} (\rho AV^2) = s \hat{g} \Delta \rho A \sin \beta - \int_{l^-}^{l^+} (\tau_B + \tau_I) d\eta, \quad (\text{A.33})$$

where $w_e(\xi, \eta) = w(\xi, \eta, d)$ is the entrainment velocity at the interface, and the stresses $\tau_B = \tau_{\xi z}(\xi, \eta, 0)$ (bottom) and $\tau_I = \tau_{\xi z}(\xi, \eta, d)$ (interfacial) are defined in a sense opposing the mean motion. The edges of the flow are at $\eta = l^-(\xi), l^+(\xi)$ and

$$A(\xi) = \int_{l^-}^{l^+} d\eta \int_0^d dz. \quad (\text{A.34})$$

Finally, the turbulent entrainment and friction laws are adopted based on the similarity forms of the profiles:

$$\text{(ix)} \quad E_0 V = \int_{l^-}^{l^+} w_e d\eta, \quad \text{and} \quad (\text{A.35})$$

$$\text{(x)} \quad \rho K V^2 = \int_{l^-}^{l^+} (\tau_B + \tau_I) d\eta. \quad (\text{A.36})$$

Hence, the integral forms of the streamtube model equations, based on the set of constraints and assumptions (i) - (x), are given by,

$$\frac{d}{d\xi} (AV) = E_0 V, \quad (\text{A.37})$$

$$\frac{d}{d\xi} (\rho AV) = \rho_e E_0 V, \quad (\text{A.38})$$

$$\frac{d}{d\xi} (\rho AV^2) = s \hat{g} \Delta \rho A \sin \beta - \rho K V^2, \text{ and} \quad (\text{A.39})$$

$$\rho V \left(\hat{f} + V \frac{d\theta}{d\xi} \right) = s \hat{g} \Delta \rho \cos \beta, \quad (\text{A.40})$$

where $\rho(\xi) = \rho_e + \Delta \rho$, $\rho_e(\xi) = \rho_0 [1 + s \hat{T} Y(\xi)]$ (A.41)

and $\hat{f} = Z \Omega \cos \alpha$, $\hat{g} = g \cos \alpha$, $\hat{T} = T \cos \alpha$,

$$s = \tan \alpha.$$

APPENDIX B

Derivation of Approximate Solutions
to the Streamtube Model Equations for Certain Limiting Cases

Approximate solutions are sought to the streamtube model equations (2.20) - (2.25) subject to initial conditions (2.26). Due to the highly nonlinear character of these equations, analytic solutions are precluded except in certain asymptotic regimes. Those solutions which are accessible may be divided into two categories:

- (i) Linearized solutions may be derived for small values of the parameters and restricted initial conditions using perturbation expansions valid in the vicinity of the source. The results to first order give wave-like solutions plus secular terms which indicate initial trends in the exact solution along with amplitude and scale of the waves.
- (ii) Asymptotic solutions valid in the downstream region ($\xi' \rightarrow \infty$) may be found since the waves present in the source region are damped by friction or entrainment and β attains a constant value. With this simplification, certain closed-form solutions may be found.

In all cases, the results obtained for these limiting cases are confirmed by numerical solutions to the exact equations.

In the absence of external stratification ($\gamma = 0$), the flow is characterized by a constant flux of excess density, $H' = A_0' V_0' = H_0'$,

and it is convenient to redefine the entrainment and friction parameters slightly,

$$\bar{\delta} = \delta/H'_0 = E_0/LH'_0 \quad , \quad (\text{B.1})$$

and

$$\bar{\kappa} = \kappa/H'_0 = K/LH'_0 \quad . \quad (\text{B.2})$$

The approximate solutions for four limiting cases are derived below.

B.1 Small Entrainment and Friction, $\bar{\delta}, \bar{\kappa} \ll 1$; Homogeneous Environment, $\gamma=0$.

In this limit, the governing equations (2.20) to (2.23) reduce to the following form:

$$A'V' = r' H_0' , \quad (\text{B.3})$$

$$\frac{dr'}{d\xi'} = \bar{\delta} V' , \quad (\text{B.4})$$

$$r' V'^2 \frac{d\beta}{d\xi'} = \cos \beta - r' V' , \quad (\text{B.5})$$

and

$$r' V' \frac{dV'}{d\xi'} = \sin \beta - (\bar{\delta} + \bar{\kappa}) V'^3 . \quad (\text{B.6})$$

Expand the dimensionless flow variables in bilinear perturbation expansions of the form,

$$\phi'(\xi) = \sum_{m=0}^{\infty} \sum_{n=0}^{\infty} \bar{\delta}^m \bar{\kappa}^n \phi_{m,n}'(\xi) . \quad (\text{B.7})$$

Also, to make the problem tractable and obtain a self-consistent result, set $\beta_{0,0} = 0$ and restrict the initial values of β' and V' .

$$\beta_0 \leq \Theta(\bar{\delta}, \bar{\kappa}) ,$$

and

(B.8)

$$V_0' = 1 + \Delta V_0' \quad \text{WHERE} \quad \Delta V_0' \leq \Theta(\bar{\delta}, \bar{\kappa}) .$$

After substituting the expanded variables into equations (B.3) - (B.6) and the initial conditions, the resulting ordered set of problems

yields constant values at lowest order:

$$r_{0,0} = V_{0,0} = 1 \quad \text{and} \quad A_{0,0} = A'_0. \quad (\text{B.9})$$

At order $\bar{\kappa}$, the solution contains topographic meanders of length $(2\pi L)$ and predicts a mean pitch angle,

$$\begin{aligned} \beta_{0,1} &= \frac{\beta_0 - \bar{\kappa}}{\bar{\kappa}} \cos \xi' + \frac{\Delta V_0'}{\bar{\kappa}} \sin \xi' + 1, \\ V_{0,1} &= -\frac{\beta_0 - \bar{\kappa}}{\bar{\kappa}} \sin \xi' + \frac{\Delta V_0'}{\bar{\kappa}} \cos \xi', \end{aligned} \quad (\text{B.10})$$

$$A_{0,1} = \left(A'_0 / \bar{\kappa} \right) \left[(\beta_0 - \bar{\kappa}) \sin \xi' + \Delta V_0' (1 - \cos \xi') \right],$$

and

$$r_{0,1} = 0$$

While at order $\bar{\delta}$ secular terms appear in the density, velocity and cross-sectional area expressions,

$$r_{1,0} = \xi',$$

$$V_{1,0} = -\xi', \quad (\text{B.11})$$

$$A_{1,0} = (A'_0 V_0') 2 \xi',$$

and

$$\beta_{1,0} = 0.$$

Hence, the full solution to first order in both $\bar{\delta}$ and $\bar{\kappa}$ is given by,

$$r' = 1 + \bar{\delta} \zeta', \quad (\text{B.12})$$

$$V' = 1 - \bar{\delta} \zeta' - (\beta_0 - \bar{\kappa}) \sin \zeta' + \Delta V_0' \cos \zeta', \quad (\text{B.13})$$

$$\beta = (\beta_0 - \bar{\kappa}) \cos \zeta' + \Delta V_0' \sin \zeta' + \bar{\kappa}, \quad (\text{B.14})$$

and $A' = A_0' [1 + 2\bar{\delta} \zeta' + (\beta_0 - \bar{\kappa}) \sin \zeta' + \Delta V_0' (1 - \cos \zeta')]$. (B.15)

Note that the perturbation scheme breaks down where the secular terms grow to be order one, i.e., at $\zeta' \sim \bar{\delta}^{-1}$. The validity of this solution is therefore confined to within a distance of order $L/\bar{\delta}$ from the source.

B.2 Downstream Limit for Zero Entrainment $\bar{\delta} = 0$, and Homogeneous Environment, $\bar{\gamma} = 0$.

In the asymptotic limit ($\xi' \rightarrow \infty$) for the case $\bar{\delta} = \bar{\gamma} = 0$, the waves induced by the source conditions are damped by friction and all flow variables attain constant values. These values are governed by the following expressions which are easily obtained from the model equations and initial conditions:

$$r' = 1,$$

$$A' = H_0' / V', \quad (\text{B.16})$$

$$\tan \beta = \bar{\kappa} V'^2,$$

and

$$\bar{\kappa}^2 V'^6 + V'^2 - 1 = 0.$$

Solving the cubic equation in V'^2 yields

$$V' = \frac{1}{2^{1/6} \bar{\kappa}^{1/3}} \left\{ \left(1 + \sqrt{1 + \frac{4}{27} \bar{\kappa}} \right)^{1/3} + \left(1 - \sqrt{1 + \frac{4}{27} \bar{\kappa}} \right)^{1/3} \right\}, \quad (\text{B.17})$$

as the only positive real root for the dimensionless velocity. Therefore all the variables in (B.16) are specified by (B.17).

B.3 Downstream Limit for Zero Friction, $\bar{\kappa} = 0$, and Homogeneous Environment, $\gamma = 0$.

For this case, waves induced by the initial conditions are damped in the downstream by the entrainment and the pitch angle approaches a constant value. The limiting forms of equation (2.21) - (2.23) are,

$$\frac{dr'}{d\xi'} = \bar{\delta} V' , \quad (\text{B.18})$$

$$r' V' = \cos \beta , \quad (\text{B.19})$$

and

$$r' V' \frac{dV'}{d\xi'} + \bar{\delta} V'^3 = \sin \beta . \quad (\text{B.20})$$

By combining (B.18) with (B.20) and making use of (B.19), it is easily seen that the only constant value of β which is consistent with this limit is $\beta = 0$. Once this fact is established, asymptotic expressions for the other variables are easily derived by integrating equations (B.18) and (B.20),

$$r' = (2\bar{\delta}\xi' + C)^{1/2} \sim (2\bar{\delta}\xi')^{1/2} , \quad (\text{B.21})$$

$$V' = (2\bar{\delta}\xi' + C)^{-1/2} \sim (2\bar{\delta}\xi')^{-1/2} , \quad (\text{B.22})$$

and

$$A' = (A'_0 V'_0) (2\bar{\delta}\xi' + C) \sim 2A'_0 V'_0 \bar{\delta}\xi' , \text{ as } \xi' \rightarrow \infty , \quad (\text{B.23})$$

where C is an arbitrary constant.

The balance in equation (B.20) with $\beta = 0$ implies that the dimensionless downstream momentum flux, $A'V'^2$, is non-divergent. Assuming this condition holds downstream, it is possible to include a weak frictional effect in this limit by assuming the pitch angle is small but non-zero. Then the viscous and gravitational forces in the momentum equation are balanced to order β^2 , i.e.,

$$\sin \beta \approx \beta = \bar{\kappa} V'^3 = \bar{\kappa} (2\bar{\delta}\bar{\zeta}' + c)^{-3/2}. \quad (\text{B.24})$$

Since $\bar{\kappa}$ is no longer zero, the arbitrary constant appearing in the limiting forms is formally a function of $\bar{\kappa}$, i.e., $c = c(\bar{\kappa})$.

B.4 Small Friction, $\kappa \ll 1$, Weak Stratification, $\gamma \ll 1$,
Zero Entrainment, $\delta = 0$.

The appropriate limiting equations for this case are,

$$\frac{dH'}{d\xi'} = -\gamma r' H' \sin \beta, \quad (\text{B.25})$$

$$\frac{dr'}{d\xi'} = \gamma r'^2 \sin \beta, \quad (\text{B.26})$$

$$r' V'^2 \frac{d\beta}{d\xi'} = \cos \beta - r' V', \quad (\text{B.27})$$

and
$$r' V' \frac{dV'}{d\xi'} = \sin \beta - \kappa \frac{V'^3}{H'} \quad (\text{B.28})$$

The expansion procedure used to solve these is entirely analogous to that used in Section B.1 except that the small parameters are κ and γ rather than $\bar{\delta}$ and $\bar{\kappa}$. If the initial conditions are again restricted as in (B.8) and the assumption $\beta_{0,0} = 0$ is made, then the set of ordered problems leads to constant values at lowest order as before in (B.9). At first order κ , the wave-like solutions again result as in (B.10), however, there is no contribution to r' or H' at order γ since $\sin \beta = O(\kappa)$. Variations in these quantities first appear at second order where,

$$H_{2,0} = -H'_0 \left(\frac{\beta_0}{\gamma} \sin \xi' + \frac{\Delta V'_0}{\gamma} \cos \xi' \right), \quad (\text{B.29})$$

and
$$r_{2,0} = \frac{\beta_0}{\gamma} \sin \xi' + \frac{\Delta V'_0}{\gamma} \cos \xi' \quad \text{at order } \gamma^2,$$

also
$$H_{1,1} = -\xi' + \sin \xi', \quad (B.30)$$

and
$$r_{1,1} = \frac{1}{H_0'} (\xi' - \sin \xi') \quad \text{at order } \gamma \kappa .$$

These corrections to the constant values at lowest order yield an approximate solution of the following form,

$$H' = H_0' \left[1 - \gamma \left\{ (\beta_0 - \bar{\kappa}) \sin \xi' + \Delta V_0' \cos \xi' + \bar{\kappa} \xi' \right\} \right], \quad (B.31)$$

$$r' = 1 + \gamma \left[(\beta_0 - \bar{\kappa}) \sin \xi' + \Delta V_0' \cos \xi' + \bar{\kappa} \xi' \right], \quad (B.32)$$

$$V' = 1 + (\beta_0 - \bar{\kappa}) \sin \xi' + \Delta V_0' \cos \xi', \quad (B.33)$$

$$\beta' = (\beta_0 - \bar{\kappa}) \cos \xi' - \Delta V_0' \sin \xi' + \bar{\kappa}, \quad (B.34)$$

and

$$A' = A_0' \left[1 - (\beta_0 - \bar{\kappa}) \sin \xi' + \Delta V_0' (1 - \cos \xi') \right] \quad (B.35)$$

where
$$\bar{\kappa} = \kappa / H_0'$$

The secular terms in these expressions are of order $\gamma \bar{\kappa}$ so that the validity of the solution extends out to $\xi \sim L / \gamma \bar{\kappa}$.

APPENDIX C

Method of Characteristics for Flow
near the Upper Edge in the Strong Rotation Limit

The analysis of nonlinear first-order partial differential equations by the method of characteristics is quite well known. Following the notation of Garabedian (1964), equation (5.47) may be expressed in general form as,

$$F = p^2 + q^2 - q = 0 \quad (\text{C.1})$$

where $p = \bar{d}\bar{x}$ and $q = \bar{d}\bar{y}$. Then the characteristic paths for the first-order equation are defined in terms of the characteristic coordinate, r , by

$$\frac{d\bar{y}}{dr} = F_p = 2p = \pm 2\sqrt{q(1-q)}, \quad (\text{C.2})$$

$$\frac{d\bar{x}}{dr} = F_q = 2q - 1, \quad (\text{C.3})$$

while the solution is governed by differential equations along the characteristics

$$\frac{du}{dr} = pF_p + qF_q = 2p^2 + 2q^2 - q = q, \quad (\text{C.4})$$

$$\frac{dp}{dr} = -F_q - pF_u = 0, \quad (\text{C.5})$$

$$\frac{dq}{dr} = -F_\Delta - q F_u = 0, \quad (C.6)$$

where $u = \bar{d}$ is the layer thickness and $(\bar{x}, \bar{y} - \bar{y}_e(0)) = (\xi, \Delta)$ are the coordinates on the characteristic path. Initial data for the integration of this system is specified along the source profile at $\bar{x} = 0$, in terms of the initial value parameter, t , which measures the distance from the upper edge of the layer:

$$\begin{aligned} \xi(0, t) &= 0, \\ \Delta(0, t) &= t, \\ u(0, t) &= u_0(t), \end{aligned} \quad (C.7)$$

$$p(0, t) = p_0(t) = \pm \sqrt{q_0(1-q_0)},$$

and $q(0, t) = q_0(t),$

where $t = \bar{y} - \bar{y}_e(0)$ along $\bar{x} = 0$.

Equations (C.6) and (C.7) indicate that p and q are constant along characteristics. Integration of the remaining equations gives

$$\xi(r, t) = \pm 2\sqrt{q_0(1-q_0)} r, \quad (C.8)$$

$$\Delta(r, t) = (2q_0 - 1)r + t, \quad (C.9)$$

and $u(r, t) = q_0 r + u_0(t) \quad (C.10)$

The multiplicity of solutions to the nonlinear equation is evidenced by the two possibilities for the sign of the radical in (C.8). For the present case, the positive sign is chosen in order that the characteristics be traced in the downstream direction. Moreover, in order that the layer thickness grow in the cross-stream direction, q_0 must be positive. Then for real solutions to (C.8), q_0 must be bounded as follows,

$$0 \leq q_0 \leq 1.$$

Finally, the inversion from characteristic variables to geometric coordinates requires that the Jacobian of the transformation be non-zero, i.e.,

$$J = \begin{vmatrix} \xi_r & \Delta_r \\ \xi_t & \Delta_t \end{vmatrix} = 2\sqrt{q_0(1-q_0)} \neq 0.$$

Therefore, $q_0 \neq 0, 1$, so,

$$0 < q_0 < 1. \quad (\text{C.11})$$

With q_0 suitably constrained, equation (C.8) may be solved for r , and substitution into (C.9) and (C.10) yields expressions for the trajectory of the characteristic and the corresponding layer thickness variable,

$$A(\bar{x}, \bar{y}; t) = \bar{y} - \bar{y}_e(0) = \frac{(2q_0 - 1)}{2\sqrt{q_0(1-q_0)}} \bar{x} + t \quad (\text{C.12})$$

and

$$\bar{d}(\bar{x}, \bar{y}; t) = \frac{g_0}{2\sqrt{g_0(1-g_0)}} \bar{x} + u_0(t) \quad (\text{C.13})$$

If the second cross-stream derivative of the layer thickness is negative, then characteristics in the downstream region are expected to intersect since the trajectories nearest the edge pitch most steeply downslope. Points on the envelope of characteristics so formed satisfy simultaneously the path equation (C.12) and

$$0 = \Delta_{c,t} = \frac{g_0'}{4(g_0 - g_0^2)^{3/2}} \xi_c + 1 \quad (\text{C.13})$$

where $g_0'(t) = \frac{dg_0}{dt} = \bar{d}_{\bar{y}\bar{y}}(0, \bar{y}; t)$, (ξ_c, Δ_c) are the points in the envelope. Solving for these coordinates in terms of the initial data gives,

$$\xi_c = \frac{-4(g_0 - g_0^2)^{3/2}}{g_0'} \quad (\text{C.14})$$

and

$$\eta_c = \frac{2g_0}{g_0'} (2g_0^2 - 3g_0 + 1) \quad (\text{C.15})$$

Downstream from the locus of points given by (C.14) and (C.15) the method of characteristics breaks down as the inversion from characteristic variables to geometric coordinates $(r, t) \rightarrow (\xi, \Delta)$ becomes multivalued.

REFERENCES

- Abramowitz, M., and I. A. Stegun, (1970) Handbook of Mathematical Functions, National Bureau of Standards Applied Mathematics Series 55, U.S. Government Printing Office, Washington, D.C.
- Batchelor, G.K., (1967) An Introduction to Fluid Dynamics, Cambridge University Press, Cambridge University Press, Cambridge, England.
- Bowden, K.F., (1960) The dynamics of flow on a submarine ridge, Tellus, XII, 4, 418-426.
- Caldwell, D.R., C. W. VanAtta and K. N. Helland, (1972) A laboratory study of the turbulent Ekman layer, Geophys. Fluid Dynamics, 3, 125-160.
- Clarke, N.S., (1968) Two-dimensional flow under gravity in a jet of viscous liquid, J. Fluid Mech., 31, 3, 481-500.
- Cole, J.D., (1968) Perturbation Methods in Applied Mathematics, Blaisdell Publishing Co., Waltham, Mass.
- Cooper, L.H.N., (1955) Deep water movements in the North Atlantic as a link between climatic changes around Iceland and biological productivity of the English Channel and Celtic Sea, J. Mar. Res., 14, 347-362.
- Csanady, G.T., (1967) On the "resistance law" of a turbulent Ekman layer, J. Atmos. Sci., 24, 467-471.
- Davies and Rideal, (1963) Interfacial Phenomena, J. Wiley and Sons, New York.

- Defant, A. (1961) Physical Oceanography, Vol. I, Chap. X, Pergamon Press, New York.
- Ellison, T.H., and J. S. Turner, (1959) Turbulent entrainment in stratified flows, J. Fluid Mech., 6, 423-448.
- Faller, A.J., (1971) Oceanic mixing and the Langmuir circulation, Technical Note BN 683, Institute for Fluid Dynamics and Applied Mathematics, University of Maryland, College Park.
- Grant, A.B., (1968) Atlas of Oceanographic Sections, Davis Strait - Labrador Basin - Denmark Strait 1965-1967, Atlantic Oceanographic Laboratory, Bedford Institute, unpublished manuscript.
- Hart, J.E., (1972) A laboratory study of baroclinic instability, Geoph. Fluid Dyn., 3, 181-209.
- Harvey, J.G., (1961) Overflow of cold deep water across the Iceland-Greenland Ridge, Nature, 189, 911-913.
- Heezen, B.C. and G. L. Johnson, (1969) Mediterranean Undercurrent and microphysiography west of Gibraltar, Bull. Inst. Oceanogr. Monaco, 67, 1-51.
- Johnson, G.L. and E. D. Schneider, (1969) Depositional ridges in the North Atlantic, Earth and Plan. Sci. Let. 6, 416-422.
- Lee, A.J. and D. Ellett, (1965) On the contribution of overflow water from the Norwegian Sea to the hydrographic structure of the North Atlantic Ocean, Deep-Sea Res. 12, 129-142.

- Lee, A.J. and D. Ellett (1967) On water masses of the Northwest Atlantic Ocean, Deep-Sea Res., 14, 183-190.
- Madelain, F., (1970) Influence de la topographie du fond sur l'écoulement Méditerranéen entre le Détroit de Gibraltar et le Cap Saint-Vincent, Cah. Oceanog., XXII, 1, 43-61.
- Mann, C.R., (1969) Temperature and salinity characteristics of the Denmark strait overflow, Deep-Sea Res., Suppl. to Vol. 16, 125-137.
- Monin, A.S., (1970) The atmospheric boundary layer, Annual Reviews of Fluid Mechanics, 2, 225-250.
- Saunders, P.M., (1973) The instability of a baroclinic vortex, J. Phys. Oceanogr., 3, 61-65.
- Saunders, K.D., and R. C. Beardsley, (1972) The design and construction of an ultra-stable air-bearing turntable, Rev. Sci. Inst., 43(10), 1451-1453.
- Smith, P.C., (1973) A similarity solution for slow viscous flow down an inclined plane, J. Fluid Mech., 59, 275-288.
- Steffansson, U., (1968) Dissolved nutrients, oxygen, and water masses in the Northern Irminger Sea, Deep-Sea Res., 15, 541-575.
- Stommel, H., and A. B. Arons, (1972) On the abyssal circulation of the world ocean - V. The influence of bottom slope on the broadening of inertial boundary currents, Deep-Sea Res., 19, 707-718.

- Turner, J.S., (1973) Buoyancy Effects in Fluids, Cambridge University Press, Cambridge, England.
- Weatherly, G.L., (1972) A study of the bottom boundary layer of the Florida Current, J. Phys. Oceanogr., 2, 54-72.
- Whitehead, J.A., A. Leetmaa, and R. A. Knox, (1973) Rotating hydraulics of strait and sill flows, Woods Hole Oceanographic Institution Contribution No. 3038, Woods Hole, Mass.
- Worthington, L.V., (1969) An attempt to measure the volume transport of Norwegian Sea overflow water through the Denmark Strait, Deep-Sea Res., suppl. to vol. 16, 421-432.
- Worthington, L.V., (1970) The Norwegian Sea as a mediterranean basin, Deep-Sea Res., 17, 77-84.
- Worthington, L.V., and G. Metcalf, (1961) The relationship between potential temperature and salinity in deep Atlantic water, Rapp. P.-V. Reun. Cons. perm. int. Explor. Mer., 149, 122-128.
- Yih, C.-S., (1969) Fluid Mechanics, McGraw-Hill Book Company, New York.

BIOGRAPHICAL NOTE

Peter Colvin Smith was born on June 15, 1944, in East Orange, New Jersey. He received his Bachelor's and Master's degrees in aerospace engineering from Brown University in 1966 and 1967 respectively. On June 17, 1967, he married the former Julia Jane Berry of Englewood, New Jersey. After two years of employment at Avco Systems Division, Wilmington, Mass., he entered the M.I.T.-W.H.O.I. Joint Program to pursue his Ph.D. in physical oceanography.